

Computational Investigations of Topological and Magnetic Phases in a few Chalcogenides and Rare-Earth Oxides

A Thesis

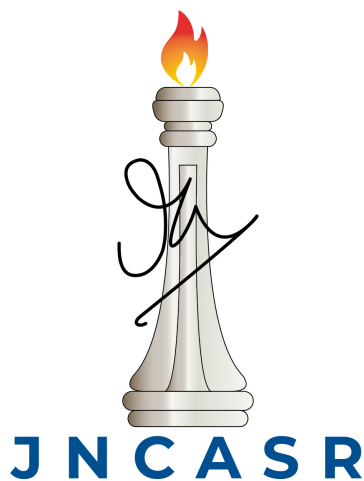
Submitted for the Degree of

Doctor of Philosophy

in the Faculty of Science

by

Anita Gemmy Francis



Theoretical Sciences Unit
Jawaharlal Nehru Centre For Advanced Scientific Research
Bangalore, INDIA

July 2024

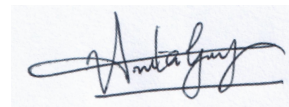
To

Amma and Appa

DECLARATION

I hereby declare that the matter embodied in the thesis entitled **Computational Investigations of Topological and Magnetic Phases in a few Chalcogenides and Rare-Earth Oxides** is the result of investigations carried out by me at the **Theoretical Sciences Unit**, Jawaharlal Nehru Centre for Advanced Scientific Research, Bangalore, India, under the supervision of **Prof. Swapan K. Pati** and that it has not been submitted elsewhere for the award of any degree or diploma.

In keeping with the general practice in reporting scientific observations, due acknowledgement has been made whenever the work described is based on the findings of other investigators.

A handwritten signature in black ink, appearing to read 'Anita Gemmy Francis', is shown within a light blue rectangular box.

Anita Gemmy Francis

CERTIFICATE

I hereby certify that the matter embodied in this thesis entitled **Computational Investigations of Topological and Magnetic Phases in a few Chalcogenides and Rare-Earth Oxides** has been carried out by **Ms. Anita Gemmy Francis** at the **Theoretical Sciences Unit**, Jawaharlal Nehru Centre for Advanced Scientific Research, Bangalore, India under my supervision and that it has not been submitted elsewhere for the award of any degree or diploma.



Prof. Swapan K. Pati
(Research Supervisor)

Acknowledgements

This work required an enormous amount of support and goodwill from a lot of wonderful human beings. I would like to thank all those who lent me a helping hand or a compassionate word during my PhD days. Without their ardent support and constant cheers, my days as a PhD student would have become less enjoyable and scientifically murky.

First and foremost I would like to thank Prof. Swapan K. Pati, for instilling in me a scientific fervor and for allowing me to pursue scientific problems that interested me, with complete freedom. The scientific discussions and elaborate debates with him made me see things differently and has guided me in every step of reaching my final goal.

I would like to thank Prof. C.N.R Rao, for his vision and love of science. He has inspired me from a young age till now, with his passion for scientific curiosity. Thank you for being a torchbearer of research and academic pursuits in India.

I was blessed to have studied under some of the best teachers in the country. I am extremely thankful to my teachers, Prof N.S. Vidyadhiraja, Prof. Shobhana Narasimhan, Prof. Umesh Waghmare, Prof. Subir Das, Prof. Kavita Jain, Prof. Srikanth Sastry, Prof. A. Sundareshan and Dr. Awadhesh Narayan.

This PhD work would not have been possible without the wonderful collaborations

and thought provoking discussions within and outside JNCASR. I thank all my collaborators, Prof. Chandrabhas Narayana, Prof. A. Sundaresan, Prof. Amitava Patra, Prof. Sayan Bhattacharya, Prof. Kanishka Biswas, Dr. Raju Kumar Biswas, Dr. Janaky Sunil, Dr. Neha Bothra, Dr. Anjana Joseph, Dr. Rahul Kumar, Kritiman Marjit, Dr. Shahnaz Parveen, Dr. Viswadeepa Hazra, Dr. Subarna Das and Nesta. I am grateful to the Centre for Scientific and Industrial Research (CSIR), India for funding my research.

I thank the National Super-computing Mission (NSM), India, for access to the supercomputer ParamYukti, which was used extensively for all the calculations in this thesis.

I thank all the JNCASR staff, the always ready to help academic staff, the administrative staff and the dining hall staff.

I am thankful to Chandan and TSU Secretary, for helping me at all critical points.

I thank all my lab mates, for being the best everyday companions in this journey and I really hope I could also be the same to you. I am grateful for all the discussions and for making my stay at JNCASR memorable. I extend my gratitude to Sayan, Mayank, Brijesh, Sougata, Utkarsh, Soumya, Pralhad, Dr. Vipin, Dr. Supriya, Dr. Suparna, Souritra, Dr. Abhiroop, Dr. Neha, Dr. Madhulika, Dr. Pallavi, Dr. Bidhan and Dr. Supriti.

I am lucky to have met and befriended some wonderful people along the way. They have seen all my highs and lows and were there for me through all the thick and thin. They have indeed lessened the weight of the PhD yoke and have made me felt cherished in my entirety. I extend my heartfelt thanks to all my friends, Rani Geroqe, Reshma, Merin, Ann Ria, Janaky, Anjana, Kiran, Niloy, Varghese, Ravi, Rajarshi, Biswadeep, Amal, Nirmal, Deepak, Shubhangi, Arijit, Ashish, Rahul, Swarnima, Diksha, Hariharana, Suryadev, Soumyadeep, Krishna, Swarnendu, Debargya, Raghav, Prasanti, Shiv, Triplets, Graison, Geo, George, Nabeel and Henry.

I thank Anusooya Ma'am for being a home away from home and a beacon of support

throughout my PhD days.

I am extremely grateful to Vallyapappan, Thadipappan, Jolenta aunty for their constant prayers.

I thank my wonderful siblings Tony and Aleena for all the love and support they have shown me.

I am forever grateful to Athira, my one true soul mate and Abhijit, who has put up with me throughout the last five years.

I thank Appa and Amma, for all the sacrifices they have made for me, for believing in me and for cherishing me the way I am.

And lastly I thank Pushkar, for all the love, friendship and affection. I cannot imagine what life would have been without you. I feel blessed to have you as my most staunch supporter and am extremely grateful for all the discussions, both academic and non-academic, which has paved the way for the completion of this thesis.

List of Figures

1.1	The Hall Resistance R_{xy} and the magneto resistance R_{xx} of a 2D electron gas with the variation in magnetic field ^[1] . The Hall resistance, instead of linearly increasing with magnetic field, shows plateaus which are correspond to $h/\nu e^2$, where ν being an integer denotes integer quantum hall effect and ν is a fraction in fractional quantum hall effect ^[1]	2
1.2	Spaces with different topologies, characterized by the genus g . When a wavefunction corresponding to the ground state is wrapped on these different spaces, we get different degeneracies. For example, if wrapped on a sphere the degeneracy is 1 ^[3]	3
1.3	a) The skipping motion of electron's cyclotron orbits at the interface between the vacuum and a quantum hall state. b) The edge mode from Haldane's model for graphene in a periodic magnetic field is connecting the valence band and the conduction band by crossing the Fermi level ^[6]	5
1.4	The energy dispersion at various crystal momenta. $\Gamma_a = 0$ and $\Gamma_b = \pi/a$ are the time reversal invariant momenta, which are Kramers degenerate. Away from these points the degeneracy is lifted by the SOC. In (a) The bands at Γ_a and Γ_b connect in such a way that the bands intersect the Fermi level an even number of times while in (b) it is odd. The odd number of crossings denote topologically non-trivial phase ^[6]	7

-
- 1.5 (a) A magnetic flux threading a 2D cylinder. If the circumference is a single lattice constant, then this flux corresponds to the crystal momentum, k_x , on the edge. The time reversal invariant fluxes, 0 to $h/2e$, in this case is denoted as Λ_1 and Λ_2 . (b) Λ_a corresponds to the projections of the 4 TRIM in the 2D Brillouin zone. (c) In the 3D generalization, the Corbino torus can be threaded by two fluxes, which corresponds to the crystal momentum on a surface. There are four TRIM points on a given surface, which corresponds to the projection of the 8 TRIM points in a 3D Brillouin zone as shown in (d)^[8] 8
- 1.6 a) The surface Fermi surface of a Weak Topological Insulator (WTI). (b) The Fermi surface of a surface of a Strong Topological Insulator. In this case, the Berry phase acquired by the electronic state is π , as the k is changed (c) The Dirac cone present within the Fermi circle. 12
- 1.7 (a) Ising spins on a triangle with antiferromagnetic exchange. There are six possible ways the spins on this lattice can arrange. (b) A 2D triangular lattice formed from the triangular motifs shown in (a). (c) A 2D Kagome lattice^[19]. 16
- 1.8 (a) The valence bond state. The inset shows an entangled pair of spins, forming a valence bond. The VBS represents one arrangement of such valence bonds. (b) The superposition of VBS states gives a resonating valence bond state. The entanglement in (a) and (b) is short range. (c) The light blue valence bonds represent long range entanglement, which are less tightly bound and hence can be excited easily into a state with non-zero spin^[19]. 18

- 1.9 (a) and (b) The crystal structure of κ -(ET)₂Cu₂(CN)₃, (a) where the ET dimers form a triangular lattice. The $S = 1/2$ spin per dimer is shown as red arrow. (b) These ET molecules are stacked between layers of Cu₂(CN)₃^[24] (c), (d) Herbertsmithite structure, with the Cu atoms forming layers of Kagome lattice, which are interconnected by Zn^[25] and (e), (f) α -RuCl₃, where the Ru atoms arrange in honeycomb layers which are weakly coupled with Cl^[26] 21
- 1.10 The left hand side shows the Bloch wave functions in real space, $e^{ikx}u_k(x)$, for three different k s, for a single band in one-dimensional system. The right hand side shows the corresponding wannier functions^[51] 35
- 2.1 (a) Le Bail fit of the XRD pattern of TaSe₃ at ambient conditions. (b) The first Brillouin zone of TaSe₃, with the 101 and 100 planes shown as coloured rectangles. The 8 TRIM points are also denoted within the BZ. The top (c) and the side (d) views of the TaSe₃ structure. The chain like arrangement of the trigonal prisms is clear in (d) and we see four such chains in the unit cell (c). 53
- 2.2 (a) The band structure of TaSe₃ at 0 GPa without the inclusion of SOC. (b) The orbital projected band structure at 0 GPa. Without SOC, TaSe₃ shows no band gap. As SOC is included the bands near $B - \Gamma - A$, separate giving a finite band gap. In (b), the red bands correspond to the Ta d orbitals and the blue colour represents the Se p orbitals. At B , A and Y , there are clear signatures of band inversion. 56

- 2.3 Wannier Charge Centre evolution for the six time reversal invariant planes (a) $k_x = 0$ (b) $k_x = \frac{\pi}{a}$ (c) $k_y = 0$ (d) for $k_y = \frac{\pi}{b}$ (e) $k_z = 0$ (f) $k_z = \frac{\pi}{c}$ at 0GPa. A line is chosen at random at $\bar{W} = 0.55$, and is denoted by the red dotted line. If the number of times this line cuts any chosen WCC evolution line is even, then, Δ is 0, otherwise it's 1. In a), the line cuts the wcc evolution at one point, making it's Chern number 1. Similarly, for the other planes we get b) $\Delta = 1$ c) $\Delta = 0$ d) $\Delta = 0$ e) $\Delta = 1$ (3 mod 2) f) $\Delta = 1$ 57
- 2.4 (a) The ratio of lattice constants with pressure. The ratio shows a slope change at around 3 GPa and 8 GPa. b) and c) shows the Raman shift with pressure. At 3 GPa and 8 GPa, most of modes undergo a softening as opposed to the expected hardening. 58
- 2.5 (a) The orbital projected band structure at 2 GPa. The band inaversions are similar to the one seen at 0 GPa. However the gap at Γ has decreased. The band structure (b) 4.5 GPa (c)5.5 GPa and (d)7 GPa are shown subsequently. As the pressure rises, the band gap progressively decreases and beyond 4.5 GPa, a band inversion comes about at Γ , with a small gap, as seen in (c). With further pressure increase, the band gap at Γ increases with the retention of band inversion . . . 60
- 2.6 The change in band gap with pressure at the TRIM points (a) Γ , (b) B , (c) A , (d) Y . The first and second derivative of abnd gap with pressure is also plotted. (a)The band gap closes and reopens at the Γ point at around 5 GPa while at B , the gap closes and reopens at 7 GPa. 62

- 2.7 The surface spectrum and spin density difference on TaSe₃ surface at various pressures. (a) and (b) show the surface spectrum on the (10 $\bar{1}$) plane and the up and down spin density on the same, at 0 GPa. At 5.5 GPa, since we expect all surfaces to host the Dirac point, we have chosen (10 $\bar{1}$) plane, which is the natural cleavage plane of TaSe₃ as well. (c)- (d) show the surface spectrum of TaSe₃ at 5.5 GPa, on the (10 $\bar{1}$) plane. (e) and (f) are the surface spectrum and spin density difference on the 100 plane at 8 GPa. 65
- 3A.1 a) The crystal structure of Sb₂Te₃ in the R-3m space group. The primitive cell is given in (c). (b) The band structure of Sb₂Te₃ with the Sb and Te orbital projection. The High symmetry points in the Brillouin zone are represented in (d). The band structure (b) shows a band inversion at Γ 74
- 3A.2 a) The evolution of HWCCs on the $k_x = 0$ plane and (b) $k_x = \pi/a$ plane. The red line is chosen randomly and it is seen that on $k_x = 0$, it cuts the HWCC line once, making $\Delta = 1$, while on $k_x = \pi/a$, it cuts the HWCC evolution line zero times. Similarly, we see that (c) for $k_y = 0$ and (e) $k_z = 0$, $\Delta = 1$, and it is 0 for (d) $k_y = \pi/b$ and (f) $k_z = \pi/c$ 76
- 3A.3 a) The surface spectrum (simulated ARPES) of Sb₂Te₃ 001 plane. The Γ -point has a distinct Dirac node. Note the linear dispersion seen on either side. (b) The corresponding Fermi arc on the surface. The Fermi surface forms a closed loop around Γ , suggesting a π Berry phase. . . 79

- 3A.4 a) Sb_2Te structure after optimization. It crystallizes in the P-3m1 spacegroup. A bilayer of Sb_2 exists between quintuple layers of Sb_2Te_3 (b) The Brillouin zone and the high symmetry points. (c) The band structure with SOC. The top valence band has a predominant conduction bands Sb-p orbital character. The highly parabolic conduction bands and the valence bands are extremely useful in the field of thermoelectrics. 80
- 3A.5 (a) The 001 plane of Sb_2Te showing the topological surface states. The Dirac cone is observed at the Γ point. (b) The Fermi surface of the 001 plane at the Fermi level. There are multiple electron pockets on the surface, formed by the surface states. These pockets are formed around Γ and the three in equivalent boundary points M , of the surface. . . 81
- 3A.6 (a) The SbTe structure, which crystallizes in P-3m1 space group. It is made up of alternating layers of Sb_2Te_3 quintuple layers and Sb_2 layers along the c -axis. (b) The calculated band structure (with SOC) along the high symmetry points in the BZ. Band inversions are visible at the M , Γ and A points. (c) The surface spectrum of the 010 plane of SbTe . There is a Dirac cone at the centre of the surface Brillouin zone d) The Fermi contour on the surface shows a non-trivial Berry phase 83
- 3A.7 The HWCC evolution on the 6 TRIM planes of SbTe . The Δ of $k_x = 0$, $k_x = \pi/a$, $k_y = 0$, $k_y = \pi/b$ and $k_z = 0$ is 0, as observed from the HWCC evolution shown in (a),(b),(c),(d) and (e) respectively. In (f), we see that the arbitrary line (in red), crosses the line an odd number of times, giving $\Delta = 1$ 84

- 3B.1 The band structure of Sb_2Te_3 under uniaxial strain along the c -axis. The band structure at 0% strain is shown in (c). (a) corresponds to 4% compressive strain and (b) to 2% compressive strain. (d)-(f) shows the band evolution with tensile strain. It is clear that the band gap decreases with tensile strain and compressive strain leads to an increase in band gap at Γ 92
- 3B.2 (a) -(c) shows a decrease in the compressive strain in Sb_2Te_3 . (c) is the 0%-strain band structure. We see that the compressive strain do not lead to new band inversions or disappearance of old ones. (d) and (e) reports 2% and 4% tensile strain respectively. We see an additional band inversion appearing at the M -point suggesting a possible TQPT. 92
- 3B.3 The electronic band structure of Sb_2Te_3 under various pressures.(a)-(c) The band structure for 0.5 GPa, 2 GPa and 4 GPa pressure. The band structure remains similar, except the valley degeneracy increases as the pressure reaches 4 GPa. (d)-(f) shows the band structure at pressures 6 GPa, 8 GPa and 10 GPa. The band inversion at Γ , vanishes at pressures from 6 GPa and above. This leads to a trivial phase of Sb_2Te_3 at pressures above 6 GPa. 93
- 3B.4 (a) The band structure of Sb_2Te_3 at 2 GPa. (b) -(e) represents the band structure for 4 GPa, 6 GPa, 8 GPa and 10 GPa. The valence band and conduction band at the L -point comes closer with the increase in pressure. For 8 GPa (d) , we see a reversal of band characteristic at L . 95
- 4.1 The crystal structure of $\text{Yb}_2\text{Te}_5\text{O}_{13}$. The green and blue polyhedra corresponds to the two Yb atoms having a different crystal environment. These atoms form dimers as shown in (b) and (c), along the c -direction. The dimers are stacked along the a -direction 101

- 4.2 (a) The magnetic susceptibility with temperature. The Curie-Weiss linear fit, shown in red, corresponds to the behaviour of the system at high temperature paramagnetic region. The susceptibility deviates from the expected linear behaviour at around 125 K and at a lower temperature, around 45 K, the susceptibility turns upward sharply. (b) The variation of effective magnetic moment $\mu_{eff} = [(3k_B/N_A\mu_B^2)\chi T]^{1/2} \sim 2.828\sqrt{\chi T}$ with the temperature. The effective magnetic moment decreases as the temperature is lowered. (c) zero -field muon spin resonance measurements showing the a non-oscillatory behaviour in the depolarisation, suggesting the lack of a local static magnetic field. (d) The relaxation rate of the depolarization with temperature. As the temperature is lowered, the relaxation rates start increasing from around 200 K, until it plateaus below 10 K 103
- 4.3 The band structure and the atom projected Density of States for $\text{Yb}_2\text{Te}_5\text{O}_{13}$. From b) it is clear that the bands in the gap are formed by the f orbitals of Yb with significant contribution of O p and Te p orbitals near the Fermi level. 104
- 4.4 (a) The nearest neighbour pairs are aligned in the c -axis, with the exchange coupling represented by J_1 . (b) The second and third nearest neighbors lie in the $a-b$ plane and their exchange couplings are denoted as J_2 and J_3 respectively. 105
- 4.5 The energy per spin vs the linear system size L . The energy for the small L values remain almost the same after which it slowly increases. 105
- 4.6 (a)-(c) The spin-spin correlation along the a , b and c axes respectively. Alogn each axis the spin correlations are plotted for three different temperatures- 30 K, 100 K and 300 K. (d)-(f) The equal time structure factor for q_x , q_y and q_z . The peak for $S(q_x)$ and $S(q_z)$ is at π/a and π/c respectively. $S(q-y)$ do not show any specific peak. 106

- 4.7 (a) The equal time structure factor at 10 K on the (hk0) plane. This temperature is below the transition temperature observed in the simulations. (b) The structure factor at 50 K, which shows broad peaks near the boundary of the Brilluoin zone. This corresponds to a spiral ordering in the system, which arises beacuse of the thermal fluctatons acting on the classical spins 109
- 5.1 (a)The observed and refined powder x-ray diffraction pattern of NaYbW_2O_8 . The green lines mark the Bragg positions. The difference between experimental amd calculated intensities is given in blue. (b) The lattice structure of NaYbW_2O_8 , as viewd along the b-axis. (c) The magnetic lattice, with 50% disorder between the Yb and Na atoms. This lattice forms a hyperhoneycomb structure. 116
- 5.2 (a) and (b) shows a schematic representation of the nearest and next nearest neighbors in lattice A. (c) and (d) The nearest and next nearest pairs in lattice B. It is clear that lattice A is geometrically frustrated and that such geometric frustration is absent in lattice B. Lattice A has two nearest neighbors and four next nearest neighbors as compared to lattice B, which has four nearest neighbors and eight next nearest neighbors. 119
- 5.3 (a)The magnetic susceptibility vs temperature down to a temperature of 400 mK, under Zero Field cooled and Field cooled protocols. Two level curie-Weiss model fit to the inverse susceptibility data is given in the inset. (b)Measured heat capacity in a temperature range 2 K to 100 K, in the absence of magnetic field (c) The μSR measurements showing the depolarisation with temperature. The depolarisation shows an exponential decay. (d)The variation of the corresponding fitting parameter, λ with temperature. 121

5.4	The energy per spin, e , for various linear system sizes L (a) for lattice A and (b) lattice B. The energy per spin remains almost the same for varying L	123
5.5	a) The equal time structure factor of lattice A from Iterative Minimisation for $L=10$. The peaks in this case occur at $(\frac{\pm 1}{2}, \frac{\pm 3}{10}, \frac{\pm 3}{10})$. b) The equal time structure factor at 5 K ($T > T_c$). The peaks are diffused about the peaks in (a).	124
5.6	a) The equal time structure factor of lattice A from Iterative Minimisation for $L=12$ b) The equal time structure factor at 1 K ($T > T_c$). The peaks are broad and diffused about the peaks in (a)	125

List of Tables

2.1	The product of parity eigenvalues of the occupied bands at the high symmetry points for three different pressure ranges, 0 to 4.5 GPa, corresponding to the first weak topological insulator phase, 5.0 to 6.0 GPa, which marks the strong topological insulator phase and 7.0 to 12.0 GPa, which is the second weak topological phase. Their respective Z_2 invariants obtained from Fu-Kane parity analysis ^[26] are reported in the last column.	63
3A.1	The calculated Z_2 invariants for Sb_2Te_3 , Sb_2Te and SbTe . All three systems have the strong topological index as zero, suggesting that they are strong topological insulators.	79
4.1	The optimised lattice parameters.	100
4.2	The nearest, next nearest, third nearest neighbor exchange couplings and the zero-field splitting parameters calculated from first principles calculations.	106
4.3	The ordering vector Q , in units of 2π , of the ground state, obtained from the peak of the equal time structure factor calculated using Iterative Minimisation (IM).	108
5.1	The nearest, next nearest exchange couplings from first principles calculations for lattice A and lattice B	122

5.2	The ordering vector Q of the ground state for lattice A, in units of 2π , obtained from the peak of the equal time structure factor obtained from Iterative Minimisation (IM).	122
-----	--	-----

Contents

Acknowledgements	7
1 Introduction	1
1.1 Topological Order in Condensed Matter Physics	2
1.2 Topological Insulators	4
1.2.1 Topological Band Theory	5
1.2.2 Bulk-Boundary Correspondence	7
1.2.3 Quantum Spin Hall Insulator	8
1.2.4 3D Topological Insulators	12
1.2.5 Applications of Topological Insulators	14
1.3 Quantum Spin Liquids	16
1.3.1 Candidates for Quantum Spin Liquids	20
1.3.2 Applications of QSL	22
1.4 Computational Methods	23
1.4.1 Density Functional Theory	23
1.4.2 Approximations to the Exchange Correlation Functional . . .	30
1.4.3 Tight Binding Model	33
1.4.4 Maximally Localised Wannier Functions	35
1.4.5 Z_2 Invariant from Wannier Charge Centre	37
1.5 Summary of the Thesis	40

2	Evolution of Topological Phases of TaSe₃ under Hydrostatic Pressure	51
2.1	Introduction	51
2.2	Computational Methods	54
2.3	Results	56
2.3.1	The Dirac Cone on TaSe ₃ surface	64
2.4	Conclusion and Discussion	66
3A	Topological Phases of (Sb₂Te₃)_m(Sb₂)_n Homologous Series	73
3A.1	Introduction	73
3A.2	Computational Methods	76
3A.3	Results	77
3A.4	Conclusion	85
3B	Evolution of the Topological properties of Sb₂Te₃ and Sb₂Te under Uniaxial strain and Hydrostatic Pressure	89
3B.1	Introduction	89
3B.2	Computational Methods	90
3B.3	Results and Discussions	91
3B.3.1	Uniaxial Strain	91
3B.3.2	Hydrostatic Pressure	94
3B.4	Conclusion and Discussions	96
4	Dynamic Magnetic Ground State in Yb₂Te₅O₁₃, a Dimer-based Compound	99
4.1	Introduction	99
4.2	Computational Methods	101
4.3	Results	104
4.4	Conclusion	110

5	NaYbW₂O₈ : A Possible Quantum Spin Liquid in a Hyperhoneycomb Lattice	115
5.1	Introduction	115
5.2	Computational Methods	117
5.3	Results	120
5.4	Conclusion	126
6	Conclusion and Future Outlook	135
	Other Works	139

Introduction

The pursuit of exotic phenomena has time-and-again stirred intrigue and excitement in the field of condensed matter physics. These exotic phases are distinct from the traditional paradigm of Landau-Ginzburg, whereby the different phases are identified by the various symmetries that the phase holds, and are characterized by the presence of a “topological order”, which does not arise from simple symmetry-breaking. This order, without symmetry, is based on the global properties of the system and not the local ones. Topologically non-trivial phases give rise to topological properties, by which I mean properties which cannot be destroyed by local perturbations, for instance, the emergence of fractional statistics. The main defining feature of such an exotic state is the highly entangled ground state of the phase. The “topological order” in some sense is a measure of this long range entanglement in such phases.

In this thesis, I have considered two interesting phases of matter, that have received tremendous impetus in the last decade - Topological Insulators and Quantum Spin Liquids. These novel phases of matter, in addition to providing a very interesting platform to understand the rich physics in low energy materials, are extremely important when it comes to material applications, ranging from thermoelectricity to quantum computing. Although both of these phases are “non-trivial”, a topological insulator in reality is a symmetry protected topologically trivial phase, while the quantum spin liquid phases are topologically non-trivial. To understand the differ-

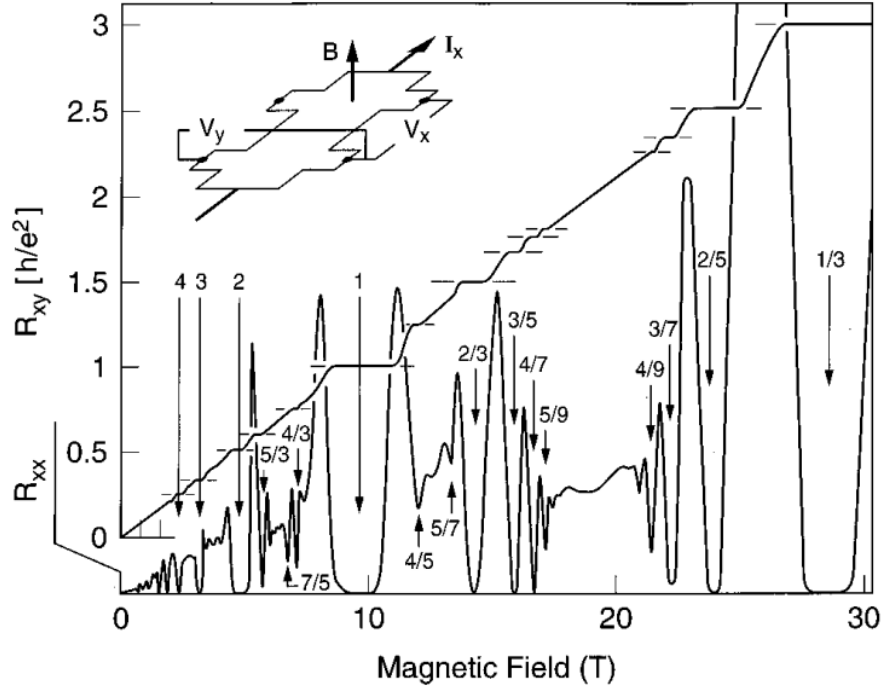


Figure 1.1: The Hall Resistance R_{xy} and the magneto resistance R_{xx} of a 2D electron gas with the variation in magnetic field^[1]. The Hall resistance, instead of linearly increasing with magnetic field, shows plateaus which correspond to $h/\nu e^2$, where ν being an integer denotes integer quantum hall effect and ν is a fraction in fractional quantum hall effect^[1]

ence between the two, let us understand the meaning of “topological order”.

1.1 Topological Order in Condensed Matter Physics

The necessity to come up with a new order parameter arises from the existence of phases of matter which cannot be distinguished by symmetry-breaking. To understand this in detail, let us look at the case of Fractional Quantum Hall (FQH) effect. When a potential is applied across the length of a two dimensional electron gas in the presence of a perpendicular magnetic field, then there exists a potential V , across the width, which is characterized by a quantized conductivity. This quantization can be integer, leading to integer quantum hall effect or fractional, leading to fractional quantum hall effect. As shown in Fig. 1.1, the Hall resistance vs magnetic field hosts numerous plateaus, each of which corresponds to a different phase. And it has

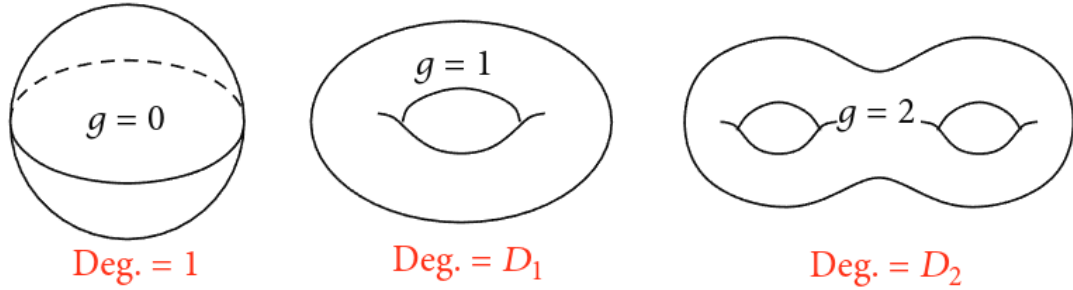


Figure 1.2: Spaces with different topologies, characterized by the genus g . When a wavefunction corresponding to the ground state is wrapped on these different spaces, we get different degeneracies. For example, if wrapped on a sphere the degeneracy is 1^[3].

to be noted that the longitudinal resistivity, R_{xx} , goes to 0 whenever R_{xy} plateaus, which is counter-intuitive, because, classically we expect the Hall potential to balance out the Lorentz Force from the magnetic field and the longitudinal current to flow unhindered. Thus, the phases we see here are new. Each of these new phases are characterised by different integer or fractional numbers, though all of these phases show the same symmetries. Thus, we need a new order parameter to identify these different, interesting phases of matter and this order parameter is the “topological order”^[2].

One way to envision the extraction of the topological order of a quantum system from its ground state wavefunction, is to put the wavefunction on spaces with different topologies as shown in Fig. 1.2 and then measure its degeneracy. For example, if the ground state is wrapped on a sphere, the degeneracy is 1, while for a torus, it will give a different number. Interestingly, this ground state degeneracy is robust against local perturbations. The measure of this kind of ground state degeneracy of gapped systems, defines the notion of topological order. To go from one kind of ground state degeneracy to the other, the energy gap must close. This kind of topological ground state degeneracy arises from the long-range quantum entanglement in the system. The topological order is in fact a pattern of long range entanglement^[4,5]. Recently, it was found that even the phases which have short-range entanglement, though hav-

ing the same symmetries, can belong to the different phases. These phases can be distinguished by Symmetry Protected Topological (SPT) order, where, despite the presence of a bulk gap, degenerate edge or surface states exist, which are protected by the symmetry. Unlike the fractional quantum Hall state, where intricately correlated electronic states demand a quantum many-body approach to derive any understanding, these SPT order states, like the integer quantum Hall effect, can be formulated in terms of single-particle quantum physics. However, in an SPT ordered phase, the perturbations which do not conserve symmetries like $U(1)$ symmetry and time reversal symmetry (TRS) of the system, can destroy the edge or surface states. Hence they are, in the truest of sense, topologically trivial. The presence of topological order means that the state is protected against *any* local perturbation.

This thesis deals with the study of a symmetry protected trivial topological phase, the three dimensional topological insulator, and a non-trivial topological phase, the quantum spin liquid (QSL) phase. In topological insulators, the surface states are not protected under “any” local perturbation. In fact these states are protected only in the presence of $U(1)$ and TRS operators. A QSL, on the other hand, is protected under any local perturbation and hence is topological.

1.2 Topological Insulators

Topological insulators are phases which have a bulk gap, like an ordinary insulator, but host gap-less edge or surface states on their boundaries. The existence of degenerate boundary states in this class of electronic materials are made possible with time reversal symmetry (TRS) and spin-orbit coupling (SOC) operators. This kind of topological insulators are much like another phase that hosts edge states, the integer quantum Hall state. We can understand the topological insulators within the framework of topological band theory.

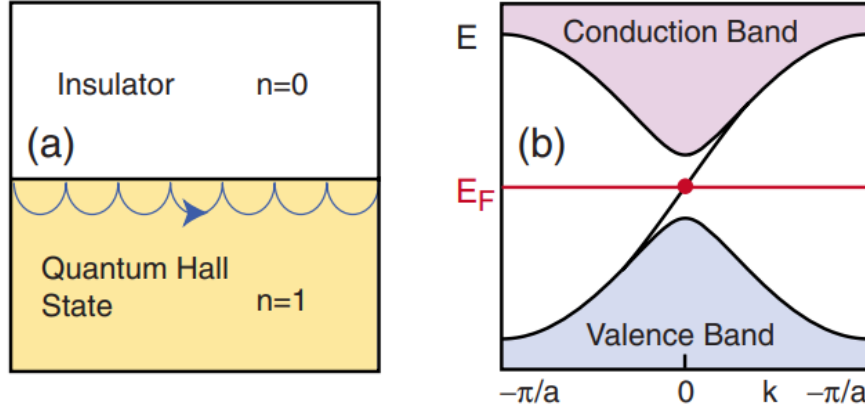


Figure 1.3: a) The skipping motion of electron's cyclotron orbits at the interface between the vacuum and a quantum hall state. b) The edge mode from Haldane's model for graphene in a periodic magnetic field is connecting the valence band and the conduction band by crossing the Fermi level^[6].

1.2.1 Topological Band Theory

The band theory of solids provides a way to describe the electronic states in crystals, by exploiting their translational symmetry to generate the wave functions in terms of the crystal momentum, \mathbf{k} , which exists in a periodic Brillouin zone. In such a case, the Bloch Hamiltonian, $H(\mathbf{k})$, can be used to describe the state. $H(\mathbf{k})$ has Bloch states, $|u_{n\mathbf{k}}\rangle$ as the eigenstates with the corresponding eigenvalues, $E_{n\mathbf{k}}$, which collectively form the well-known band structure of solids. In the band structure description, an insulating state, is characterized by a band gap between the highest occupied band and the lowest unoccupied band. Such a gap exists in semiconductors as well, albeit smaller. The vacuum, according to Dirac's relativistic equation, also has a gap. By tuning the Hamiltonian very slowly, one can in fact, connect the insulating and the semiconducting phases to vacuum.

This situation is not general, in the sense that, all states with a bulk gap cannot be adiabatically connected to vacuum, for example, the integer quantum Hall (IQH) state. When a 2D electron gas (2DEG) is placed in a strong magnetic field, the cyclotron orbits of electrons lead to Landau levels, which are quantised and shows a gap between the occupied and the empty states. However, they are different from an

ordinary insulator, in that, when an electric field is applied to the 2DEG, a current flows, with a Hall conductance, which is quantised,

$$\sigma_{xy} = Ne^2/h \quad (1.1)$$

These phases can be distinguished by an integer, called the Chern Invariant, n , which can be understood in terms of the Berry phase. When \mathbf{k} is varied smoothly in a closed loop, provided there exists no accidental degeneracies, the wavefunction $|u_{mk}\rangle$ acquires a phase, called the Berry phase, given by the line integral of Berry connection, $A_m = \iota\langle u_m|\nabla_k|u_m\rangle$. This can also be defined as the surface integral of $\nabla \times A_m$, called the Berry flux (F_m). The total Berry flux through the Brillouin zone gives the Chern invariant, n_m , given as

$$n_m = \frac{1}{2\pi} \int d^2\mathbf{k} F_m \quad (1.2)$$

The sum of n_m over all the occupied bands

$$n = \sum_m n_m \quad (1.3)$$

remain an invariant even in the presence of degeneracy of bands, if there exists a band gap. This invariant was found to be equal to N - denoting the quantization of Hall conductance - to an accuracy of one part in a billion. To gain a physical understanding of the Chern number, we can draw an analogy to the concept of “genus” defined in geometry. Genus counts the number of holes in a geometrical object. Interestingly, the idea of a doughnut being different from an orange comes from this consideration. The genus is in fact related to the integral of Gaussian curvature over a closed surface, which is quantized and is an integer, according to the Gauss-Bonnet theorem^[7]. The Chern number is thus an integral of a similar curvature, but in the Hilbert space. A non-zero Chern number denotes a non-trivial topological phase.

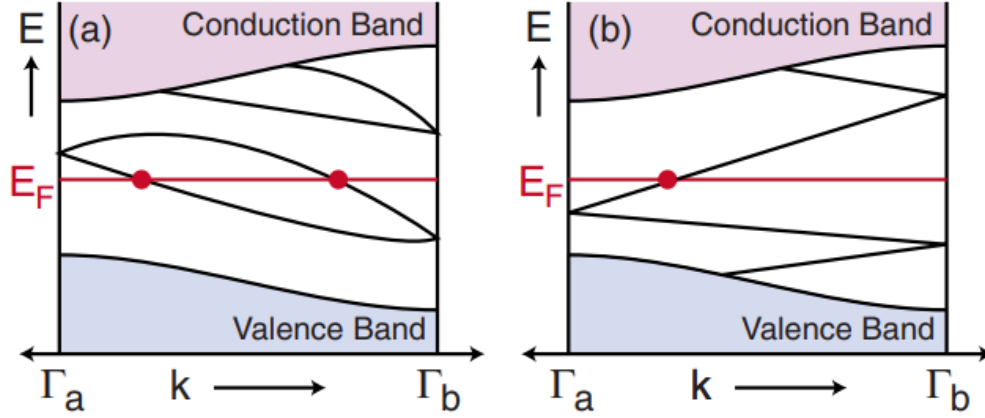


Figure 1.4: The energy dispersion at various crystal momenta. $\Gamma_a = 0$ and $\Gamma_b = \pi/a$ are the time reversal invariant momenta, which are Kramers degenerate. Away from these points the degeneracy is lifted by the SOC. In (a) The bands at Γ_a and Γ_b connect in such a way that the bands intersect the Fermi level an even number of times while in (b) it is odd. The odd number of crossings denote topologically non-trivial phase^[6].

1.2.2 Bulk-Boundary Correspondence

A direct consequence of the non-trivial topological phase is that a system with finite gap would exhibit gap-less conducting states at the boundary. This is known as bulk-boundary correspondence. Such edge states are known to exist at the interface between IQHE state and vacuum. They can be understood by considering the motion of electrons at the boundary. Under the electric field, the electrons undergo a skipping motion along the interface, as their cyclotron orbits reflect off the edge (see Fig 1.3 (a)). These electrons form the edge states in IQHE, which are chiral and are robust against disorder. The Haldane model^[9] on a semi-infinite geometry with the edge placed at $y = 0$ can be used to model the chiral edge states. The dispersion of energy along the edge for this model is shown in Fig 1.3 (b). It clearly shows a single linear band crossing the Fermi energy, connecting the valence and conduction bands with a positive velocity. This represents the edge state at the boundary. The dispersion near the edge can be modified by tuning the Hamiltonian. For instance, the Hamiltonian may be tuned such that the edge states cross the surface three times, with two states having positive group velocity and the third a negative group velocity. For a given

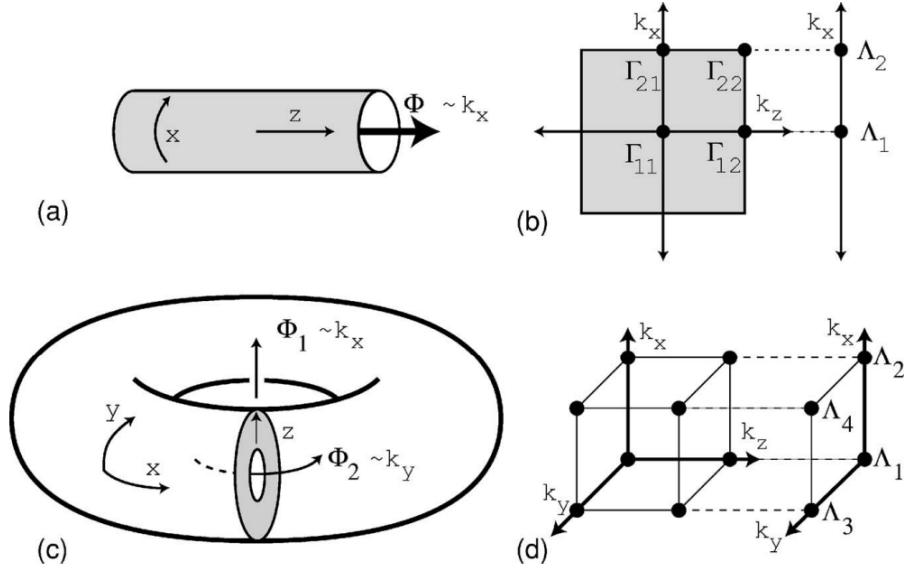


Figure 1.5: (a) A magnetic flux threading a 2D cylinder. If the circumference is a single lattice constant, then this flux corresponds to the crystal momentum, k_x , on the edge. The time reversal invariant fluxes, 0 to $h/2e$, in this case is denoted as Λ_1 and Λ_2 . (b) Λ_a corresponds to the projections of the 4 TRIM in the 2D Brillouin zone. (c) In the 3D generalization, the Corbino torus can be threaded by two fluxes, which corresponds to the crystal momentum on a surface. There are four TRIM points on a given surface, which corresponds to the projection of the 8 TRIM points in a 3D Brillouin zone as shown in (d)^[8]

Hamiltonian, the difference between the number of left moving (N_L) and right moving (N_R) modes, cannot change and this difference gives a change in the Chern number of the system across the interface.

1.2.3 Quantum Spin Hall Insulator

The IQHE states occur in the presence of a magnetic field. This breaks the Time Reversal symmetry (TRS) in the system. There is yet another phase, which is topologically non-trivial, which can be realised even in the absence of a magnetic field, such that the TRS is preserved. This in fact is allowed by the spin-orbit coupling (SOC).

TRS can be represented in the operator form as,

$$T = e^{i\pi S_y / \hbar \kappa} \quad (1.4)$$

where S_y is the spin operator and κ , the complex conjugation. For the case of spin-1/2 electrons, T has the property that $T^2 = -1$. This leads to the Kramer's theorem, which basically says that the eigenstates of a time-reversal invariant Hamiltonian are at least doubly degenerate. If the SOC is absent, then Kramer's degeneracy simply is the degeneracy between up and down spins. However, in the presence of SOC, this degeneracy between up and down spins is lifted at the k-points other than the special k-points which are time reversal invariant. Consider the energy dispersion near the edge of a time reversal invariant 2D insulator as shown in Fig 1.4. The k-points $k_x = 0$ and $k_x = \pi/a$ (same as $k_x = -\pi/a$) are Time Reversal Invariant Momenta (TRIM) and the Kramer's theorem makes sure that the states at these two points are two-fold degenerate. Away from these two points, the degeneracy is lifted. This gives rise to two different ways the states at $k_x = 0$ and $k_x = \pi/a$ can connect pair-wise. Either they can connect such that the bands intersect the Fermi level an even number of times (see Fig. 1.4(a)), or they can connect in such a way that the bands cross the Fermi level an odd number of times, as shown in Fig. 1.4(b). In the former case, the edge states can be eliminated by shifting the Fermi level, while in the latter, the edge states cannot be gotten rid of, meaning they are there to stay and are robust. Thus SOC and TRS together makes the realisation of a quantum spin Hall insulator or a Z_2 topological insulator in 2D. In such systems, the Chern number is zero and a new invariant, a Z_2 invariant - that can take two values, 0 or 1- is defined to identify a quantum spin Hall insulator from a trivial insulator.

Just like the Laughlin thought experiment^[10] of a charge pump to understand the integer quantization in the IQHE, a similar Z_2 pump can be used to gain insights about Z_2 insulators. In his famous thought experiment, Laughlin proposed that if the 2DEG is considered to be a corbino disc, and the magnetic field is threading the middle of this disc, then a change in the magnetic flux by one quanta, hc/e , pumps a charge of e^2/h , across the inner and outer surfaces of the disc. Similar to the case where adding a charge changes the charge polarisation, Fu and Kane defined a

Z_2 quantity, called Time Reversal Polarisation (discussed in detail in section 1.4.5), which characterizes whether Kramer's degeneracy is present or absent on a surface when a charge is added. For a 2D system, we can consider a long cylinder with axis parallel to the reciprocal lattice vector \mathbf{G} , and a circumference equal to one of the lattice constants of the system. Then the analogue of magnetic flux threading the cylinder, $\phi = 0$ and $\phi = h/2e$ are the edge time reversal invariant momenta (TRIM) $k_x = \Lambda_1 = 0$ and $k_x = \Lambda_2 = \pi$. In a quantum spin hall state, the Kramer's pairs switch partners, as the flux threading the cylinder changes or equivalently the crystal momentum changes from 0 to π . The Z_2 invariant is related to this change in the Kramer's degeneracy between $k_x = \Lambda_1$ and $k_x = \Lambda_2$, in the one dimensional edge. As shown in Fig. 1.5(b), $k_x = \Lambda_1$ and $k_x = \Lambda_2$ are projections of the four TRIM points in the 2D Brillouin zone. In the case of 3D, we can consider a "generalized cylinder", which is equivalent to a Corbino donut or torus. In a torus, there are two ways to thread a flux, and each one can be associated with one of the two edges of the surface boundary in 3D, which are perpendicular to \mathbf{G} . There are four TRIM points on a surface (see Fig. 1.5 (c) and (d)), corresponding to the two fluxes being either 0 or $h/2e$ and are projections of the eight TRIM in 3D Brillouin zone.

For a cylinder oriented along \mathbf{G} , the change in time reversal polarisation when the flux changes between λ_1 and λ_2 , can be expressed using the quantities^[8],

$$\delta_i = \frac{\sqrt{\det [w(\Gamma_i)]}}{Pf [w(\Gamma_i)]} = \pm 1 \quad (1.5)$$

where Γ_i corresponds to the TRIM and w is a $2N \times 2N$ (if there are $2N$ occupied levels) unitary matrix given by,

$$w_{mn}(\mathbf{k}) = \langle u_{m-\mathbf{k}} | T | u_{n\mathbf{k}} \rangle \quad (1.6)$$

where T is the time reversal operator with $T^2 = -1$ and $\langle a | T | b \rangle = \langle b | a \rangle$. This allows the definition of a Pfaffian for w , satisfying the condition $\det [w] = Pf[w]^2$.

In 2D there are 4 TRIM points (Γ_i) and a single Z_2 invariant can then be defined as

$$(-1)^\nu = \prod_{i=1}^4 \delta_i \quad (1.7)$$

In 3D, there are 8 TRIM points, leading to four independent Z_2 invariants. One of them can be formulated as the product of all the 8 $\delta(\Gamma_i)$ as

$$(-1)^{\nu_0} = \prod_{i=1}^8 \delta_i \quad (1.8)$$

The other three are given by the product of four Γ_i 's residing on the same plane, as follows,

$$(-1)^{\nu_k} = \prod_{n_k=1, n_{j \neq k}=0,1} \delta_{i=(n_1, n_2, n_3)} \quad (1.9)$$

In the presence of inversion symmetry, a further simplification for the calculation of Z_2 is possible, as shown by Fu and Kane^[8,11]. In this case, the Z_2 invariants can be determined from the occupied bands' parity eigenvalues at the four (in case of 2D) or at the eight (for 3D) TRIM points. Specifically, the δ_i s mentioned above becomes,

$$\delta_i = \prod_{m=1}^N \xi_{2m}(\Gamma_i) \quad (1.10)$$

where ξ_{2m} is the eigenvalue of the parity operator, at the $2m^{th}$ occupied band at the TRIM point, Γ_i . The parity eigenvalue ξ_{2m} can be ± 1 and it shares the same eigenvalue with it's Kramer's partner, ξ_{2m-1} . The calculation of Z_2 invariants in the absence of inversion symmetry requires the explicit calculation of the Time Reversal Polarisation, and a method in terms of Wannier functions is discussed in the computational methods section.

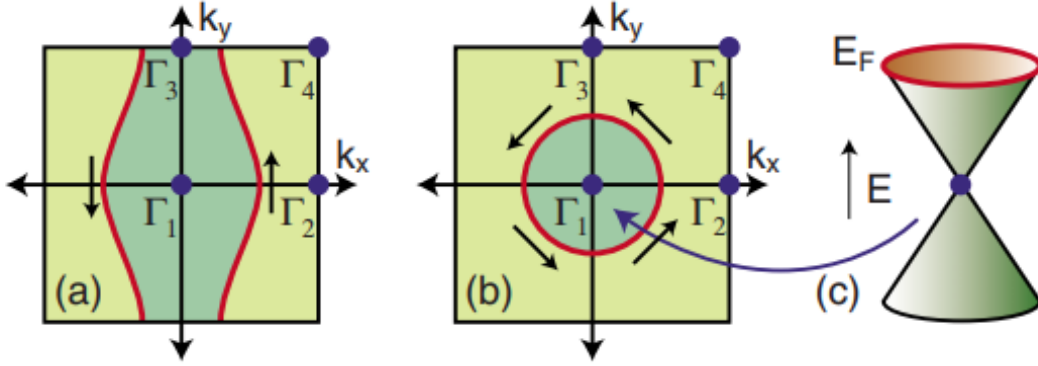


Figure 1.6: a) The surface Fermi surface of a Weak Topological Insulator (WTI). (b) The Fermi surface of a surface of a Strong Topological Insulator. In this case, the Berry phase acquired by the electronic state is π , as the k is changed (c) The Dirac cone present within the Fermi circle.

1.2.4 3D Topological Insulators

As mentioned above, there are 8 TRIM points in 3D, which can be imagined to form the corners of a cube as shown in Fig. 1.5(d). They are given by,

$$\Gamma_{i=n_1n_2n_3} = (n_1\mathbf{b}_1 + n_2\mathbf{b}_2 + n_3\mathbf{b}_3)/2 \quad (1.11)$$

with $n_j = 0, 1$. The δ_i s of any group of four Γ_i , lying on the same plane changes sign under a gauge transformation. There exists 16 invariant δ_i s, modulo these gauge transformations, which leads to 16 classes of topological materials, characterized by four Z_2 invariants, $(\nu_0; \nu_1, \nu_2, \nu_3)$ which are defined above. Since ν_0 is related to the product of δ_i over all the 8 TRIM, it is independent of the choice of \mathbf{b}_i , while ν_1, ν_2, ν_3 are not.

In 3D, one can classify the topological insulators into either a “strong” topological insulator or a “weak” topological insulator. ν_0 , known as the strong index can be used to identify between the two. If ν_0 is 1, it denotes a Strong Topological Insulator (STI) and $\nu_0 = 0$, a Weak Topological Insulator (WTI). The WTI phase can be understood if we consider that a 3D TI is made by stacking two dimensional quantum spin hall insulators. The 2D TIs host edge delocalised modes. As one stacks the QSHIs, these

helical edge states form anisotropic topological surface states. However, the stacking direction is devoid of symmetry protected surface states. This stacking direction, which is topologically “dark”, is in fact denoted by the weak indices (ν_1, ν_2, ν_3) . Unlike the case of a 2D TI, the surface states in the weak topological insulator are not protected by the time reversal symmetry. These states can exist if the surface is clean, but any disorder will lead to the localisation of these states. This is the reason for calling them “weak”. Though they are typically weak, presence of additional symmetries or even the presence of line dislocations can make them robust^[12].

The topological surface states (TSSs) in a strong topological insulator cannot be understood from this analogy. The invariant, ν_0 identifies how many Kramer’s degenerate points are enclosed within the Fermi circle of a surface. In a strong topological insulator, an odd number of Dirac points lie inside the Fermi circle. The simplest case is the presence of a single Dirac point, which can be described using,

$$H_{surface} = -\iota \hbar v_F \vec{\sigma} \cdot \vec{\nabla} \quad (1.12)$$

STIs host TSSs on all their surfaces and these states cannot be localised even in the presence of strong disorder. The Surface States (SS) form a very unique 2D topological metal, which shows very different properties compared to the normal 2D metal. The main difference is that unlike the case of ordinary metal, where the spins are degenerate at all points on the Fermi surface, the spins on the surface of a TI do not show spin degeneracy. The states at \mathbf{k} and $-\mathbf{k}$ should have the opposite spins, as demanded by the TRS. Thus, as one takes \mathbf{k} around the Fermi surface, the spins must rotate around it (see Fig. 1.6). This makes an electron acquire a Berry phase of 0 or π (as required by TRS), after a rotation around the Fermi surface. When an electron goes around a Dirac point, its spin changes by 2π , leading to a Berry phase of π ^[6]. A Berry phase of π leads to non-trivial consequences for the surface states. For instance, in a normal 2D electron gas, the electrical conductivity decreases as the temperature is lowered. This is because of the tendency for Anderson localization in

the presence of disorder^[13]. However, a Berry phase of π adds a weak anti localization term to the conductivity, by changing the sign of the localization correction term to the conductivity^[14]. Thus, the surface states in a strong TI cannot be localised, in fact, even when there is strong disorder.

1.2.5 Applications of Topological Insulators

The unique properties of topological insulators make them promising candidates in many areas of applied physics, especially in the field of electronic and magnetic device technologies. The topologically protected surface states with spin-momentum locking and the presence of Spin-Orbit coupling makes the topological insulators extremely important in the field of spintronics. When a hetero structure between topological insulators and magnets is formed, the non-trivial nature of the TIs can induce a giant spin-orbit torque in the magnet in contact, which can be used in low-power tuning of the magnetism in the material adjacent to the TI, leading to new ways of switching operation. The giant spin-orbit torque is generated because the spin-momentum locking and the large SOC in TIs naturally lead to pure spin currents, when a charge current is passed through it^[15]. This kind of manipulation of magnetism is possible in intrinsic magnetic topological insulators as well, which leads to applications in magnetoelectronics. When there is intrinsic magnetism in a material, the Time Reversal Symmetry is broken, and thus the surface states of topological insulators become gapped and a magnetoelectric effect arises, which basically means that a magnetic polarization can be induced by an external electric field and an electric polarization by a magnetic field.

Another research area where topological insulators can be used is the field of optoelectronics. Topological insulators are known to have near-infrared transparency^[16] and ultra broadband plasmon excitations^[17]. Moreover, recent studies have shown that the refractive index on the surface of a topological insulator is much less as compared to the bulk refractive index^[18]. All these properties can be used in various

optical devices including optical recording, sensors, waveguides, solar cells etc.

Yet another application of topological insulators is in the quantum information and quantum computing. In quantum computing, quantum mechanical features like superposition and entanglement are exploited to do operations on data. These operations are very difficult to implement in a classical computer. The data is represented in the basis of “qubits” or quantum bits, just like bits in classical computers. However, the present realisations of such qubits, like superconductors and trapped ions, are extremely susceptible to their external environment. A topological insulator in the proximity of a superconductor or a topological insulator with intrinsic superconductivity, can host Majorana fermions, which obey non-Abelian anyonic statistics. If the information is stored in such quasiparticles, the operations are then “braiding” of these anyons and they are much more robust against local perturbations, making them extremely useful in obtaining qubit implementations that are resistant to decoherence and noise.

Topological Insulators find utility in the field of thermoelectrics as well. The efficiency of thermoelectric materials is quantified using the thermoelectric figure of merit, a dimensionless quantity, given by $zT = S^2\sigma/(\kappa_e + \kappa_{ph})T$, where S is the Seebeck coefficient, σ , the electrical conductivity and κ , the thermal conductivity. Out of S , σ , κ_e and κ_{ph} , κ_{ph} is fairly independent of the others, while the electrical terms are not independent of each other. Hence, the field of thermoelectrics mainly tries to tune the lattice thermal conductivity, κ_{ph} to improve the figure of merit. The topological insulators, however offer a novel way to tune the zT . The TIs have robust surface states, which cannot be back scattered, which means that, these states remain conducting even in the presence of dopants. Effective tuning of phonons using such chemical processes thus leave the conductivity unaffected, leading to new ways of obtaining good thermoelectrics.

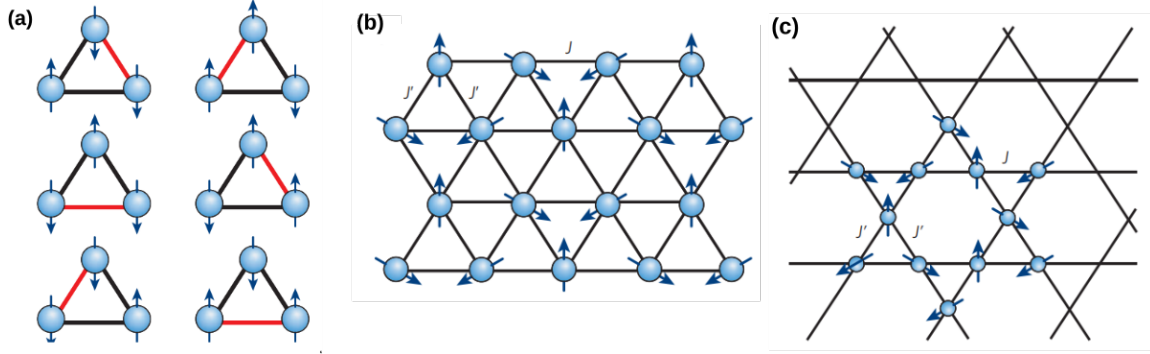


Figure 1.7: (a) Ising spins on a triangle with antiferromagnetic exchange. There are six possible ways the spins on this lattice can arrange. (b) A 2D triangular lattice formed from the triangular motifs shown in (a). (c) A 2D Kagome lattice^[19].

1.3 Quantum Spin Liquids

A quantum spin liquid is another exotic phase which has been studied greatly in condensed matter physics. This phase is characterized by short range magnetic order and long range magnetic entanglement with fractionalized spin excitation with a finite gap, which arises not from spontaneous symmetry breaking phenomena. The search for the quantum spin liquid system has been there in the literature for a decade and only a few candidates quantum spin liquids have been identified.

The quantum spin liquid is a system of highly-correlated spins which evade long-range magnetic order at very low temperature or even $T = 0K$, because of strong quantum fluctuations. An essential ingredient of a QSL phase is an anomalously high degree of long-range entanglement. The idea of long-range entanglement is still an intensely researched field in condensed matter physics and a concrete description is still lacking. However, a highly entangled state can loosely be described as a state which cannot be connected to a product state smoothly, over any spatial block of finite dimension. One way to coarsely classify them is based on whether the excitation spectrum has a finite gap between the ground state and the excited state or not. Gapped QSL phases are simpler to study theoretically and can be characterized by a topological order, which is a representation of patterns of long-range entanglement.

Unlike the case of topological insulators, where the word “topology” derives from “geometric” topology (where we talk about the equivalence of a doughnut and coffee mug), the “topology” in topological order is algebraic topology. The QSL phase hosts exotic excitations with fractional quantum numbers and emergent gauge fields.

Let us dive a little deeper into the topic, by first looking at the anti-ferromagnetic ordering in normal magnets. With the advent of quantum mechanics, Heisenberg explained magnetism by proposing that neighbouring spins can have short range interactions via quantum super-exchange interactions. Néel argued that if this exchange is negative, it leads to an alternating up-down arrangement of spins at low temperatures, known as the Néel antiferromagnet, which was initially thought to be unstable because of fluctuations, until it was observed experimentally. Nonetheless, P. W. Anderson came up with the idea that this kind of anti-ferromagnetic long-range order can be destroyed if the spin system is “frustrated”^[20]. A prototypical example of such a frustrated system is the 2D triangular Ising spin lattice with antiferromagnetic interaction between the nearest neighbours. An isolated triangular motif in this system, can have six different ways in which the spins can orient with respect to each other as shown in Fig. 1.7 (a). When these triangular motifs form an extended lattice (see Fig. 1.7 (b)), Wannier showed that the ground state has a very large degeneracy^[21]. The spins fluctuate between these different possible degenerate states as the temperature is lowered, but in a collective manner, since the spins are confined to the ground state of the Ising antiferromagnet. This state is called a spin liquid and can be compared to an ordinary liquid, where the molecules form a highly correlated, dense state, which shows no signs of static order. How frustrated can a system be? A measure of the degree of frustration is provided by a quantity called the “frustration parameter”, f . It is given by the ratio of the Curie-Weiss temperature, θ_{CW} , to the ordering temperature T_C . According to the Curie-Weiss law, the magnetic susceptibility is related to the temperature as $\chi = C/(T - \theta_{CW})$, where θ_{CW} sets the scale of ordering temperature in ordinary magnets. If there exists frustration in the system,

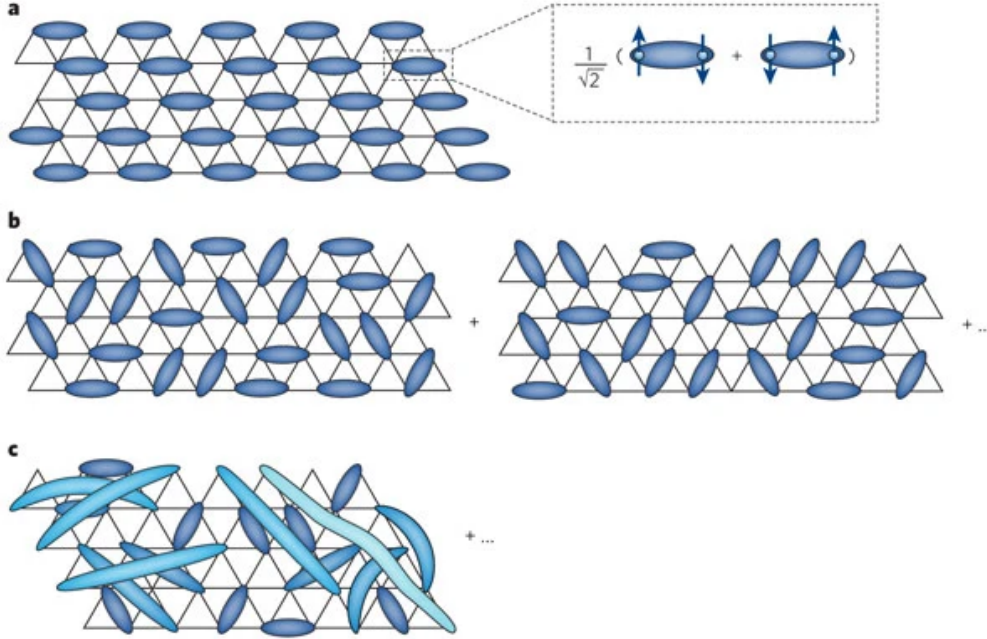


Figure 1.8: (a) The valence bond state. The inset shows an entangled pair of spins, forming a valence bond. The VBS represents one arrangement of such valence bonds. (b) The superposition of VBS states gives a resonating valence bond state. The entanglement in (a) and (b) is short range. (c) The light blue valence bonds represent long range entanglement, which are less tightly bound and hence can be excited easily into a state with non-zero spin^[19].

the ordering temperature is generally suppressed and f gives a measure of how much it is suppressed and we say that a spin liquid regime exists at temperatures below $|\theta_{CW}|$, which in some cases can exist all the way up to $T = 0 \text{ K}$.

The spins are defined in magnitude as half-integers of \hbar . The fluctuations experienced by these spins can be either classical or quantum, depending on their magnitude. If the spins are classical, meaning large spins, the classical or thermal fluctuations dominate. When such a system has enough thermal energy, the spins fluctuate in a random fashion. These fluctuations decrease with the lowering of temperature and the spins finally freeze into a random configuration or order at very low temperatures. However, if the spins are quantum spins, with $S = 1/2$, the quantum mechanical fluctuations - which are basically zero-point motions produced by the uncertainty principle - that persist down to very low temperatures, become

comparable to their sizes. These spins, though thermal fluctuations are absent, will be “tossed around” by the quantum fluctuations, even till 0 K. Unlike the thermal fluctuations, the quantum fluctuations have the property of phase coherence. Strong quantum fluctuations leads to a QSL phase, where the ground state is a state of massive superposition. Locally the QSL has well-formed magnetic moments, however, the ground state somehow is non-magnetic.

A non-magnetic state can be thought to be build out of a lattice of valence bonds, which are a pair of spins that form a singlet which has a total spin of 0. (see Fig 1.8). Such a spin singlet state is highly entangled and a lattice in which all the spins form a part of a valence bond, naturally will have ground state which is non-magnetic, with $S = 0$. Each spin in a valence bond state (VBS) is highly entangled to it's partner in the valence bond. Though such VBS states exist in a lot of materials, they are not exactly QSL states, since they tend to break lattice symmetries and are not long-range entangled. If we consider quantum fluctuations on these valence bonds, which makes the spins fluctuate between different valence bond partitions, we get a Resonating Valence Bond (RVB) state, which is a “liquid” VBS. The RVB state is thus a superposition of various valence bond states possible in a system. Each VB partition can have a different weight. This gives a plethora of possible RVB ground states, which lead to distinct QSL phases. It was shown that the spins on a triangular lattice order at 120° angle, making the RVB theory not an explicit theory of QSL. However, Anderson showed a connection between the QSL phase and the Cooper pairs in superconductivity, rejuvenating the studies on spin liquid theory.

Now we know that a host of QSL phases exist, possibly an infinite number of them. Classifying the QSL phases is a very active field of research in condensed matter physics. A common signature in all the different number of QSL phases is that they support excitations that are quite exotic. If a valence bond in an VBS state is broken, we get an excited state, a triplet. This gives rise to gapped bosonic excitation called, triplon, which is what is expected in the system. If we now imagine a VB

between two spins that are far apart, it can be broken into free-spins, with very low energy. These excitations are called spinons, which have half-integral spins. Usually the excitations seen in materials are either electron-like, with spin $1/2$ and charge e or magnon-like, with spin 1 and charge 0. A common deviation from such excitations is observed in the Fractional Quantum Hall (FQH) state, where the excitations carry quantum numbers that are fractional. Similarly, the spinons in a QSL state, are neutral quasi particles with a spin of $1/2$. They are quite important in the experimental verification of QSLs. It can be viewed as if a $S = 1$ magnon has split into two spinons with $S = 1/2$. This is an example of *fractionalization*. A systematic way to examine whether such a fractionalization occur in a spin model was proposed by Wen^[22,23], using the concepts of confinement and deconfinement in lattice gauge theory, which is outside the scope of this thesis. Detecting these particles is a very difficult task, because the fractional nature of the spinons prohibits the formation of a single spinon. The smoking gun evidence of the presence of spinons in a system is the presence of broad and diffuse neutron scattering peaks which arise from probing the two particle continuum.

1.3.1 Candidates for Quantum Spin Liquids

There have been numerous reports on possible candidates of QSL phase in the last few years. The evidence, however, is circumstantial. The search for QSL systems have been majorly in systems with spin- $1/2$, which frustrate the Neel antiferromagnetic order. Interests are also directed at low dimensional systems and systems with low coordination number, where the quantum fluctuations are enhanced. There are also the cases of pyrochlore and hyper-kagome lattices in 3D, where the magnetic long range order is suppressed by geometric frustration. Another interesting place to look for QSL phases is in the weak Mott Insulators, close to the metal-insulator transitions, for example $(V_{1-x}Cr_x)_2O_3$ ^[27]. Let us look at some examples of QSL candidates with $S = 1/2$ or an effective $J = 1/2$ spins.

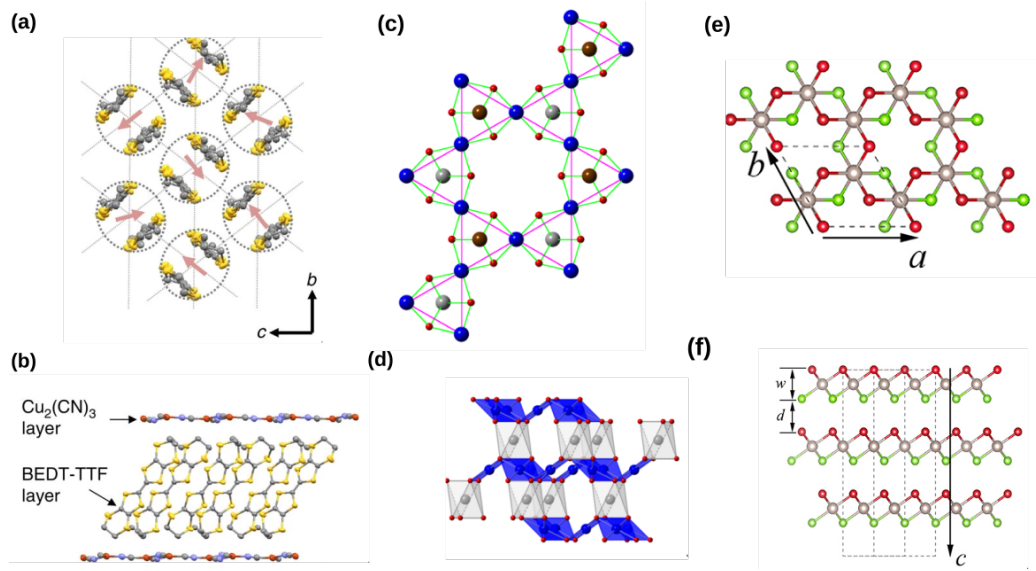


Figure 1.9: (a) and (b) The crystal structure of κ -(ET) $_2$ Cu $_2$ (CN) $_3$, (a) where the ET dimers form a triangular lattice. The $S = 1/2$ spin per dimer is shown as red arrow. (b) These ET molecules are stacked between layers of Cu $_2$ (CN) $_3$ ^[24] (c), (d) Herbertsmithite structure, with the Cu atoms forming layers of Kagome lattice, which are interconnected by Zn^[25] and (e), (f) α -RuCl $_3$, where the Ru atoms arrange in honeycomb layers which are weakly coupled with Cl^[26]

Herbertsmithite, ZnCu $_3$ (OH) $_6$ Cl $_2$, is a rare mineral, where the Cu $^{2+}$ ions form a Kagome lattice Fig. 1.9(b). The magnetic measurements on this system showed no signatures of long-range magnetic order. Furthermore, the neutron diffraction studies revealed broad continuum of spin excitations in the system, signaling fractional excitations.

Another example is the class of 2D Organic salts, in which structural dimers, having a single spin-1/2 degree of freedom, form triangular lattice. Some prominent examples include κ -(BEDT-TTF) $_2$ Cu $_2$ (CN) $_3$ (See Fig. 1.9), called κ -ET, EtMe $_3$ Sb[Pd(dmit) $_2$] $_2$ (Pd-dmit), κ -H $_3$ (Cat-EDT-TTF) $_2$ and κ -(BEDT-TTF) $_2$ Hg(SCN) $_2$ Br. NMR measurements on κ -ET shows that it lacks long-range magnetic order, well below the Curie-Weiss temperature. The spin susceptibility becomes a constant at low temperatures, and the heat capacity shows a linear temperature dependence^[28].

The Inelastic Neutron Scattering (INS) experiments on α -RuCl $_3$, also revealed a continuum of spin excitations^[29], suggesting a QSL phase. It was observed that the

application of magnetic field in this system suppresses magnetic order, implying there could be a range of magnetic fields where the spin liquid could exist^[30].

A recent interest, with respect to realising a QSL phase, is in the Rare-Earth based compounds. An interplay of spin-orbit coupling, exchange anisotropy, spin correlations and frustration in Rare-Earth materials, make them unique quantum materials. One such example is YbMgGaO_4 . In this material the magnetic Yb atoms form a triangular lattice with the Mg and Ga atomic sites having disorder. Extensive studies have been performed on this system^[31–33], which point to a spin liquid state. However, like most of the existing candidates, disorder plays a huge role in this material. The Mg and Ga cations interchange and thus distort the Yb environment^[33]. Another example is the $\text{Ce}_2\text{Zr}_2\text{O}_7$ ^[34,35], where Ce^{3+} ions, with an effective $S = 1/2$, occupy a lattice made of corner sharing tetrahedra. Replacing Zr with Sn, gives another QSL candidate $\text{Ce}_2\text{Sn}_2\text{O}_7$ which has been categorized as a $U(1)$ spin liquid^[36].

In this thesis we report two Yb-based rare-earth oxides, $\text{Yb}_2\text{Te}_5\text{O}_{13}$ and NaYbW_2O_8 , the former a dimer-based lattice and the latter a hyperhoneycomb lattice.

1.3.2 Applications of QSL

The most important application of Quantum Spin Liquids is in the field of quantum computation and quantum information processing. The QSL phases have long-range quantum entanglement in their ground state and support fractional excitations, like Majorana fermions. These particles can behave like anyons, which obey non-Abelian statistics, in the presence of a magnetic field^[37,38]. When these excitations move around each other, it is known as braiding, and this braiding can be used to perform unitary operations. Measurements in such system can be done by observing the fusion of such excitations in pairs. Kitaev argued that^[37] such a quantum computer is fault-tolerant, against external environment, by its physical nature. This makes QSLs lucrative in the field of quantum computing.

1.4 Computational Methods

A brief review of the basic theoretical formalism used in the simulations in this thesis is described in this section. First, we discuss the density functional theory, followed by a review of the tight-binding model and wannierization. We conclude this section with the topic of time reversal polarisation and how it can be used to classify band topological insulators.

1.4.1 Density Functional Theory

An important aspect of quantum mechanical studies on materials is to find the solution of the non-relativistic many-body time dependent Schrödinger equation,

$$\hat{H}\Psi = E\Psi \quad (1.13)$$

where \hat{H} is the many body Hamiltonian and Ψ and E are the eigenvector and the eigenvalue of this \hat{H} respectively. The many-body wavefunction, Ψ , contains all the information about the system and the energy of the system is given by eigenvalue E . For a general system consisting of n_e electrons and N_I nuclei, the non-relativistic Hamiltonian is given by,

$$\begin{aligned} \hat{H} = & - \sum_i^{n_e} \frac{\hbar^2}{2m_e} \nabla_i^2 - \sum_I^{N_I} \frac{\hbar^2}{2m_I} \nabla_I^2 - \sum_i^{n_e} \sum_I^{N_I} \frac{Z_I e^2}{|r_i - R_I|} \\ & - \sum_i^{n_e} \sum_{j>i}^{m_e} \frac{e^2}{|r_i - r_j|} - \sum_I^{N_I} \sum_{J>I}^{N_I} \frac{Z_I Z_J e^2}{|R_I - R_J|} \end{aligned} \quad (1.14)$$

where the first two terms correspond to the kinetic energy of the electrons and the nuclei respectively, with m_e being the mass of the electron and m_I , the mass of the nuclei. The third term captures the interaction between the nuclei and the electron, while the last two terms correspond to the electron-electron interaction energy and the interaction between two nuclei respectively. The charge of an electron is e and

$Z_I e$ corresponds to the charge of a nucleus. The Hamiltonian can thus be re-written in a compact form as:

$$\hat{H} = \hat{T}_e + \hat{T}_N + \hat{V}_{ext} + \hat{V}_{ee} + \hat{V}_{nn} \quad (1.15)$$

The term containing the electron-nuclei interaction is denoted as the external potential. The solution of the above equation becomes cumbersome as we consider a system with more than one electron. In such cases, which is in fact the most observed case, one has to resort to an efficient way of solving Schrödinger equation, which involves some approximations. The first approximation to discuss is the Born-Oppenheimer approximation.

In the Born-Oppenheimer Approximation, the nuclei is considered to be infinitely heavier than the electron, which renders the motion of nuclei quite negligible as compared to the electronic motion. Hence, we can assume the nuclei to be stationary, while the electrons move and reorganise themselves around the nuclei. As a consequence the electronic part and the nuclear part of the Schrödinger can be decoupled. Mathematically, the total wavefunction of the time independent Schrödinger equation can then be written in a separable form, as the product of an electronic wavefunction and a nuclear wavefunction as,

$$\Psi_{tot}(r_i, R_I) = \Psi_e(r_i, \{R_I\})\Psi_N(R_I) \quad (1.16)$$

the electronic wavefunction, Ψ_e depends on the nuclear positions R_I parametrically. This wavefunction represents the electronic states for a fixed configuration of nuclei. The separation of variables allow us to write Eq. 1.14 as two different equations, an

electronic part,

$$\begin{aligned} & \left[- \sum_i^{n_e} \frac{\hbar^2}{2m_e} \nabla_i^2 - \sum_i^{n_e} \sum_I^{N_I} \frac{Z_I e^2}{|r_i - R_I|} - \sum_i^{n_e} \sum_{j>i}^{n_e} \frac{e^2}{|r_i - r_j|} - \sum_I^{N_I} \sum_{J>I}^{N_I} \frac{Z_I Z_J e^2}{|R_I - R_J|} \right] \Psi_e(r_i, \{R_I\}) \\ & = U_e(\{R_I\}) \Psi_e(r_i, \{R_I\}) \end{aligned} \quad (1.17)$$

and a nuclear part,

$$\left[- \sum_I^{N_I} \frac{\hbar^2}{2m_I} \nabla_I^2 + U_e(\{R_I\}) \right] \Psi_N R_I = E \Psi_N R_I \quad (1.18)$$

where $U_e(\{R_I\})$ dependent on the nuclear coordinates is called the electronic energy and E is the total energy of the system. This is the potential energy surface that the nuclei feels and thus enters the nuclear Schrodinger equation (Eq.1.18). Thus, the Born-Oppenheimer approximation reduces the difficulty in solving the full many-body Schrödinger equation.

Though the BO approximation greatly simplifies the Schrödinger equation and forms the basis of many electronic structure calculations, solving the many-body electronic Schrödinger equation itself comes with it's own set of difficulties. For instance, further approximations to the many-body, N electron wavefunction.

Consider an n -electron system under the influence of a single nucleus or a collection of nuclei, like an atom, a molecule or a solid. The Hamiltonian is given by,

$$\hat{H} = \hat{T}_e + \hat{V}_{ext} + \hat{V}_{ee} \quad (1.19)$$

The nuclei-nuclei interaction term is usually neglected while considering Eq.1.17, because it can be solved separately and added in the end as a constant energy term. If Ψ is not an eigenvalue of the above Hamiltonian, then it does not have a well-defined energy. In this general case, the energy expectation value can be calculated

by solving the following integral,

$$\begin{aligned}\langle \Psi | \hat{H} \Psi \rangle &= \int_{r_1} \int_{r_2} \dots \int_{r_{n-1}} \int_{r_n} \Psi^* \hat{H} \Psi \, dr_1 dr_2 \dots dr_{n-1} dr_n \\ &= \langle \Psi | \hat{T}_e + \hat{V}_{ee} \rangle + \langle \Psi | \hat{V}_{ext} | \Psi \rangle\end{aligned}\quad (1.20)$$

Let us look at the electron-nuclei interaction term,

$$\begin{aligned}\langle \Psi | \hat{V}_{ext} | \Psi \rangle &= \int_{r_1} \int_{r_2} \dots \int_{r_n} \Psi^* \left(\sum_i^n v_i(\vec{r}_i) \right) \Psi \, dr_1 dr_2 \dots dr_n \\ &= \sum_i^n \int_{r_1} \int_{r_2} \dots \int_{r_n} v_i(r_i) |\Psi|^2 dr_1 dr_2 \dots dr_n\end{aligned}\quad (1.21)$$

where, v_i is the one electron term of the external potential, \hat{V}_{ext} . Because of the fact that $v_i(r_i)$ is the same for all electrons and $|\Psi|^2$ is symmetric under position exchange, all the terms in the above summation are equivalent and we can write the above as,

$$\langle \Psi | \hat{V}_{ext} | \Psi \rangle = n \int_{r_1} v_i(r_1) \left(\int_{r_2} \dots \int_{r_n} |\Psi(r_1, r_2, \dots, r_n)|^2 \, dr_2 \dots dr_n \right) dr_1 \quad (1.22)$$

Now, the one-electron density, for a system with normalized wavefunction Ψ is given by integrating the probability density $|\Psi|^2$ with respect to all the electronic coordinates r_i , except one. And that is exactly the term

$$\int_{r_2} \dots \int_{r_n} |\Psi(r_1, r_2, \dots, r_n)|^2 dr_2 \dots dr_n$$

in the above equation. Thus, Eq. 1.22, gets modified as,

$$\langle \Psi | \hat{V}_{ext} | \Psi \rangle = \int_{r_1} v_1(r_1) \rho(r_1) dr_1 \quad (1.23)$$

The electron-nuclei term is thus a functional of density ρ . The same applies to any other operator which is the sum of multiplicative single electron operators.

The Hohenberg-Kohn Theorems

P. Hohenberg and W. Kohn proved two theorems in 1964^[39], which paved the way for Density Functional Theory (DFT).

Theorem 1 : *The external potential is a unique functional of the ground state electron density, upto a trivial additive constant.*

This theorem immediately follows that given the ground state electronic density, the Hamiltonian can be uniquely determined and thus the wavefunction and all the materials properties could be computed.

Theorem 2 : *For any positive definite density, such that $\int \rho_p(r)dr = N$, then $E[\rho_p] \geq E_0$*

This theorem establishes a variational principle and restricts density functional theory to exploration of the ground state.

Now Eq. 1.19 can be written in terms of the functional as,

$$E[\rho] = T[\rho] + V_{ext}[\rho] + V_{ee}[\rho] \quad (1.24)$$

The interaction of the electron with external potential is trivial and discussed above, however, the kinetic energy term, $T[\rho]$ and the electron-electron interaction term, $V_{ext}[\rho]$ are not known. We have to resort to approximations of these functional and provided we can approximate it well enough, a direct minimisation of the above equation with respect to the density would give the ground state properties of the system.

The Kohn-Sham approach

The kinetic energy functional and the electron-electron interaction functional in Eq. 1.24 was approximated by Kohn and Sham^[40] by considering a fictitious system of non-interacting N-electrons, whose ground state density resembles that of the interacting case, which is of interest to us. The fictitious system is described by a single

determinant of N orbitals, f_i , such that the ground state density $\rho(r)$ is given by,

$$\rho(r) = \sum_i^N |f_i|^2 \quad (1.25)$$

The kinetic energy of this fictitious system can be obtained directly as

$$\hat{T}_s = \frac{\hbar^2}{2m_e} \sum_i^N \langle f_i | \nabla^2 | f_i \rangle \quad (1.26)$$

It is also noteworthy that the major contribution in the electron-electron interaction term, $\hat{V}_{ee}[\rho]$ is the classical Coulomb interaction or the Hartree energy,

$$V_H[\rho] = \frac{1}{2} \int \frac{\rho(r_1)\rho(r_2)}{|r_1 - r_2|} dr_1 dr_2 \quad (1.27)$$

Thus, we can rewrite the energy functional in Eq. 1.24 as,

$$E[\rho] = T_s[\rho] + V_{ext}[\rho] + V_H[\rho] + E_{xc}[\rho] \quad (1.28)$$

where $E_{xc}[\rho]$ is the exchange-correlation functional introduced to capture the error in the kinetic energy because of considering non-interacting electron-system and the error due to the consideration of the electron-electron interaction classically. So, E_{xc} can be written as,

$$E_{xc}[\rho] = (T[\rho] - T_s[\rho]) + (V_{ee}[\rho] - V_H[\rho]) \quad (1.29)$$

Writing the energy functional explicitly in terms of the density of the non-interacting system of electrons and by applying variational theorem, we can get the orbitals that minimise the energy functional, which satisfy the following set of differential

equations,

$$\left[-\frac{\hbar^2}{2m_e} \nabla^2 + v_{ext}(r) + \int \frac{\rho(r')}{|r - r'|} dr' + v_{xc}(r) \right] f_i(r) = e_i f_i(r) \quad (1.30)$$

where v_{xc} is a local multiplicative potential, which is a functional derivative of $E_{xc}[\rho]$ with respect to density,

$$v_{xc}(r) = \frac{dE_{xc}[\rho]}{d\rho} \quad (1.31)$$

Though the Kohn-Sham equations have the same basic form as that of the Hartree-Fock equations, note that the Kohn-Sham equations have an exchange correlation potential unlike the Hartree-Fock equations which have just the exchange potential. Moreover, the exchange correlation potential in Kohn-Sham equations have a component of kinetic energy and not just the sum of exchange and correlation.

Thus the Kohn-Sham approach maps the ground state of many-body interacting system of electrons to the density of a non-interacting system of electrons and this mapping is exact if the exact exchange-correlation functional is known. However, we do not know the exact exchange-correlation functional. Nevertheless, this functional does not depend on the specific material that is studied, that is, it is a universal functional. The determination of the exact properties of this universal functional in some systems, allows us to approximate the form of this functional to some accuracy. Below I will discuss some of the most commonly used approximations to the exchange-correlation functional.

1.4.2 Approximations to the Exchange Correlation Functional

Local Density Approximation

In the Local Density Approximation (LDA), the exchange correlation functional for a spin unpolarised system is given by,

$$E_{xc}^{LDA}[\rho(r)] = \int \epsilon_{xc}(\rho(r)) \cdot \rho(r) dr \quad (1.32)$$

where $\epsilon_{xc}(\rho(r))$ is the exchange-correlation energy per particle of a uniform electron gas with density $\rho(r)$. In other words, LDA replaces the local density of an inhomogeneous system at each point with the density of a homogeneous electron gas which has a density equal to the local density of the system at that point. This has been accurately calculated from quantum Monte Carlo simulations by Ceperley and Alder^[41] and parameterized by Perdew and Zunger^[42] to give an analytic form. For a spin-polarised system, LDA can be generalized to a Local Spin Density Approximation (LSDA), as follows:

$$E_{XC}^{LSDA}[\rho_{\uparrow}(r), \rho_{\downarrow}(r)] = \int \epsilon_{xc}(\rho_{\uparrow}(r), \rho_{\downarrow}(r)) \cdot \rho(r) dr \quad (1.33)$$

This approximation, by construction, yields very accurate results for systems which have a slowly varying or uniform electron density, but is not a good approximation for the systems with highly in-homogeneous density like atoms or molecules. Nonetheless, LDA seems to work much better than anticipated for a host of materials, at least qualitatively. For example, in molecules, LDA overestimates the binding energies, while providing reasonably good results for vibrational frequencies and equilibrium distances. A striking disadvantage of LDA is its consistent lack of agreement with the experiments, on the band gap in semiconductors and insulators. LDA always underestimates the band gap, at least by a difference of two. In order to overcome the limitations of LDA, a number of other approximations to the exchange-correlation

functional have been developed.

Generalized Gradient Approximation

The Generalized Gradient Approximation (GGA) to the exchange correlation functional aims to correct the errors because of LDA, by considering the exchange correlation energy to depend on the gradient of the local spin density as well. This semi-local approximation to the exchange correlation functional can be written as

$$E_{xc}^{GGA}[\rho_{\uparrow}(r), \rho_{\downarrow}(r)] = \int \epsilon_{xc}(\rho_{\uparrow}(r), \rho_{\downarrow}(r), \nabla \rho_{\uparrow}(r), \nabla \rho_{\downarrow}(r)) \rho(r) dr \quad (1.34)$$

The success of GGA comes from its abilities to get rid of some of the disadvantages of LDA, at a modest computational load. A host of generalized gradient approximations to the exchange correlation functional have been proposed, most notably by Perdew-Burke^[43,44], Perdew-Wang^[45] and Perdew-Burke-Ernzerhof^[46]. Though the GGA improve upon LDA in many aspects, it still harbors various drawbacks like the underestimation of band gap in semiconductors.

Hybrid Functionals

The predominant contribution to the total exchange-correlation energy is the exchange energy of electrons with the same spin. It is only reasonable in this case to expect a better result if the semi-local exchange functional is replaced with the exact Hartree-Fock exchange energy. The major advantage of this formalism is the total elimination of the “self-interaction” energy, a non-physical and absurd energy that an electron experiences from itself, which is compensated only partially in the semi-local approximations. The correlation energy in DFT, considers only the dynamic correlation and the exchange energy in DFT takes into account the non-dynamic correlation. However, if we consider the exchange to be the exact exchange, this non-dynamic correlation is lost, as it only includes the correlation of Fermi electrons with identical

spins. In order to ensure a balance between the elimination of the Self-Interaction Error and the inclusion of the non-dynamic correlation, a linear combination of exact exchange and semi-local exchange is used, and this is the hybrid functional,

$$E_{xc}^H = a_0 E_x^{Exact} + (1 - a_0) E_x^{DFT} + E_c^{DFT} \quad 0 \leq a_0 \leq 1 \quad (1.35)$$

One of the most widely used hybrid functional is Becke's three parameter scheme (B3) where the exchange-correlation is approximated as,

$$\begin{aligned} E_{xc}^H &= a_0 E_x^{Exact} + (1 - a_0) E_X^{LDA} + a_x \Delta E_x^{B88} + E_c^{LDA} + a_c \Delta E_c^{GGA} \\ a_0 &= 0.2, a_x = 0.72, a_c = 0.81, \end{aligned} \quad (1.36)$$

where, ΔE_x is the gradient correction to the exchange energy taken from B88 functional^[44] and ΔE_c^{GGA} is the gradient correction to the correlation energy. The parameters a_0 , a_x and a_c were obtained by fitting to experimental observations. The B3LYP functional is based on the same, but with the Lee-Yang-Parr correlation functional^[47]. Though extremely useful in the case of molecules, the hybrid functionals are not very suitable for solids.

The two types of systems studied in this thesis are chalcogenides and rare-earth oxides. The presence of partially filled d- and f-orbitals in these systems lead to strong correlation effects. Using DFT to study such strongly correlated systems pose two main challenges, because of the approximations to the exchange-correlation functional - one is the delocalization or the self interaction error, and the other is the static correlation error. If standard, starting approximations, like LDA or GGA to the exchange-correlation functional is used, it can lead to the failure of DFT in strongly correlated systems.

All our theoretical results are compared with contemporary studies on similar systems and is carefully fine tuned. For example, in TaSe₃, the existence of a negative band gap of around 20 meV is experimentally observed^[48] and in our GGA calcu-

lated band gap with SOC, we observe a negative gap of around 16 meV. In the case of Sb_2Te_3 , the presence of a single Dirac cone at the Γ -point on its surfaces are reported in multiple studies^[49,50], both experimental and theoretical and this is indeed what we observe in our studies as well. With the confidence gained from this calculation, we proceed to analyse the topological character of the other members of the series. When it comes to the magnetic rare-earth oxide systems, we have implemented a DFT+U+SOC approach, where a semi-empirical correction to the delocalization error is included with the Hubbard U correction. Moreover, rather than emphasizing the absolute value of the magnetic exchanges (which are the only quantities we have obtained from DFT), we are interested in the ratio of the exchanges and the magnetic properties are further calculated within a Monte-Carlo framework. The main point to remember is that all the works presented in the thesis are not stand-alone theoretical studies. Our computational analysis is complimented by experiments and are designed to explain the experimental observations.

1.4.3 Tight Binding Model

The general electronic Hamiltonian can be written as

$$\hat{H} = \hat{H}_e + \hat{H}_{ei} \quad (1.37)$$

where, \hat{H}_{ei} is the electron-ion interaction term. If we neglect the electron-electron interactions terms contained in \hat{H}_e , we get the single electron Hamiltonian

$$\hat{H}_0 = \frac{\hat{p}^2}{2m} + V(\hat{r}) \quad (1.38)$$

where $V(\mathbf{r})$ is given by,

$$V(\mathbf{r}) = \sum_j V_{ion}(\mathbf{r} - \mathbf{R}_j) \quad (1.39)$$

This is the background ionic potential landscape that the single electron experiences, which is periodic by construction. Thus, the single particle Hamiltonian \hat{H}_0 commutes with the translation operator \hat{T} , thereby making the eigenstates of \hat{T} , simultaneous eigenfunctions of \hat{H}_0 as well. According to the Bloch's theorem, the eigen states of \hat{T} lies on a unit circle in the complex plane, of the form,

$$\Psi_{n\mathbf{k}}(\mathbf{r}) = u_{n\mathbf{k}}(\mathbf{r})e^{i\mathbf{k}\cdot\mathbf{r}} \quad (1.40)$$

which is basically the product of a plane wave $e^{i\mathbf{k}\cdot\mathbf{r}}$ and a periodic Bloch function $u_{n\mathbf{k}}(\mathbf{r})$, where n is an integer known as band index and \mathbf{k} is a pseudo-momentum, called crystal momentum. The tight binding model approximates that the atoms in a periodic lattice are well-separated that their orbitals do not overlap considerably. In this case, the localised atomic orbitals, $\{\phi_n(\mathbf{r})\}$ are a good representation of the electronic states. If $\hat{H}_a(\mathbf{R}) = \hat{p}^2/2m + V_a(\mathbf{r} - \mathbf{R})$ is the atomic Hamiltonian of an atom located at \mathbf{R} , then $\phi_n(\mathbf{r})$ satisfies the following equation,

$$\hat{H}_a(\mathbf{R}) \phi_n(\mathbf{r} - \mathbf{R}) = \epsilon_n \phi_n(\mathbf{r} - \mathbf{R}) \quad (1.41)$$

Then the single-particle Hamiltonian in Eq. 1.38 becomes,

$$\hat{H} = \hat{H}_a(\mathbf{R}_j) + \Delta V_{\mathbf{R}_j}(\mathbf{r}) \quad (1.42)$$

where a single atomic part at \mathbf{R}_j is singled out, with a correction given by

$$\Delta V_{\mathbf{R}_j}(\mathbf{r}) = \sum_{\mathbf{R}_{j'} \neq \mathbf{R}_j} V_a(\mathbf{r} - \mathbf{R}_{j'}) \quad (1.43)$$

There are different ways to construct the tight binding model. One such model is the Linear Combination of Atomic Orbitals (LCAO). An alternate way to approach the Tight-binding formalism is through Wannier functions. An important difference

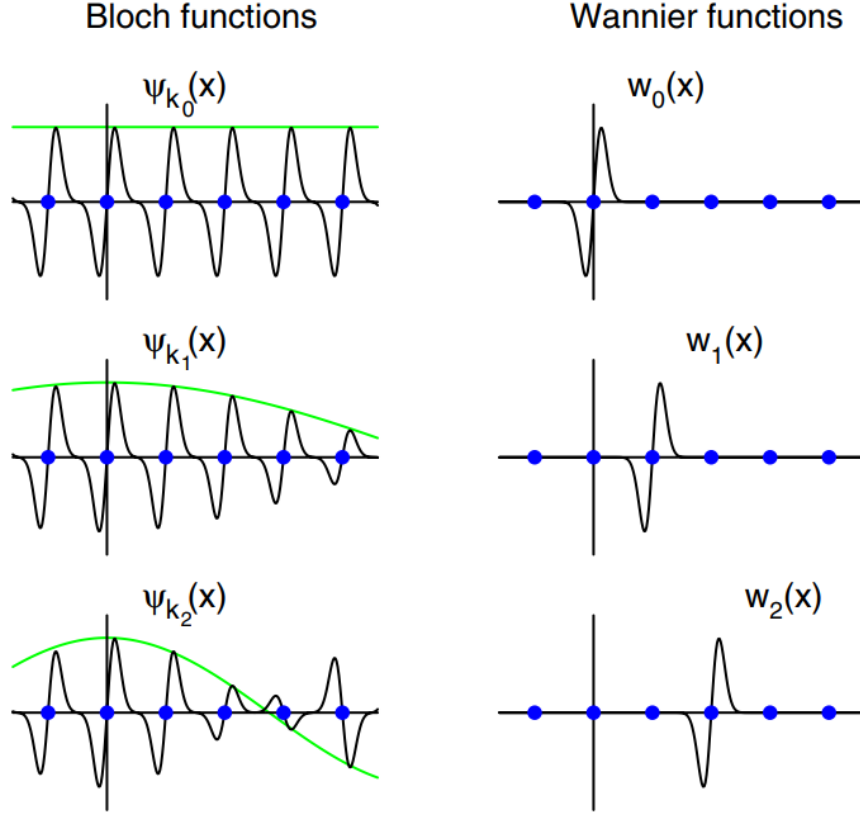


Figure 1.10: The left hand side shows the Bloch wave functions in real space, $e^{ikx}u_k(x)$, for three different k s, for a single band in one-dimensional system. The right hand side shows the corresponding wannier functions^[51]

between the two is that the Wannier functions satisfy the orthonormality criteria.

1.4.4 Maximally Localised Wannier Functions

Gregory Wannier, in the year 1967, introduced an alternate representation, in terms of the localised “Wannier functions” (WF) as opposed to the extended Bloch functions, to represent the electronic ground state of periodic systems. For a periodic system, in the independent particle approximation, the electronic ground state is described by a set of single particle orbitals and their corresponding occupations. For periodic systems, these orbitals are the Bloch wave functions, described by a crystal momentum, \mathbf{k} , residing in the Brillouin zone and n , the band index. The Wannier

functions are obtained by a unitary transformation of the Bloch functions, which localises the orbitals in the real space. Unlike the Bloch functions, the Wannier functions are not eigenvectors of the Hamiltonian.

The Bloch orbitals for a one-particle Hamiltonian is given as follows,

$$\Psi_{n\mathbf{k}}(\mathbf{r}) = u_{n\mathbf{k}}(\mathbf{r})e^{i\mathbf{k}\cdot\mathbf{r}} \quad (1.44)$$

where the periodicity in the Hamiltonian is contained in $u_{n\mathbf{k}}(\mathbf{r})$. For different crystal momenta, \mathbf{k} , the Bloch functions have different envelopes, $e^{i\mathbf{k}\cdot\mathbf{r}}$, see Fig. 1.10 and this allows us to construct the localized “wave-packet” by superposing Bloch functions of different envelopes. We can thus construct Wannier functions,

$$w_0(\mathbf{r}) = \frac{V}{2\pi} \int_{BZ} \Psi_{n\mathbf{k}}(\mathbf{r}) d\mathbf{k} \quad (1.45)$$

The integral is over the whole Brillouin zone and V is the volume of the primitive cell in real space. This gives the WF showed in Fig. 1.10. More generally, any translation in the real space can also be incorporated into the above transformation in the form of $e^{-i\mathbf{k}\cdot\mathbf{R}}$, where \mathbf{R} denotes the lattice vector in real space. Thus the above equation becomes,

$$|\mathbf{R}n\rangle = \frac{V}{2\pi} \int_{BZ} \Psi_{n\mathbf{k}}(\mathbf{r}) e^{-i\mathbf{k}\cdot\mathbf{R}} d\mathbf{k} \quad (1.46)$$

where, $|\mathbf{R}n\rangle$ is the WF of orbital n in the real space unit cell corresponding to \mathbf{R} . The set $\{|\mathbf{R}n\rangle\}$ is orthonormal and any WF, $|\mathbf{R}n\rangle$, can be transformed into another WF $|\mathbf{R}'n\rangle$ by a lattice translation vector, $\mathbf{R} - \mathbf{R}'$.

An important aspect to consider here is the fact that the above unitary transformation is not unique. This arises because of the nature of Bloch orbitals in that, there exists a “gauge freedom” in the definition of $\Psi_{n\mathbf{k}}(\mathbf{r})$. This means that there can be an arbitrary unitary operation that can be applied to the Bloch wavefunctions at each \mathbf{k} , which inevitably reflect in the non-uniqueness of the WFs as well. The

Bloch functions, however, must belong to a “smooth” gauge, to obtain well-localised WFs. This is in fact a general property of Fourier Transforms: the more smooth the reciprocal space function, the more localised the real-space function and vice-versa. To choose, from this set of Wannier functions, a unique set for any particular system, Marzari and Vanderbilt^[52] came up with the formulation of Maximally Localised Wannier Functions (MLWFs). Within this formalism, first, the spread functional,

$$\begin{aligned}\Omega &= \sum_n \langle \mathbf{0}n | \mathbf{r}^2 | \mathbf{0}n \rangle - \langle \mathbf{0}n | \mathbf{r} | \mathbf{0}n \rangle^2 \\ &= \sum_n [\langle r^2 \rangle_n - \bar{r}^2]\end{aligned}\tag{1.47}$$

which adds up the quadratic spread of the WFs in the home unit cell, $\mathbf{R} = \mathbf{0}$, is defined. This functional is then reformulated in terms of the Bloch functions in the k-space and then minimised with respect to the unitary transformation, U_{mn}^k , to obtain a highly localised set of Wannier functions for the system in hand.

1.4.5 Z_2 Invariant from Wannier Charge Centre

Fu and Kane^[53] defined the Z_2 invariants of a topological insulator in terms of a quantity called Time Reversal Polarisation (TRP), thereby providing a clear picture about the physical interpretation of the Z_2 invariant. Solunayov and Vanderbilt^[54] reformulated the TRP in terms of the Wannier Charge Centres, which are discussed above.

If we consider a one dimensional gapped Hamiltonian $H(x)$ which is subjected to an adiabatic pumping cycle, with t being the time or the pumping parameter with $H[t + T] = H[t]$, subject to the constraint,

$$H[-t] = \Theta H[t] \Theta^{-1}\tag{1.48}$$

then the constraint makes sure that the Hamiltonian, $H(x)$ is Time-reversal Invariant at $t = 0$ and $t = T/2$ and at any other value of t , the Time Reversal Symmetry (TRS) is broken. If we consider that the periodicity of the Hamiltonian is unity, *i.e.*, $H(x + 1) = H(x)$, then the eigenstates of the Hamiltonian are the periodic part of the Bloch states given by,

$$|u_{nk}\rangle = e^{-ikx} |\Psi_{nk}\rangle \quad (1.49)$$

These functions lie on a torus given the fact that the Hamiltonian is periodic in two parameters, k and t . At the time reversal invariant points, $t = 0$ and $t = T/2$, Kramer's theorem tells that there exists a pair of degenerate eigenstates at $k = 0$ and $k = \pi$. If we consider the Kramers pairs to fall into two different subspaces, then the Berry connection given by

$$A_k = \iota \sum_n \langle u_{nk} | \partial_k | u_{nk} \rangle \quad (1.50)$$

can be rewritten as,

$$A(k) = A^I(k) + A^{II}(k) \quad (1.51)$$

with

$$A^S(k) = \iota \sum_{\alpha} \langle u_{\alpha k}^S | \partial_k | u_{\alpha k}^S \rangle \quad (1.52)$$

where $S = I, II$ are the two subspaces, and α corresponds to the number of pairs in the occupied states. This allows to define the charge polarization also in a similar fashion, with the total polarisation,

$$P_{\rho} = \frac{1}{2\pi} \oint dk A_k \quad (1.53)$$

written as the sum of two “partial polarisation” defined as,

$$P_{\rho}^S = \frac{1}{2\pi} \oint dk A^S(k) \quad (1.54)$$

This partial polarisation is not gauge invariant and the total polarisation is defined only modulo an integer. The change in total polarisation during the adiabatic pumping cycle of the Hamiltonian is, however, gauge invariant. Thus,

$$P_\rho(T) - P_\rho(0) = C \quad (1.55)$$

with C denoting the Chern number, which corresponds to the number of charge quanta pumped through the system in a single adiabatic cycle. For a time reversal invariant system, this quantity is zero.

A similar quantity was introduced in^[53], called Time Reversal Polarization, which is non-zero for the TRS symmetric Hamiltonian. It is given as the difference of the two partial polarisations,

$$P_\Theta = P_\rho^I - P_\rho^{II} \quad (1.56)$$

Now, the Z_2 invariant is given by,

$$\Delta = P_\Theta(T/2) - P_\Theta(0) \text{ mod } 2 \quad (1.57)$$

It is to be noted that the Z_2 invariant as given above is well-defined only in the case of a gauge which is continuous on the torus defined by t and k and if it preserves time reversal symmetry at $t = 0$ and $t = T/2$. $\Delta = 1$ in the case of a non-trivial topological insulator and in this case, such a gauge can be defined only on a half torus.

Equation 1.57 can be reformulated in terms of the Wannier Charge Centre (WCC). The Wannier Charge Centre, \bar{x}_n or \bar{r}_n in the 3D case, is the expectation value of the position operator in a particular state $|\mathbf{0}n\rangle$ in the unit cell, as given below,

$$\bar{x}_n = \frac{\iota}{2\pi} \int_{-\pi}^{\pi} dk \langle u_{nk} | \partial_k | u_{nk} \rangle \quad (1.58)$$

The sum of all the WCCs in a unit cell is a gauge invariant quantity and the sum of WCCs over each subspace, $S = I, II$ is equal to the corresponding partial Berry connection $A^S(k)$ ^[54]. Thus the Z_2 invariant Δ can be written as,

$$\Delta = \sum_{\alpha} \left[\bar{x}_{\alpha}^I(T/2) - \bar{x}_{\alpha}^{II}(T/2) \right] - \sum_{\alpha} \left[\bar{x}_{\alpha}^I(0) - \bar{x}_{\alpha}^{II}(0) \right] \bmod 2 \quad (1.59)$$

This definition of the Z_2 invariant holds only if the gauge choice is Time Reversal(TR) invariant and is smooth in the half torus defined by k and t . The method for maximally localised Wannier functions, introduced in the previous subsection satisfies this criteria in 1D, provided the functions are made to evolve smoothly with t . However, enforcing this continuity with respect to t , for a multiple band system, on a discrete t -mesh may prove very challenging. In practice, Eq.1.59 can be implemented numerically, by simply plotting WCC at each t and by tracking their evolution with t or by just tracking the largest gap in the WCC spectrum. For defining the Z_2 invariant for a 3D Topological Insulator using this approach, we resort to Hybrid Wannier Charge Centres (HWCC)^[55], which are localised and wannier-like in one direction and Bloch-like in the other two.

1.5 Summary of the Thesis

The thesis is organised as follows, in the second chapter, the evolution of topological phases of TaSe₃ under hydrostatic pressure is studied in detail. TaSe₃ is a quasi one dimensional material, which has a superconducting transition temperature of the order of 2.3 K. The realization of materials with non-trivial topology and superconductivity is fascinating given the possibility of realising Majorana fermions in such systems. We study the topological nature of TaSe₃ from first principles and subsequently try to probe the behavior of the system with the application of hydrostatic pressure. Experimentally, from Raman Spectroscopy, it is observed that with the

increase in pressure, TaSe_3 undergoes two isostructural phase transitions, at 3 GPa and at 8 GPa. Our Density Functional Theory (DFT) analysis reveals that the two transitions observed are topological quantum phase transitions, the first one from a weak topological insulator phase to a strong topological phase and the second one at 8 GPa, from the strong topological phase to a weak topological phase. This fact is confirmed by the calculated Z_2 invariant as well as from the observation of a single Dirac cone on the TaSe_3 surface in the strong topological insulator phase.

There are two parts in chapter 3. The first part deals with the topological phases in $(\text{Sb}_2\text{Te}_3)_m(\text{Sb}_2)_n$ series, while in part B, the evolution of topological phases in Sb_2Te_3 and Sb_2Te under uniaxial strain and hydrostatic pressure has been studied. In the first part of chapter 3, the structure-property relationship in various materials in the $(\text{Sb}_2\text{Te}_3)_m(\text{Sb}_2)_n$ homologous series has been studied to understand the topological properties in this potentially good thermoelectric materials. The series has Sb_2Te_3 ($n=0$) and Sb_2 ($m=0$) at its extreme ends, out of which Sb_2Te_3 is known to be a topological insulator and Sb_2 , a topological semi metal. The series that we have studied include Sb_2Te_3 , Sb_2Te and SbTe , all of which reveal large phonon anharmonicity and low phonon group velocity, which indicates low lattice thermal conductivity. The existence of topological surface states in these promising thermoelectric materials will offer us new ways to control the thermopower, thereby making it even more lucrative. Our first principles studies reveal that, in addition to Sb_2Te_3 , Sb_2Te and SbTe also reveals a non-trivial topology with a non-zero strong invariant. Our simulated Angle Resolved Photoemission Spectroscopy (ARPES) reveals the presence of a single Dirac cone on the surfaces of all the three systems.

In the next part of chapter 3, the evolution of topological phases in Sb_2Te_3 and Sb_2Te under uniaxial strain and hydrostatic pressure is investigated. The electronic band structure of Sb_2Te_3 under the application of compressive strain (as large as 4%) along the c-axis, shows an increase in the band gap, with the retention of band inversion at the point, which indicates that the compressive strain does not lead to a

topological phase transition in Sb_2Te_3 . However, with the application of tensile strain (up to 4 %) , the band gap at Γ decreases. We also examined the band structure evolution in Sb_2Te_3 and Sb_2Te under hydrostatic pressure. In Sb_2Te_3 , we observe an increase in the valley degeneracy with pressure (upto 4 GPa) and a subsequent decrease in the valley degeneracy with further increase in pressure. Though no closing of the band gap is seen until 10 GPa, beyond 4 GPa, the band inversion at Γ ceases to exit, thereby making the material trivial at high pressures. The high pressure studies on Sb_2Te , reveal a strong to weak topological phase transition beyond 6 GPa. This is confirmed by the band gap closing and reopening at the L -point.

In chapter 4, we have studied the dynamic magnetic ground state in a dimer based compound $\text{Yb}_2\text{Te}_5\text{O}_{13}$. The Yb^{3+} ions in $\text{Yb}_2\text{Te}_5\text{O}_{13}$ are in a $J_{eff} = 1/2$ state because of the large Spin-Orbit Coupling (SOC) and the Crystal Electric Field (CEF) splitting, making it very susceptible to quantum fluctuations. The Yb atoms form a dimer along the c -axis, with the dimers stacked along the a -axis. Experimental magnetic susceptibility and specific heat do not show magnetic ordering at temperatures as low as 400 mK. Moreover, the μSR studies also hint at the absence of local static magnetic field in the system. In this chapter, we discuss the microscopic origin of this dynamic magnetic state using first principles. We calculated the nearest (J_1), next nearest (J_2) and the third nearest (J_3) neighbor exchange interactions as well as the zero-field splitting parameters D and E from first principles. We observe that J_1 and J_2 are antiferromagnetic and J_3 is ferromagnetic. J_1 is the exchange between Yb atoms in the dimer, along the c -axis, while J_2 and J_3 act in the a - b plane and are of opposing character. This competition between the exchanges in the a - b plane leads to the dynamic magnetic ground state seen in the experimental system between temperature 125 K down to 45 K. Owing to the fact that the single ion anisotropy and the biaxial anisotropy, D and E respectively, are much lower as compared to J_1 , we constructed an effective J_1 - J_2 - J_3 Heisenberg model to simulate the system. Our Monte Carlo studies reveal diffused peaks in the equal time structure factor at 50 K,

hinting at a spiral spin liquid regime in the 45K to 125 K temperature range.

In chapter 5 we explore the dynamic magnetic ground state in a hyper honeycomb lattice, with an inherent disorder between the Sodium (Na) and Ytterbium (Yb) sites. Owing to this disorder, we obtained six possible structures, out of which we studied the energetically lowest structure and a structure with geometric frustration. The former shows very low values of J_1 and J_2 ($\sim 10^{-2}$ meV), while the latter shows exchange interactions of the order of 10^{-1} meV. The disorder in the system thus leads to the lowering of the exchange couplings, leading to a huge suppression of the magnetic ordering temperature. We analyzed the equal time structure factor for both the systems, which revealed broad, diffused peaks (around the ground state peaks observed from iterative minimisation), thus confirming a dynamic magnetic ground state in the system.

The last chapter is the conclusion and future outlook, where we have summarized all the major and salient points obtained in each of the four work chapters, with a discussion on the topics to be studied in the near future.

Bibliography

- [1] H. L. Stormer, D. C. Tsui, and A. C. Gossard, “The fractional quantum hall effect,” *Rev. Mod. Phys.*, vol. 71, pp. S298–S305, Mar 1999.
- [2] X.-G. Wen, “Topological orders and edge excitations in fractional quantum hall states,” *Advances in Physics*, vol. 44, no. 5, pp. 405–473, 1995.
- [3] X.-G. Wen, “Topological order: From long-range entangled quantum matter to a unified origin of light and electrons,” *International Scholarly Research Notices*, vol. 2013, no. 1, p. 198710, 2013.
- [4] A. Kitaev and J. Preskill, “Topological entanglement entropy,” *Phys. Rev. Lett.*, vol. 96, p. 110404, Mar 2006.

-
- [5] M. Levin and X.-G. Wen, “Detecting topological order in a ground state wave function,” *Phys. Rev. Lett.*, vol. 96, p. 110405, Mar 2006.
 - [6] M. Z. Hasan and C. L. Kane, “Colloquium: Topological insulators,” *Rev. Mod. Phys.*, vol. 82, pp. 3045–3067, Nov 2010.
 - [7] M. Nakahara, *GEOMETRY, TOPOLOGY AND PHYSICS*. Institute of Physics, 1990.
 - [8] L. Fu and C. L. Kane, “Topological insulators with inversion symmetry,” *Phys. Rev. B*, vol. 76, p. 045302, Jul 2007.
 - [9] F. D. M. Haldane, “Model for a quantum hall effect without landau levels: Condensed-matter realization of the ”parity anomaly”,” *Phys. Rev. Lett.*, vol. 61, pp. 2015–2018, Oct 1988.
 - [10] R. B. Laughlin, “Quantized hall conductivity in two dimensions,” *Phys. Rev. B*, vol. 23, pp. 5632–5633, May 1981.
 - [11] L. Fu, C. L. Kane, and E. J. Mele, “Topological insulators in three dimensions,” *Phys. Rev. Lett.*, vol. 98, p. 106803, Mar 2007.
 - [12] Y. Ran, Y. Zhang, and A. Vishwanath, “One-dimensional topologically protected modes in topological insulators with lattice dislocations,” *Nature Physics*, vol. 5, pp. 298–303, Apr 2009.
 - [13] P. A. Lee and T. V. Ramakrishnan, “Disordered electronic systems,” *Rev. Mod. Phys.*, vol. 57, pp. 287–337, Apr 1985.
 - [14] H. Suzuura and T. Ando, “Crossover from symplectic to orthogonal class in a two-dimensional honeycomb lattice,” *Phys. Rev. Lett.*, vol. 89, p. 266603, Dec 2002.

-
- [15] Q. L. He, T. L. Hughes, N. P. Armitage, Y. Tokura, and K. L. Wang, “Topological spintronics and magnetoelectronics,” *Nature Materials*, vol. 21, pp. 15–23, Jan 2022.
- [16] H. Peng, W. Dang, J. Cao, Y. Chen, D. Wu, W. Zheng, H. Li, Z.-X. Shen, and Z. Liu, “Topological insulator nanostructures for near-infrared transparent flexible electrodes,” *Nature Chemistry*, vol. 4, pp. 281–286, Apr 2012.
- [17] P. Di Pietro, M. Ortolani, O. Limaj, A. Di Gaspare, V. Giliberti, F. Giorgianni, M. Brahlek, N. Bansal, N. Koirala, S. Oh, P. Calvani, and S. Lupi, “Observation of dirac plasmons in a topological insulator,” *Nature Nanotechnology*, vol. 8, pp. 556–560, Aug 2013.
- [18] Z. Yue, B. Cai, L. Wang, X. Wang, and M. Gu, “Intrinsically core-shell plasmonic dielectric nanostructures with ultrahigh refractive index,” *Science Advances*, vol. 2, no. 3, p. e1501536, 2016.
- [19] L. Balents, “Spin liquids in frustrated magnets,” *Nature*, vol. 464, pp. 199–208, Mar 2010.
- [20] P. Anderson, “Resonating valence bonds: A new kind of insulator?,” *Materials Research Bulletin*, vol. 8, no. 2, pp. 153–160, 1973.
- [21] G. H. Wannier, “Antiferromagnetism. the triangular ising net,” *Phys. Rev.*, vol. 79, pp. 357–364, Jul 1950.
- [22] X. G. Wen, “Effective lagrangian for holes in the spin-liquid state,” *Phys. Rev. B*, vol. 39, pp. 7223–7227, Apr 1989.
- [23] X. G. Wen, “Mean-field theory of spin-liquid states with finite energy gap and topological orders,” *Phys. Rev. B*, vol. 44, pp. 2664–2672, Aug 1991.

- [24] T. Isono, T. Terashima, K. Miyagawa, K. Kanoda, and S. Uji, “Quantum criticality in an organic spin-liquid insulator κ -(bedt-ttf) $_2$ cu $_2$ (cn) $_3$,” *Nature Communications*, vol. 7, p. 13494, Nov 2016.
- [25] M. R. Norman, “Colloquium: Herbertsmithite and the search for the quantum spin liquid,” *Rev. Mod. Phys.*, vol. 88, p. 041002, Dec 2016.
- [26] Z. Dai, J.-X. Yu, B. Zhou, S. A. Tenney, P. Lampen-Kelley, J. Yan, D. Mandrus, E. A. Henriksen, J. Zang, K. Pohl, and J. T. Sadowski, “Crystal structure reconstruction in the surface monolayer of the quantum spin liquid candidate α -rucl $_3$,” *2D Materials*, vol. 7, p. 035004, apr 2020.
- [27] J. C. Leiner, H. O. Jeschke, R. Valentí, S. Zhang, A. T. Savici, J. Y. Y. Lin, M. B. Stone, M. D. Lumsden, J. Hong, O. Delaire, W. Bao, and C. L. Broholm, “Frustrated magnetism in mott insulating $(v_{1-x}cr_x)_2O_3$,” *Phys. Rev. X*, vol. 9, p. 011035, Feb 2019.
- [28] S. Yamashita, Y. Nakazawa, M. Oguni, Y. Oshima, H. Nojiri, Y. Shimizu, K. Miyagawa, and K. Kanoda, “Thermodynamic properties of a spin-1/2 spin-liquid state in a κ -type organic salt,” *Nature Physics*, vol. 4, pp. 459–462, Jun 2008.
- [29] A. Banerjee, J. Yan, J. Knolle, C. A. Bridges, M. B. Stone, M. D. Lumsden, D. G. Mandrus, D. A. Tennant, R. Moessner, and S. E. Nagler, “Neutron scattering in the proximate quantum spin liquid κ -rucl $_3$,” *Science*, vol. 356, no. 6342, pp. 1055–1059, 2017.
- [30] Y. Kasahara, T. Ohnishi, Y. Mizukami, O. Tanaka, S. Ma, K. Sugii, N. Kurita, H. Tanaka, J. Nasu, Y. Motome, T. Shibauchi, and Y. Matsuda, “Majorana quantization and half-integer thermal quantum hall effect in a kitaev spin liquid,” *Nature*, vol. 559, pp. 227–231, Jul 2018.

- [31] J. A. Paddison, M. Daum, Z. Dun, G. Ehlers, Y. Liu, M. Stone, H. Zhou, and M. Mourigal, “Continuous excitations of the triangular-lattice quantum spin liquid YbMgGaO_4 ,” *Nature Physics*, vol. 13, pp. 117–122, Feb 2017.
- [32] Y. Shen, Y.-D. Li, H. Wo, Y. Li, S. Shen, B. Pan, Q. Wang, H. C. Walker, P. Steffens, M. Boehm, Y. Hao, D. L. Quintero-Castro, L. W. Harriger, M. D. Frontzek, L. Hao, S. Meng, Q. Zhang, G. Chen, and J. Zhao, “Evidence for a spinon fermi surface in a triangular-lattice quantum-spin-liquid candidate,” *Nature*, vol. 540, pp. 559–562, Dec 2016.
- [33] Z. Zhu, P. A. Maksimov, S. R. White, and A. L. Chernyshev, “Disorder-induced mimicry of a spin liquid in YbMgGaO_4 ,” *Phys. Rev. Lett.*, vol. 119, p. 157201, Oct 2017.
- [34] B. Gao, T. Chen, D. W. Tam, C.-L. Huang, K. Sasmal, D. T. Adroja, F. Ye, H. Cao, G. Sala, M. B. Stone, C. Baines, J. A. T. Verezhak, H. Hu, J.-H. Chung, X. Xu, S.-W. Cheong, M. Nallaiyan, S. Spagna, M. B. Maple, A. H. Nevidomskyy, E. Morosan, G. Chen, and P. Dai, “Experimental signatures of a three-dimensional quantum spin liquid in effective spin-1/2 $\text{Ce}_2\text{Zr}_2\text{O}_7$ pyrochlore,” *Nature Physics*, vol. 15, pp. 1052–1057, Oct 2019.
- [35] E. M. Smith, O. Benton, D. R. Yahne, B. Placke, R. Schäfer, J. Gaudet, J. Dudenmaier, A. Fitterman, J. Beare, A. R. Wildes, S. Bhattacharya, T. DeLazzer, C. R. C. Buhariwalla, N. P. Butch, R. Movshovich, J. D. Garrett, C. A. Majerison, J. P. Clancy, E. Kermarrec, G. M. Luke, A. D. Bianchi, K. A. Ross, and B. D. Gaulin, “Case for a $u(1)_\pi$ quantum spin liquid ground state in the dipole-octupole pyrochlore $\text{Ce}_2\text{Zr}_2\text{O}_7$,” *Phys. Rev. X*, vol. 12, p. 021015, Apr 2022.
- [36] R. Sibille, N. Gauthier, E. Lhotel, V. Porée, V. Pomjakushin, R. A. Ewings, T. G. Perring, J. Ollivier, A. Wildes, C. Ritter, T. C. Hansen, D. A. Keen, G. J. Nilsen, L. Keller, S. Petit, and T. Fennell, “A quantum liquid of magnetic

- octupoles on the pyrochlore lattice,” *Nature Physics*, vol. 16, pp. 546–552, May 2020.
- [37] A. Kitaev, “Fault-tolerant quantum computation by anyons,” *Annals of Physics*, vol. 303, no. 1, pp. 2–30, 2003.
- [38] C. Nayak, S. H. Simon, A. Stern, M. Freedman, and S. Das Sarma, “Non-abelian anyons and topological quantum computation,” *Rev. Mod. Phys.*, vol. 80, pp. 1083–1159, Sep 2008.
- [39] P. Hohenberg and W. Kohn, “Inhomogeneous electron gas,” *Phys. Rev.*, vol. 136, pp. B864–B871, Nov 1964.
- [40] W. Kohn and L. J. Sham, “Self-consistent equations including exchange and correlation effects,” *Phys. Rev.*, vol. 140, pp. A1133–A1138, Nov 1965.
- [41] D. M. Ceperley and B. J. Alder, “Ground state of the electron gas by a stochastic method,” *Phys. Rev. Lett.*, vol. 45, pp. 566–569, Aug 1980.
- [42] J. P. Perdew and A. Zunger, “Self-interaction correction to density-functional approximations for many-electron systems,” *Phys. Rev. B*, vol. 23, pp. 5048–5079, May 1981.
- [43] J. P. Perdew, “Density-functional approximation for the correlation energy of the inhomogeneous electron gas,” *Phys. Rev. B*, vol. 33, pp. 8822–8824, Jun 1986.
- [44] A. D. Becke, “Density-functional exchange-energy approximation with correct asymptotic behavior,” *Phys. Rev. A*, vol. 38, pp. 3098–3100, Sep 1988.
- [45] J. P. Perdew and Y. Wang, “Accurate and simple analytic representation of the electron-gas correlation energy,” *Phys. Rev. B*, vol. 45, pp. 13244–13249, Jun 1992.

-
- [46] J. P. Perdew, K. Burke, and M. Ernzerhof, “Generalized gradient approximation made simple,” *Phys. Rev. Lett.*, vol. 77, pp. 3865–3868, Oct 1996.
 - [47] C. Lee, W. Yang, and R. G. Parr, “Development of the colle-salvetti correlation-energy formula into a functional of the electron density,” *Phys. Rev. B*, vol. 37, pp. 785–789, Jan 1988.
 - [48] Y. Liang, J. Wang, and H. Peng, “Quasi-one-dimensional tase3: A new topological superconductor candidate,” *Matter*, vol. 4, no. 1, pp. 19–21, 2021.
 - [49] H. Zhang, C.-X. Liu, X.-L. Qi, X. Dai, Z. Fang, and S.-C. Zhang, “Topological insulators in bi_2se_3 , bi_2te_3 and sb_2te_3 with a single dirac cone on the surface,” *Nature Physics*, vol. 5, pp. 438–442, Jun 2009.
 - [50] D. Hsieh, Y. Xia, D. Qian, L. Wray, F. Meier, J. H. Dil, J. Osterwalder, L. Patthey, A. V. Fedorov, H. Lin, A. Bansil, D. Grauer, Y. S. Hor, R. J. Cava, and M. Z. Hasan, “Observation of time-reversal-protected single-dirac-cone topological-insulator states in bi_2te_3 and sb_2te_3 ,” *Phys. Rev. Lett.*, vol. 103, p. 146401, Sep 2009.
 - [51] N. Marzari, A. A. Mostofi, J. R. Yates, I. Souza, and D. Vanderbilt, “Maximally localized wannier functions: Theory and applications,” *Rev. Mod. Phys.*, vol. 84, pp. 1419–1475, Oct 2012.
 - [52] N. Marzari and D. Vanderbilt, “Maximally localized generalized wannier functions for composite energy bands,” *Phys. Rev. B*, vol. 56, pp. 12847–12865, Nov 1997.
 - [53] L. Fu and C. L. Kane, “Time reversal polarization and a Z_2 adiabatic spin pump,” *Phys. Rev. B*, vol. 74, p. 195312, Nov 2006.
 - [54] A. A. Soluyanov and D. Vanderbilt, “Computing topological invariants without inversion symmetry,” *Phys. Rev. B*, vol. 83, p. 235401, Jun 2011.

-
- [55] A. A. Soluyanov and D. Vanderbilt, “Wannier representation of F_2 topological insulators,” *Phys. Rev. B*, vol. 83, p. 035108, Jan 2011.

Evolution of Topological Phases of TaSe₃ under Hydrostatic Pressure

2.1 Introduction

The recent years have seen tremendous impetus in finding interesting and novel topological materials, since the observation of quantum Hall effect^[1] and subsequent realisations of a plethora of similar systems, like topological insulators, semimetals, topological superconductors. . . to name a few^[2-4]. Identification of such novel phases and distinguishing them from one another is an extensively researched area in the material science community. The origin of the topological features is the non-trivial *twist* of electronic bands in a material. Among the host of various topological band insulators, the topological superconductivity is much coveted, because of its uniqueness.

** Work reported in this chapter is submitted for publication : Janaky Sunil*, Anita Gemmy Francis*, Anjana Joseph, Anustoop Das, Bobby Joseph, K.A. Irshad, Kanishka Biswas, Swapan K Pati, Chandrabhas Narayana.

* The authors have contributed equally

In fact, in the spectrum of different topological phases, topological superconductivity is distinguished, as it can host Majorana states with non-Abelian statistics, which are quite distinct from Fermions or Bosons [5]. The emergence of Majorana Fermions and the possibility of their braiding [6] in such systems, offer huge prospects for applications in the field of quantum computation and quantum cryptography[7].

Topological superconductors are, however, not very common. Most of the superconductors are topologically non-trivial. A viable way to realise such topological superconductivity is to form a heterostructure of a topological insulator and superconductor, where the proximity effect leads to the realisation of Majorana states[8,9]. Although signatures of Majorana states exist in these heterostructures, the Majorana fermions are not yet observed experimentally. Identifying and proposing new candidates for potential intrinsic topological superconductivity is thus an important and evolving field of research currently [10,11]. In this respect, the TaSe₃ is very intriguing. This layered transition metal trichalcogenide, is found to have a superconducting transition at a temperature of ~ 2.3 K [12]. Moreover, recent studies on TaSe₃ reveal that they have non-trivial topology as well [13–15], making it a promising candidate for the exploration of topological superconductivity.

Over the last few years, numerous theoretical and experimental investigations were conducted to comprehend the electronic structure and Fermi surface of TaSe₃, to understand its topological properties. For example, using first-principles calculations, Nie et.al. proposed that, at ambient conditions, the electronic band structure of TaSe₃ has a nontrivial character [13]. Z_2 invariants ($\nu_0; \nu_1, \nu_2, \nu_3$) were estimated to be (1;100). This indicates a strong topological phase and the presence of Dirac cones on all the surfaces. This was further supported by the direct observation of topological surface states in TaSe₃ experimentally, via the angle resolved photo emission spectroscopy (ARPES) [16]. However, there have been conflicting reports in the literature as well. A recent publication has shown that at 0 GPa, TaSe₃ is a weak topological insulator (WTI), with the Z_2 invariants given as (0;101) [17]. All the stud-

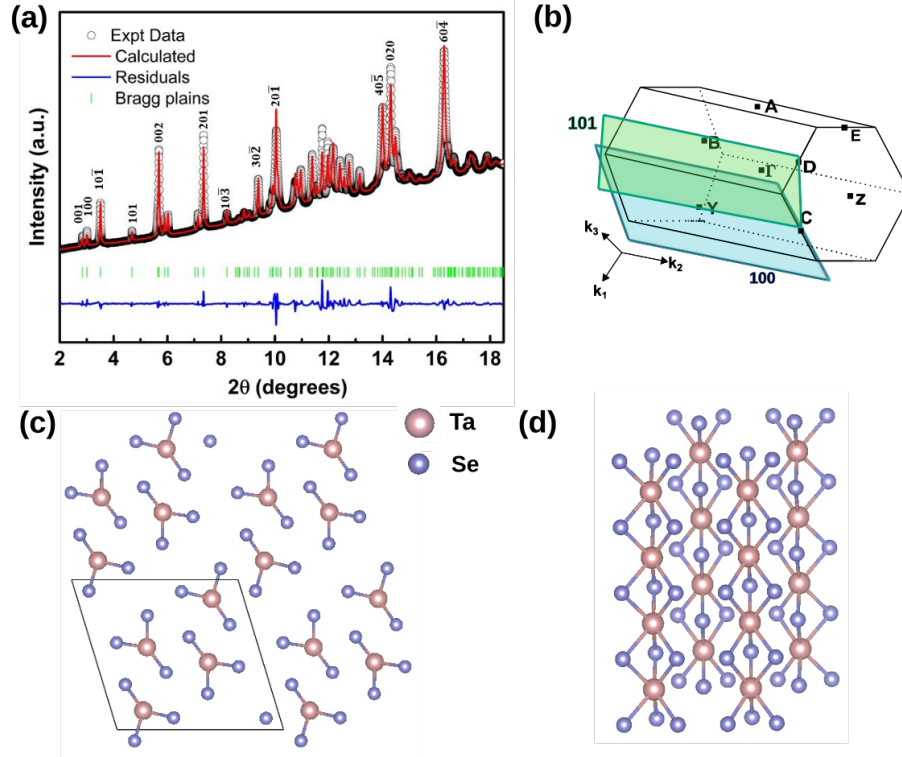


Figure 2.1: (a) Le Bail fit of the XRD pattern of TaSe₃ at ambient conditions. (b) The first Brillouin zone of TaSe₃, with the 101 and 100 planes shown as coloured rectangles. The 8 TRIM points are also denoted within the BZ. The top (c) and the side (d) views of the TaSe₃ structure. The chain like arrangement of the trigonal prisms is clear in (d) and we see four such chains in the unit cell (c).

ies point to a non-trivial topological nature of TaSe₃ at ambient conditions. However, there is a lack of consensus about the nature of the non-trivial phase of TaSe₃.

The Hamiltonian of such a system can be tuned in various ways, including elemental substitution, applying strain or pressure, changing the temperature etc., to induce a topological quantum phase transition from one topological phase to another. The chain-like structure of TaSe₃ has pushed several research groups to study the strain effect on this material. Such a study by Nie et al.^[13] has revealed that a uniaxial tensile strain along the c -axis causes a TQPT in TaSe₃, from strong topological insulator (STI) to a weak topological insulator (WTI), with a Dirac semi-metal phase between the two insulating phases. Unlike the case of strain along the c direction, under a tensile strain along b , TaSe₃ was shown to undergo a transition from a STI

to a trivial insulator^[18]. Remarkably, a similar TQPT- from WTI (seen at ambient conditions) to STI- is reported by Hyun et al., with clear signatures of topological surface states on the $(10\bar{1})$ plane^[17]. A major part of the phase diagram of TaSe₃ is still unexplored, because most of the studies deal with uniaxial or biaxial strain. Moreover, the ambiguity in the nature of TaSe₃ at ambient conditions prevails in the existing literature. In this chapter, we investigate the topological nature of TaSe₃ under hydrostatic compression from first principles and Raman spectroscopy. High-pressure Raman studies show two phase transitions in the sample with the application of pressure. The DFT calculations reveal that TaSe₃ is a weak topological insulator at 0 GPa. The analysis of the evolution of the band structure and the calculated Z_2 invariants, show that the two transitions occurring in the system are topological quantum phase transitions. The first transition is from a weak topological phase to a strong one, while the second transition is from a strong phase to a weak phase. The simulated ARPES spectrum reveals a single Dirac cone on a surface in the strong TI phase, while the two weak TI phases flanking this STI phase, show no Dirac cones, but a Rashba-like splitting of the surface states.

2.2 Computational Methods

The density functional theory (DFT) calculations are performed using the Quantum Espresso^{[19] [20] [21]} suite. We used the Generalized Gradient Approximation(GGA) by Perdew-Burke-Ernzerhof(PBE)^[22] for the exchange-correlation functional. The Optimized Norm-Conserving Vanderbilt Pseudopotentials (ONCVP)^[23] with full relativistic correction were employed for Tantalum and Selenium for all the simulations. The wave function was expanded in a plane wave basis, which was truncated at an 80 Ry energy cut-off. To avoid the slower convergence which may arise from the discontinuity of energy bands around the Fermi level, which may be partially filled, a Methfessel-Paxton function with a $k_B T = 0.01$ Ry energy spread was used to smear

the contribution from all the k-points. The sampling of Brillouin Zone (BZ) was done with a $7 \times 19 \times 6$ k-point grid. The energy cut-off for plane waves and the k-point grid were chosen by performing an energy convergence calculation. First, for a given k-point grid, the ground state energy was calculated by varying the plane wave cut-off energy. The minimal energy cut-off beyond which the ground state energy converges was chosen for the subsequent calculations. Once the energy cut-off was fixed, the same procedure was done for a number of k-point grids, and a suitable number of k-points were chosen depending on the convergence of ground state energy. Grimme's DFT-D3^[24,25] semi-empirical correction is also included in the calculations to accurately describe the van der Waals's interaction present in the system. For the ambient conditions' calculations, the effect of Spin-Orbit Coupling (SOC) to the band structure was examined by performing the calculations with and without the inclusion of SOC. For all the other pressures, between 1 GPa and 12 GPa, the calculations were performed with the inclusion of SOC. At each pressure, the corresponding lattice constants were obtained from the ambient conditions structure, by minimising the enthalpy $H = E + PV$ at each pressure. Parity analysis method for materials with inversion symmetry, as given by Fu-Kane^[26] was used to calculate the Z_2 invariants. The parity eigenvalues for the bands were obtained by comparing their irreducible representations against the standard character table, using the Irrep software^[27]. The Z_2 invariants were analysed using Wannier Charge Centres (WCCs) as well. The Z_2 invariant in this method is calculated by tracking the evolution of Wannier Charge Centres as the crystal momenta change from 0 to π . This was implemented using the WannierTools software^[28]. We also have calculated the surface spectrum at various pressures to simulate the ARPES of a number of planes. This was also implemented using WannierTools^[28], using the iterative Green's Function method. The tight binding parameters for the system were obtained from the Maximally Localised Wannier functions (MLWF), which were calculated using Wannier90^[29].

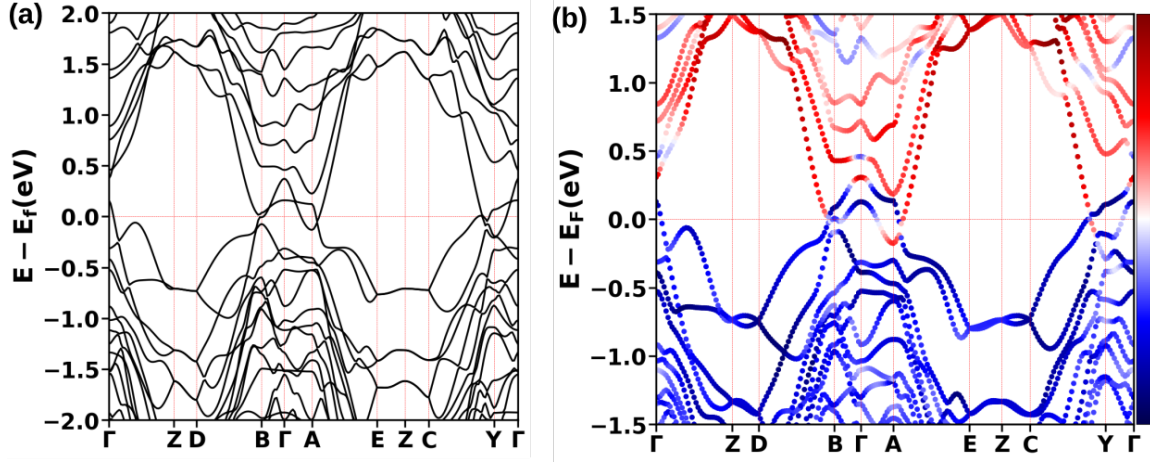


Figure 2.2: (a) The band structure of TaSe₃ at 0 GPa without the inclusion of SOC. (b) The orbital projected band structure at 0 GPa. Without SOC, TaSe₃ shows no band gap. As SOC is included the bands near $B - \Gamma - A$, separate giving a finite band gap. In (b), the red bands correspond to the Ta d orbitals and the blue colour represents the Se p orbitals. At B , A and Y , there are clear signatures of band inversion.

2.3 Results

Topological Nature of TaSe₃ at 0 GPa

Layered transition metal trichalcogenides crystallize in a well known structure^[30], characterized by stacked chains of MX₆ trigonal prisms, making them quasi-one dimensional (1D) in nature. The structural characterization using XRD revealed that TaSe₃ has a layered P21/m monoclinic structure with the lattice parameters $a = 9.8265$ Å, $b = 3.4983$ Å and $c = 10.41$ Å. Each unit cell of TaSe₃ has four chain-like structures oriented along the b -axis. After geometry optimisation, the lattice parameters at 0 GPa was observed to be $a = 9.92$ Å, $b = 3.50$ Å and $c = 10.55$ Å. The observed values are well within expected DFT error as compared to the XRD values. The optimised structure of the TaSe₃ sample is illustrated in Fig. 2.1(c) and (d), and Fig. 2.1(b) depicts the corresponding Brillouin Zone (BZ) with all the 8 high symmetry points.

The band structure was first calculated without including spin-orbit coupling. The band structure reveals no gap along the $B - \Gamma - A$ path in the Brillouin Zone. However,

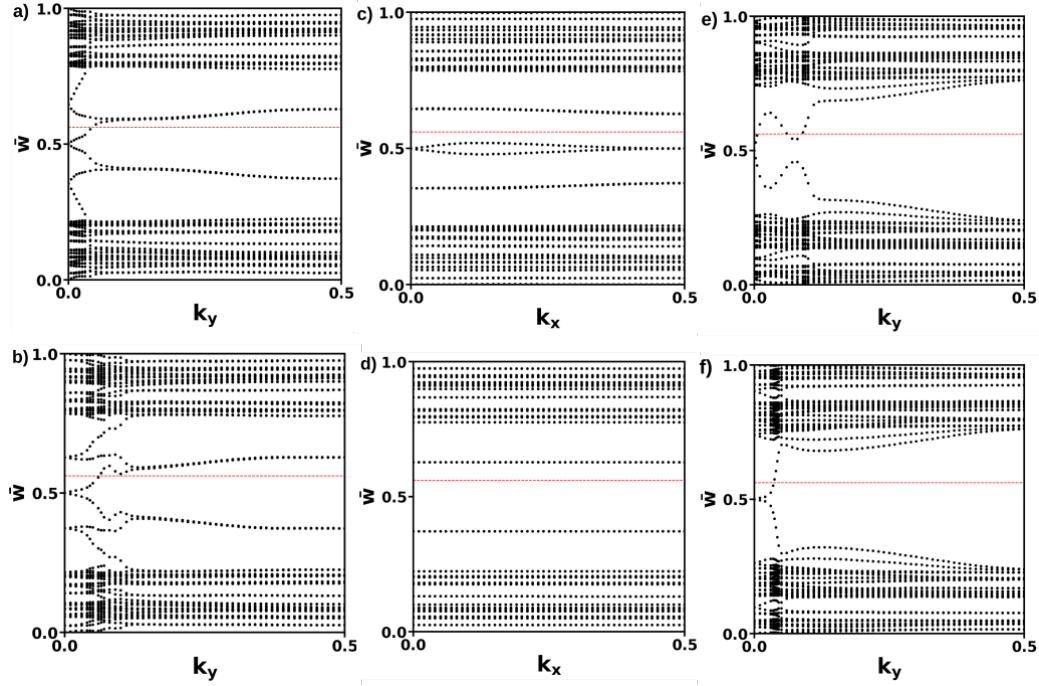


Figure 2.3: Wannier Charge Centre evolution for the six time reversal invariant planes (a) $k_x = 0$ (b) $k_x = \frac{\pi}{a}$ (c) $k_y = 0$ (d) for $k_y = \frac{\pi}{b}$ (e) $k_z = 0$ (f) $k_z = \frac{\pi}{c}$ at 0GPa. A line is chosen at random at $\bar{W} = 0.55$, and is denoted by the red dotted line. If the number of times this line cuts any chosen WCC evolution line is even, then, Δ is 0, otherwise it's 1. In a), the line cuts the wcc evolution at one point, making it's Chern number 1. Similarly, for the other planes we get b) $\Delta = 1$ c) $\Delta = 0$ d) $\Delta = 0$ e) $\Delta = 1$ (3 mod 2) f) $\Delta = 1$.

as we include the SOC, a continuous band gap opens up throughout the Brillouin zone. This is shown in Fig. 2.2, where the projections of the p-orbitals of Se and d-orbitals of Ta are plotted on the bands. The valence and conduction bands which were overlapping near the Fermi-level in the absence of SOC, get separated with the SOC added. However, the maxima of the valence band lies above the Fermi level, with a small density of states (DOS), which leads to the observed semi-metallic properties in TaSe₃^[13]. Nonetheless, since a finite gap exists, the definition of Z_2 invariants is possible here. The fat bands reported in Fig. 2.2, reveal a conduction band that is mostly derived from Ta d-orbitals, while the valence band is predominantly formed by the Se p orbitals. The orbital character along the $B - \Gamma$, $A - E$ and $Y - C$ shows a reversal in this trend. This disruption of general trend of orbital character is called band inversion and is a necessary condition for topological non-trivial nature

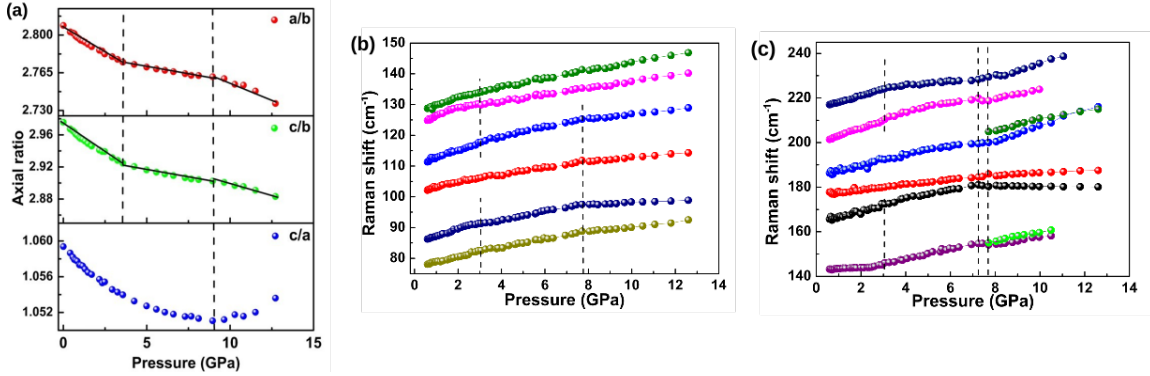


Figure 2.4: (a) The ratio of lattice constants with pressure. The ratio shows a slope change at around 3 GPa and 8 GPa. b) and c) shows the Raman shift with pressure. At 3 GPa and 8 GPa, most of modes undergo a softening as opposed to the expected hardening.

of the bands. Thus, at ambient condition the material shows non-trivial topological properties. Three TRIM points show an orbital-reversal and the presence of odd number of band inversions signals to a strong topological insulator. But, a parity analysis of the valence and conduction bands show that at TRIM point A , both conduction and valence bands have the same parity eigenvalues, which means that they will avoid crossing each other. This in turn means that the band inversion at A is trivial. At B and Y , the parity of the conduction and valence bands are opposite to each other, thereby making it possible for them to cross. Thus, only two of the three points can be considered to have band inversion, thereby indicating that, at 0 GPa the material is a weak topological insulator (WTI). Conclusive determination of the topological character of a sample demands the calculation of the Z_2 invariants. For a three-dimensional system, there exists four Z_2 invariants that are used to classify the various topological phases - $(\nu_0, \nu_1, \nu_2, \nu_3)$. A strong topological insulator (STI), which hosts robust topological surface states (TSS) on all of its surfaces, has $\nu_0 = 1$. If $\nu_0 = 0$, then it is a WTI. Thus, ν_0 is called the strong invariant. (ν_1, ν_2, ν_3) are labelled as the weak topological indices. This is the direction of stacking of 2D topological insulators and represents the direction perpendicular to the surface which does not host TSS. All the other surfaces host an even number of Dirac cones, which can be removed in pairs^[31].

TaSe₃ has an inversion-centre and this simplifies the calculation of Z_2 invariants a great deal, using the Fu-Kane parity analysis^[26]. In this formalism, a quantity denoted as δ_i is calculated, which is the product of the parity-eigenvalues of all the occupied bands at a given TRIM point denoted as Γ_i . Only one of the Kramer's partner's parity is included in the product. ν_0 , the strong index is obtained from $(-1)^{\nu_0} = \prod_{m=1}^8 \delta_m$, while the weak indices are obtained as the product of four δ_i s calculated at four Γ_i s lying on a single plane. Three such planes are considered to get the three weak indices. The 8 TRIM points in the Brillouin zone of TaSe₃ gives the following set of equations,

$$\begin{aligned}
 (-1)^{\nu_0} &= \delta(Z)\delta(D)\delta(B)\delta(\Gamma)\delta(A)\delta(E)\delta(C)\delta(Y) \\
 (-1)^{\nu_1} &= \delta(A)\delta(E)\delta(C)\delta(Y) \\
 (-1)^{\nu_2} &= \delta(Z)\delta(D)\delta(C)\delta(E) \\
 (-1)^{\nu_3} &= \delta(D)\delta(B)\delta(A)\delta(E)
 \end{aligned} \tag{2.1}$$

At 0 GPa, $\delta(Z) = \delta(D) = \delta(\Gamma) = \delta(A) = \delta(E) = \delta(C) = -1$ and $\delta(B) = \delta(Y) = +1$. It is clear that in this case the strong index becomes 0, thereby confirming weak topological nature of TaSe₃ at 0 GPa. The weak indices are calculated to be (101). This represents the Miller indices corresponding to the surface without the TSSs. This calculation of Z_2 invariants from the parity analysis is further corroborated by analysing how the Hybrid Wannier Charge Centres(HWCCs) evolve on a cylinder. HWCCs is a convenient way of obtaining 1D localised Wannier functions in 3D. They can be imagined as the Wannier charge centres of a system localised only in one dimension. Let us assume this direction to be x . Then the other two dimensions can be thought of as external parameters to which the Hamiltonian is coupled. These two parameters, k_y and k_z then form the two fluxes threading the Corbino torus^[32]. At each k_y , the hybrid WCC $\bar{x}(k_y)$ is a point defined on a circle of radius unity. As the flux k_y changes smoothly from 0 to 2π , the HWCCs flow on a cylinder $S^1 \times [0, 2\pi]$. This is like the charge pump of Laughlin. For a 2D slice of a 3D BZ, the number

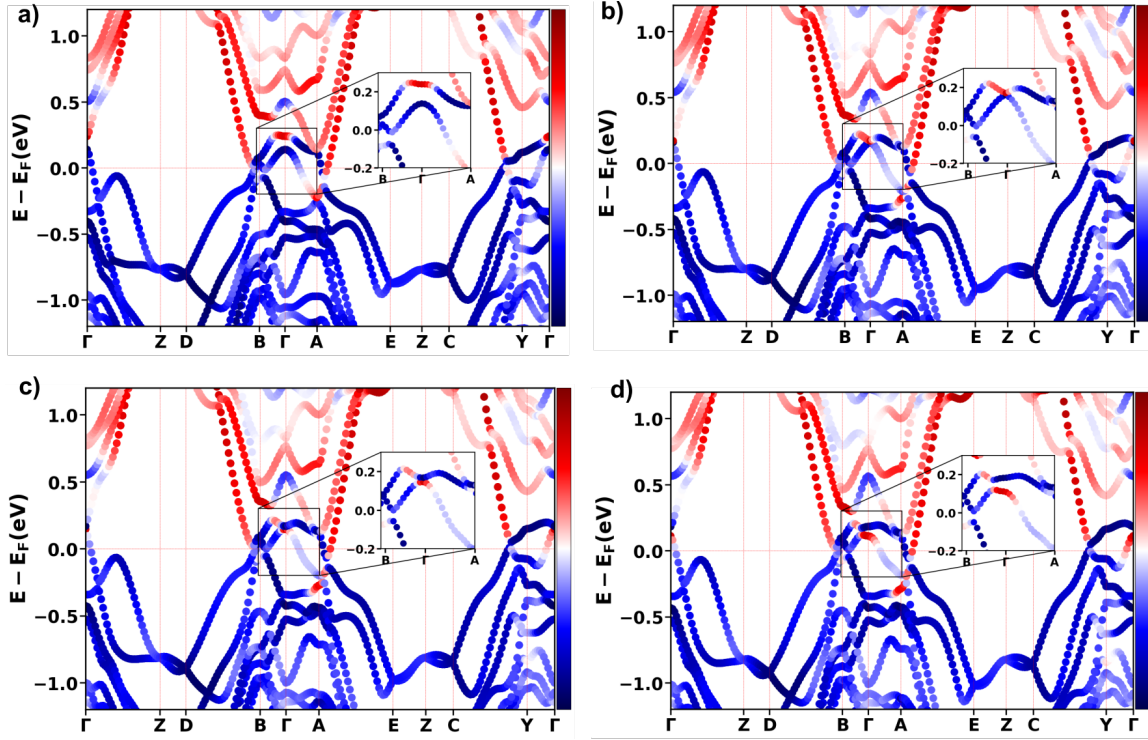


Figure 2.5: (a) The orbital projected band structure at 2 GPa. The band inversions are similar to the one seen at 0 GPa. However the gap at Γ has decreased. The band structure (b) 4.5 GPa (c) 5.5 GPa and (d) 7 GPa are shown subsequently. As the pressure rises, the band gap progressively decreases and beyond 4.5 GPa, a band inversion comes about at Γ , with a small gap, as seen in (c). With further pressure increase, the band gap at Γ increases with the retention of band inversion

of windings the time reversal polarization takes around the cylinder, as the external parameter changes from 0 to π , gives a measure of the Z_2 associated with the plane, denoted as Δ . This time reversal polarisation is in fact defined as the sum of HWCCs. In this formalism, the Z_2 invariant becomes,

$$\begin{aligned}\nu_0 &= \Delta(k_i = 0) + \Delta(k_i = 0.5) \bmod 2 \\ \nu_i &= \Delta(k_i = 0.5)\end{aligned}\tag{2.2}$$

where Δ , which is the Chern number of the fictitious 2D system, is related to the number of times any line crosses the HWCC line while the external parameter changes from 0 to $\frac{\pi}{a}$. Figure 2.3 shows the WCCs for TaSe₃ at 0 GPa in Time Reversal invariant planes, $k_x = 0$, $k_x = \frac{\pi}{a}$, $k_y = 0$, $k_y = \frac{\pi}{b}$, $k_z = 0$ and $k_z = \frac{\pi}{c}$. The Chern number Δ is 1 for $k_x = 0, k_x = \frac{\pi}{a}$, $k_z = 0$ and $k_z = \frac{\pi}{c}$, while it is 0 for $k_y = 0$ and $k_y = \frac{\pi}{b}$. Now, according to Eq. 2.2, the topological indices turn out to be (0;101) at 0 GPa, confirming that it's weak TI at 0 GPa. A similar WTI nature was reported by Hyun et.al.^[17] as well. We have carried out detailed computational study based on experimental analysis of the system under pressure. Since application of pressure may lead to a structural phase transition in some materials, high pressure X-Ray Diffraction (XRD) was conducted by the experimental counterpart, which shows a persistent peak corresponding to the monoclinic P21/m until a pressure of 13 GPa, with no new peaks appearing. This indicates that the material retains the same structure till very high pressures. Fig. 2.4(a) shows the axial ratios of the lattice constants, which show a discontinuity in the slope at around 3 GPa and 8 GPa. These two pressure points thus hint at possible phase transitions in the system. The isostructural phase transitions observed were further analyzed experimentally using Raman spectroscopy. As the system undergoes compression, the frequencies of the Raman modes are expected to show hardening. However, most of the modes as shown in Fig. 2.4(b) and (c) deviate from this expected behaviour at around 7.8 GPa. Additionally, the A_g and A_{1g} modes exhibit an additional slope change at

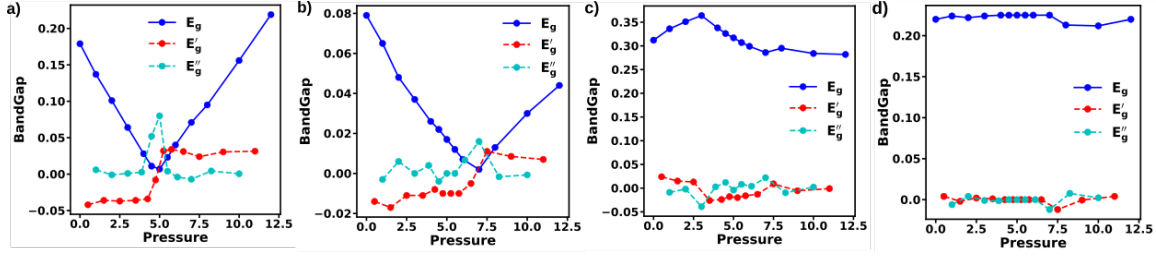


Figure 2.6: The change in band gap with pressure at the TRIM points (a) Γ , (b) B , (c) A , (d) Y . The first and second derivative of band gap with pressure is also plotted. (a) The band gap closes and reopens at the Γ point at around 5 GPa while at B , the gap closes and reopens at 7 GPa.

3 GPa. Furthermore, the Full Width Half Maxima (FWHM) of the various Raman modes also corroborate this, owing to the anomalous slope change of the Raman linewidth in some modes. These are the pressures at which the lattice constant ratios also change abruptly. Since it does not correspond to a structural transition, the origin of these changes have to be studied in detail. To this end, further simulations were performed to understand the nature of the observed phase transitions.

Changes in Electronic Band Structure under Pressure

For the range of pressures studied experimentally, we calculated the electronic band structure, out of which some selected pressures, 2 GPa, 4.5 GPa, 5.5 GPa and 7 GPa, are depicted in Fig. 2.5. With the increase in pressure from 2 GPa to 5.5 GPa (shown in Fig. 2.5(a) to (c)), the band gap at the Γ -point decreases with an eventual band inversion beyond 4.5 GPa. At pressures above 4.5 GPa, the valence band maxima at Γ shows the Ta d-orbital nature and the conduction band minima acquires a Se-p nature (Fig. 2.5 (c)). It is also seen that as the pressure is increased further, the Ta d orbital character seeps deeper into the valence band at the BZ centre and vice-versa. The band gap at 5.5 GPa is non-zero, but very small. However, with more pressure, the band gap at Γ increases, which is reported in Fig. 2.5(d). The parity eigenvalues of the valence band and conduction band, at the Γ point are opposite to each other in the pressure range 4.5 GPa to 6.5 GPa. Thus, in this pressure range, an odd number of band inversions exist in the BZ, implying a strong topological

insulator phase. However, a weak topological insulator phase is observed beyond 6.5 GPa. At pressures above 6.5 GPa, we see a change in the parity eigenvalue of the valence band at B , which leaves behind an even number of band inversions, leading to a weak topological insulator. This implies a band closing at the Γ point at the lower pressure and a band gap closing at the B point at the higher pressure. Fig. 2.6 shows the change in band gap with pressure at the TRIM points Γ, Y, B and A points. We chose these TRIM points because the band inversion is seen at these points. The band gap undergoes much less change at the A and Y points. However, a significant change in band gap is observed at Γ and B points. We see that around 4.5 GPa, at the Γ , the band gap closes, while the band gap at B closes at 6.5 GPa to 7 GPa range. Thus we observe two pressures, 4.5 GPa and 7 GPa, where the band gap closes and reopens with a change in parity. Such closing and the reopening of band gap with band inversion is a signature of a topological phase transition. Thus, we can conclude that the experimentally observed transitions are topological quantum phase transitions, which are brought about by the change in the nature of electronic bands at the TRIM points, Γ and B .

Pressure	Z	D	B	Γ	A	E	C	Y	Z_2
0 - 4.5 GPa	-1	-1	+1	-1	-1	-1	-1	+1	(0;101)
5 - 6 GPa	-1	-1	+1	+1	-1	-1	-1	+1	(1;101)
7 - 12 GPa	-1	-1	-1	+1	-1	-1	-1	+1	(0;100)

Table 2.1: The product of parity eigenvalues of the occupied bands at the high symmetry points for three different pressure ranges, 0 to 4.5 GPa, corresponding to the first weak topological insulator phase, 5.0 to 6.0 GPa, which marks the strong topological insulator phase and 7.0 to 12.0 GPa, which is the second weak topological phase. Their respective Z_2 invariants obtained from Fu-Kane parity analysis^[26] are reported in the last column.

The change in the topological nature of TaSe_3 , is quantified by calculating the Z_2 invariant. The product of parity eigenvalues (δ_i) at all the 8 TRIM points and the obtained Z_2 values, for pressures up to 12 GPa are reported in Table 3A.1. The Z_2 invariant of TaSe_3 is (0;101) from 0 GPa to 4.5 GPa. That is, upto a pressure of 4.5 GPa, the material remains in the same weak topological insulator phase that it

had at 0 GPa. At 5 GPa, δ_i becomes -1 at Γ , thus modifying the Z_2 invariant above 5 GPa, till around 7 GPa. In this region, ν_0 , the strong topological index, changes to 1. This is a strong topological phase. The consequence is that from 5 GPa to 6 GPa, all the surfaces of TaSe₃ hosts Topological Surface States (TSS), which are wavefunctions that no disorder can localise, provided TRS is not broken. These TSSs harbour an odd number of Dirac cones on the surfaces. As the pressure is raised even more, the B shows a change in the product of parity eigenvalues, which modifies the Z_2 invariant to (0;100), undoubtedly signalling a weak topological state. It must be noted that the two weak phases have different weak indices. One can adiabatically transform from a weak topological insulator phase to a stack of 2D quantum spin hall insulators, such that the weak indices denote the stacking direction. The stacking direction in the 0 GPa to 4.5 GPa range WTI phase is 101, while above 6.5 GPa, the weak indices are 100. They denote the topologically dark surfaces in the respective phases, where no Dirac cone is present. However, all the surfaces perpendicular to this direction hosts an even number of Dirac nodes. This analysis was further confirmed from the evolution of Wannier Charge Centres as well.

2.3.1 The Dirac Cone on TaSe₃ surface

We have calculated the surface spectrum of TaSe₃ at the three different phases observed to identify the Dirac nodes on the surface. To obtain the surface spectrum, first the surface Green's function of a semi-infinite slab system is obtained using the iterative Green's function approach, whose imaginary part is then directly related to the surface wavefunctions^[28]. The bulk-boundary correspondence necessitates that topologically protected surface states must exist on these topological insulator phases. The surface spectrum was investigated at 0 GPa, 5.5 GPa and 8 GPa, representing the (101) WTI phase, the STI phase and the (100) WTI phase respectively. The results are reported in Figure 2.7. The (10 $\bar{1}$) plane, which is also the natural cleavage plane of TaSe₃, at 0 GPa shows no Dirac cone (Fig.2.7(a)), as expected from the Z_2

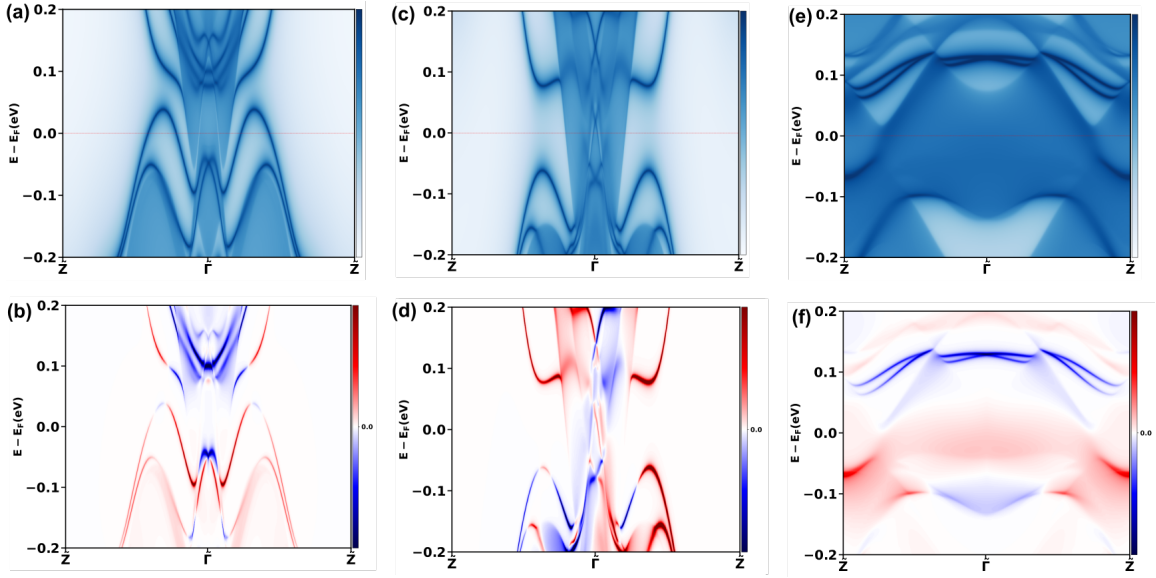


Figure 2.7: The surface spectrum and spin density difference on TaSe_3 surface at various pressures. (a) and (b) show the surface spectrum on the $(10\bar{1})$ plane and the up and down spin density on the same, at 0 GPa. At 5.5 GPa, since we expect all surfaces to host the Dirac point, we have chosen $(10\bar{1})$ plane, which is the natural cleavage plane of TaSe_3 as well. (c)- (d) show the surface spectrum of TaSe_3 at 5.5 GPa, on the $(10\bar{1})$ plane. (e) and (f) are the surface spectrum and spin density difference on the 100 plane at 8 GPa.

indices. Figure 2.7(b) shows spin polarisation on the $(10\bar{1})$ plane at 0 GPa. Near the conduction band at Γ , there is, however, a band splitting, which is Rashba-like, which is a consequence of the strong SOC, combined with the presence of an asymmetric potential at the interface. The two spin channels clearly separate into their own bands which are parabolic. The situation at 5.5 GPa is different. The surface spectrum on the 101 plane at 5.5 GPa, as shown in Fig. 2.7 (c) and its respective spin density difference, given in Fig. 2.7(d), has an unambiguous presence of a Dirac cone at the Γ point. The spin up and spin down channels show linear Dirac like dispersion at Γ . Such a dispersion on a surface, with spin-momentum locking, unequivocally points to the strong topological nature of TaSe_3 at 5.5 GPa. According to the Z_2 invariant, the (100) plane should have no Dirac cone at 8 GPa. This is indeed what is observed, as given in Fig. 2.7 (e) and (f). We thus characterise the strong and weak topological phases of TaSe_3 , arising with the change in pressure. The surface spectrum and the spin density difference offers a clear evidence to the fact that at ambient conditions,

TaSe₃ is a WTI and it evolves into a STI as the pressure is increased and then transitions to a WTI, with more increase in pressure. Thus the phase transitions observed in TaSe₃ under hydrostatic pressure, are TQPTs.

2.4 Conclusion and Discussion

To conclude, experimental probing of the system reveals two pressure points where TaSe₃ undergoes phase transitions, 3 GPa and 8 GPa. These transitions have been confirmed to be isostructural. Our DFT analysis of the system, reveals that the two transitions that the system goes through are topological quantum phase transitions. However, the critical points are different in experiment and in theoretical calculations. This kind of mismatch between experiments and theory is observed quite commonly. For example, there is discrepancy between the experimental and theoretical transition points in Sb₂Se₃^[33,34], BiTeI^[35], 1T-TiTe₂^[36], TiSe₂^[37], to name a few. DFT estimates of lattice parameters in a system is equal to the experimentally observed values, within an error bar. This in turn will affect all the subsequent calculations performed using DFT, leading to a mismatch with the experimental data. Another factor that may influence this mismatch is the formation of Se vacancies in TaSe₃, which may lead to an internal strain in the sample. The internal strain in TaSe₃, often gets created due to the formation of Se vacancies, impacting the experimental values of transition pressures^[17].

In fact, the first principles simulations were used to understand and explain the experimentally observed phase transitions. We confirm that the phase transitions observed are topological quantum phase transitions. As the system is subjected to hydrostatic pressure, we observe that the material shows two TQPT. Unlike seen in the application of unilateral or bilateral strain, where the material eventually transitions to a trivial insulator^{[18][17]}, the non-trivial phase exists until the largest pressure we have considered, around 12 GPa. However, we identified three different topological

phases that TaSe_3 can have under high pressure. Below 5 GPa, the material is a weak topological insulator, with the (101) direction showing a lack of Dirac cones. A weak topological phase exists at pressures above 7 GPa as well, which exhibits a different stacking direction, (100). Between these two WTI phases, the material becomes a strong topological insulator, which hosts robust surface states, with a single Dirac cone at Γ . Through our work, we have tried to enrich the phase diagram of superconducting material TaSe_3 and shed light on the significance of this material in realising Majorana fermions, via the possible coexistence of non-trivial topology and superconductivity. Moreover, it's a promising material for various device applications, owing to the controllability of its TSS hosting planes, via pressure. More studies on TaSe_3 and its feasibility as a device are pertinent to reveal its importance.

Bibliography

- [1] D. J. Thouless, M. Kohmoto, M. P. Nightingale, and M. den Nijs, "Quantized hall conductance in a two-dimensional periodic potential," *Physical review letters*, vol. 49, no. 6, p. 405, 1982.
- [2] M. Z. Hasan and C. L. Kane, "Colloquium: topological insulators," *Reviews of modern physics*, vol. 82, no. 4, p. 3045, 2010.
- [3] X.-L. Qi and S.-C. Zhang, "Topological insulators and superconductors," *Reviews of modern physics*, vol. 83, no. 4, p. 1057, 2011.
- [4] M. Sato and Y. Ando, "Topological superconductors: a review," *Reports on Progress in Physics*, vol. 80, no. 7, p. 076501, 2017.
- [5] C. Nayak, S. H. Simon, A. Stern, M. Freedman, and S. Das Sarma, "Non-abelian anyons and topological quantum computation," *Reviews of Modern Physics*, vol. 80, no. 3, pp. 1083–1159, 2008.

- [6] F. Wilczek, “Majorana returns,” *Nature Physics*, vol. 5, no. 9, pp. 614–618, 2009.
- [7] A. Y. Kitaev, “Fault-tolerant quantum computation by anyons,” *Annals of physics*, vol. 303, no. 1, pp. 2–30, 2003.
- [8] L. Fu and C. L. Kane, “Superconducting proximity effect and majorana fermions at the surface of a topological insulator,” *Physical review letters*, vol. 100, no. 9, p. 096407, 2008.
- [9] B. Yan, M. Jansen, and C. Felser, “A large-energy-gap oxide topological insulator based on the superconductor BaBiO₃,” *Nature Physics*, vol. 9, no. 11, pp. 709–711, 2013.
- [10] Z. Wang, P. Zhang, G. Xu, L. Zeng, H. Miao, X. Xu, T. Qian, H. Weng, P. Richard, A. V. Fedorov, *et al.*, “Topological nature of the FeSe_{0.5}Te_{0.5} superconductor,” *Physical Review B*, vol. 92, no. 11, p. 115119, 2015.
- [11] G. Xu, B. Lian, P. Tang, X.-L. Qi, and S.-C. Zhang, “Topological superconductivity on the surface of Fe-based superconductors,” *Physical review letters*, vol. 117, no. 4, p. 047001, 2016.
- [12] P. Haen, F. Lapierre, P. Monceau, M. N. Regueiro, and J. Richard, “Low temperature phase transition in the chain-like compounds NbSe₃ and TaSe₃,” *Solid State Communications*, vol. 26, no. 11, pp. 725–730, 1978.
- [13] S. Nie, L. Xing, R. Jin, W. Xie, Z. Wang, and F. B. Prinz, “Topological phases in the TaSe₃ compound,” *Physical Review B*, vol. 98, no. 12, p. 125143, 2018.
- [14] W. Xia, X. Shi, Y. Zhang, H. Su, Q. Wang, L. Ding, L. Chen, X. Wang, Z. Zou, N. Yu, L. Pi, Y. Hao, B. Li, Z. Zhu, W. Zhao, X. Kou, and Y. Guo, “Bulk fermi surface of the layered superconductor TaSe₃ with three-dimensional strong topological state,” *Phys. Rev. B*, vol. 101, p. 155117, Apr 2020.

- [15] A. I. U. Saleheen, R. Chapai, L. Xing, R. Nepal, D. Gong, X. Gui, W. Xie, D. P. Young, E. W. Plummer, and R. Jin, “Evidence for topological semimetallicity in a chain-compound TaSe_3 ,” *npj Quantum Materials*, vol. 5, p. 53, Jul 2020.
- [16] C. Chen, A. Liang, S. Liu, S. Nie, J. Huang, M. Wang, Y. Li, D. Pei, H. Yang, H. Zheng, *et al.*, “Observation of topological electronic structure in quasi-1d superconductor TaSe_3 ,” *Matter*, vol. 3, no. 6, pp. 2055–2065, 2020.
- [17] J. Hyun, M. Y. Jeong, M.-C. Jung, Y. Lee, Y. Kim, S. Jung, B. Seok, J. Song, C.-y. Lim, J. Cha, *et al.*, “Strain-controlled evolution of electronic structure indicating topological phase transition in the quasi-one dimensional superconductor TaSe_3 ,” *Physical Review B*, vol. 105, no. 11, p. 115143, 2022.
- [18] C. Lin, M. Ochi, R. Noguchi, K. Kuroda, M. Sakoda, A. Nomura, M. Tsubota, P. Zhang, C. Bareille, K. Kurokawa, *et al.*, “Visualization of the strain-induced topological phase transition in a quasi-one-dimensional superconductor TaSe_3 ,” *Nature Materials*, vol. 20, no. 8, pp. 1093–1099, 2021.
- [19] P. Giannozzi, S. Baroni, N. Bonini, M. Calandra, R. Car, C. Cavazzoni, D. Ceresoli, G. L. Chiarotti, M. Cococcioni, I. Dabo, *et al.*, “QUANTUM ESPRESSO: a modular and open-source software project for quantum simulations of materials,” *Journal of Physics: Condensed Matter*, vol. 21, p. 395502, sep 2009.
- [20] P. Giannozzi, O. Andreussi, T. Brumme, O. Bunau, M. B. Nardelli, M. Calandra, R. Car, C. Cavazzoni, D. Ceresoli, M. Cococcioni, *et al.*, “Advanced capabilities for materials modelling with quantum espresso,” *Journal of Physics: Condensed Matter*, vol. 29, p. 465901, oct 2017.
- [21] P. Giannozzi, O. Baseggio, P. Bonfà, D. Brunato, R. Car, I. Carnimeo, C. Cavazzoni, S. De Gironcoli, P. Delugas, F. Ferrari Ruffino, *et al.*, “Quantum

- ESPRESSO toward the exascale,” *The Journal of Chemical Physics*, vol. 152, no. 15, p. 154105, 2020.
- [22] J. P. Perdew, K. Burke, and M. Ernzerhof, “Generalized Gradient Approximation made simple,” *Phys. Rev. Lett.*, vol. 77, pp. 3865–3868, Oct 1996.
- [23] D. R. Hamann, “Optimized norm-conserving Vanderbilt pseudopotentials,” *Phys. Rev. B*, vol. 88, p. 085117, Aug 2013.
- [24] S. Grimme, J. Antony, S. Ehrlich, and H. Krieg, “A consistent and accurate ab initio parametrization of density functional dispersion correction (DFT-D) for the 94 elements H-Pu,” *The Journal of Chemical Physics*, vol. 132, p. 154104, 04 2010.
- [25] S. Grimme, J. Antony, S. Ehrlich, and H. Krieg, “A consistent and accurate ab initio parametrization of density functional dispersion correction (DFT-D) for the 94 elements H-Pu,” *The Journal of Chemical Physics*, vol. 132, p. 154104, 04 2010.
- [26] L. Fu and C. L. Kane, “Topological insulators with inversion symmetry,” *Phys. Rev. B*, vol. 76, p. 045302, Jul 2007.
- [27] M. Iraola, J. L. Mañes, B. Bradlyn, M. K. Horton, T. Neupert, M. G. Vergniory, and S. S. Tsirkin, “IrRep: Symmetry eigenvalues and irreducible representations of ab initio band structures,” *Computer Physics Communications*, vol. 272, p. 108226, 2022.
- [28] Q. Wu, S. Zhang, H.-F. Song, M. Troyer, and A. A. Soluyanov, “Wanniertools: An open-source software package for novel topological materials,” *Computer Physics Communications*, vol. 224, pp. 405–416, 2018.
- [29] G. Pizzi, V. Vitale, R. Arita, S. Blügel, F. Freimuth, G. Géranton, M. Gibertini, D. Gresch, C. Johnson, T. Koretsune, J. Ibañez-Azpiroz, H. Lee, J.-M. Lihm,

- D. Marchand, A. Marrazzo, Y. Mokrousov, J. I. Mustafa, Y. Nohara, Y. Nomura, L. Paulatto, S. Poncé, T. Ponweiser, J. Qiao, F. Thöle, S. S. Tsirkin, M. Wierzbowska, N. Marzari, D. Vanderbilt, I. Souza, A. A. Mostofi, and J. R. Yates, “Wannier90 as a community code: new features and applications,” *Journal of Physics: Condensed Matter*, vol. 32, p. 165902, jan 2020.
- [30] K. Hayashi, A. Kawamura, and K. Komai, “Control of phase transition in tase3,” *Materials research bulletin*, vol. 22, no. 10, pp. 1341–1345, 1987.
- [31] M. Z. Hasan and C. L. Kane, “Colloquium: Topological insulators,” *Rev. Mod. Phys.*, vol. 82, pp. 3045–3067, Nov 2010.
- [32] D. Gresch, G. Autès, O. V. Yazyev, M. Troyer, D. Vanderbilt, B. A. Bernevig, and A. A. Soluyanov, “Z2pack: Numerical implementation of hybrid Wannier centers for identifying topological materials,” *Phys. Rev. B*, vol. 95, p. 075146, Feb 2017.
- [33] W. Li, X.-Y. Wei, J.-X. Zhu, C. Ting, and Y. Chen, “Pressure-induced topological quantum phase transition in Sb_2Se_3 ,” *Physical Review B*, vol. 89, no. 3, p. 035101, 2014.
- [34] A. Bera, K. Pal, D. Muthu, S. Sen, P. Guptasarma, U. V. Waghmare, and A. Sood, “Sharp raman anomalies and broken adiabaticity at a pressure induced transition from band to topological insulator in Sb_2Se_3 ,” *Physical review letters*, vol. 110, no. 10, p. 107401, 2013.
- [35] Y. S. Ponomov, T. V. Kuznetsova, O. E. Tereshchenko, K. A. Kokh, and E. V. Chulkov, “Dynamics of the bte lattice at high pressures,” *JETP letters*, vol. 98, pp. 557–561, 2014.
- [36] V. Rajaji, U. Dutta, P. Sreeparvathy, S. C. Sarma, Y. Sorb, B. Joseph, S. Sahoo, S. C. Peter, V. Kanchana, and C. Narayana, “Structural, vibrational, and

- electrical properties of 1T-TiTe₂ under hydrostatic pressure: Experiments and theory,” *Physical review B*, vol. 97, no. 8, p. 085107, 2018.
- [37] V. Rajaji, S. Janaky, S. C. Sarma, S. C. Peter, and C. Narayana, “Pressure induced topological and structural phase transitions in 1t-tise2: a raman study,” *Journal of Physics: Condensed Matter*, vol. 31, no. 16, p. 165401, 2019.

Topological Phases of (Sb₂Te₃)_m(Sb₂)_n Homologous Series

3A.1 Introduction

Recently, in both theoretical and experimental condensed matter physics, identifying new materials as topological insulators have been at the forefront of study. This is primarily because, topological insulators find applications in a wide variety of areas. One such field with potential applications of topological insulators, is the field of thermoelectrics. This increasing attention on topological insulators from the point of view of advancing thermoelectrics was marked by the discovery of first generation 3D topological insulators. In fact, the first 3D topological insulator to be realised experimentally was the Bi_{1-x}Sb_x alloy^[1], which is a well-known thermoelectric material. The observed surface spectrum of this semiconductor alloy was complicated and the

** The work reported in this chapter is to be submitted soon for publication : S. Das, P. Acharyya, S. Biswas, R.K. Biswas, A.G. Francis, S.K. Pati, K. Biswas

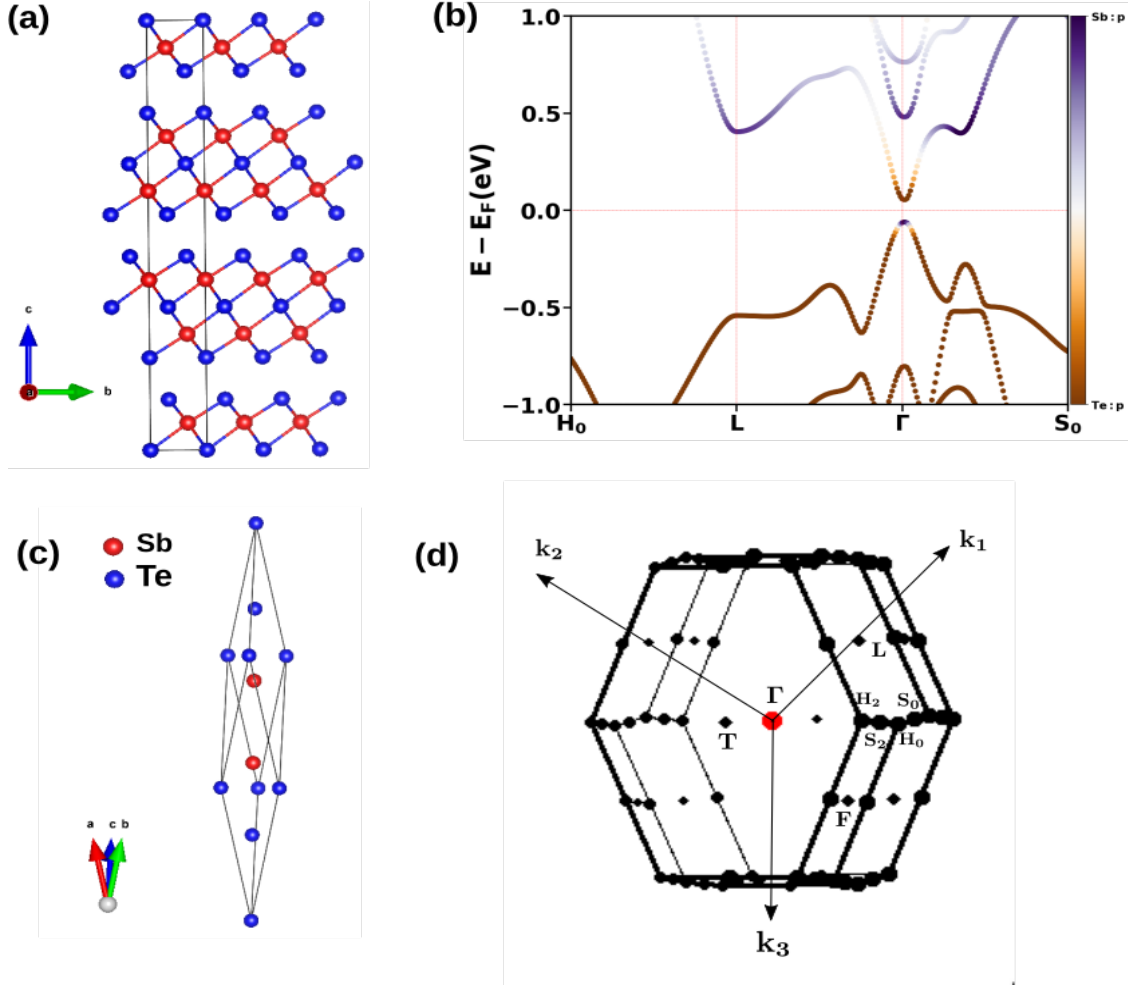


Figure 3A.1: a) The crystal structure of Sb_2Te_3 in the $R\bar{3}m$ space group. The primitive cell is given in (c). (b) The band structure of Sb_2Te_3 with the Sb and Te orbital projection. The High symmetry points in the Brillouin zone are represented in (d). The band structure (b) shows a band inversion at Γ

band gap was very narrow. This motivated the search for materials with a simpler surface spectrum and a larger band gap, which lead to the second generation 3D topological insulators, including Bi_2Se_3 ^[2,3], Bi_2Te_3 ^[4,5] and Sb_2Te_3 ^[3,6]. Interestingly they are also the one of the best thermoelectric materials near the room temperature and below^[7]. A way to gauge the performance of a thermoelectric material is to calculate a dimensionless quantity called figure of merit, $zT = S^2\sigma/(\kappa_e + \kappa_{ph})T$, where S is the Seebeck coefficient, σ , the electrical conductivity, κ_e the thermal conductivity due to electrons and κ_{ph} , the lattice thermal conductivity. Currently, the peak of zT

of most of the good thermoelectric materials lie in the range of $1 - 2$. A superlattice of Bi_2Te_3 and Sb_2Te_3 alternating layers reportedly shows a zT of about $2.4^{[8]}$. This in fact is the highest zT value observed in any material at room temperature, so far. Thus, topological insulators and thermoelectrics seem to be closely intertwined.

Topological insulators are known for their unusual property of an insulator-like behaviour in the bulk, while not quite behaving like an insulator. They are materials which exhibit gapless metallic surface states, even though their bulk has a finite gap. These gapless edge or surface modes are robust against non-magnetic disorder or impurity or dopings. They are protected from back scattering from impurities and at low temperature gives rise to ballistic transport at the interfaces. The influence of these surface states on thermoelectrics can be profound. The surface states make a superior conduction channel in topological materials, which can be retained in the process of doping or Fermi-level tuning to improve the thermoelectric performance. This added benefit of the topological surface states offer additional control to tune thermoelectric figure of merit. While the surface states are protected against doping or other defects, the phonons, however, are not. Thus the processes, such as doping can help in reducing the lattice thermal conductivity, while the electrical conductivity from surfaces can be retained. At lower temperatures, where the surface contribution to the electrical conductivity is larger than the bulk contribution, the thermoelectric figure of merit can potentially be tuned to reach high thermoelectric efficiency.

Discovery of topologically non-trivial materials which can be potential thermoelectric candidates is thus a new area of interest. The homologous series of $(\text{Sb}_2\text{Te}_3)_m(\text{Sb}_2)_n$ is a series of materials which have Sb_2Te_3 ($m = 1, n = 0$) and Sb_2 ($m = 0, n = 1$) as the building blocks. Sb_2Te_3 is a well-known TI, while Sb_2 is a topological semi metal^[9,10]. The series has materials which are formed by the Sb_2Te_3 quintuple layers interspersed with Sb_2 layers. A comprehensive study on this series is currently lacking in the literature, from thermoelectric or topological point of view. A deep analysis of the structure-property relationship of this series can offer us new ways to

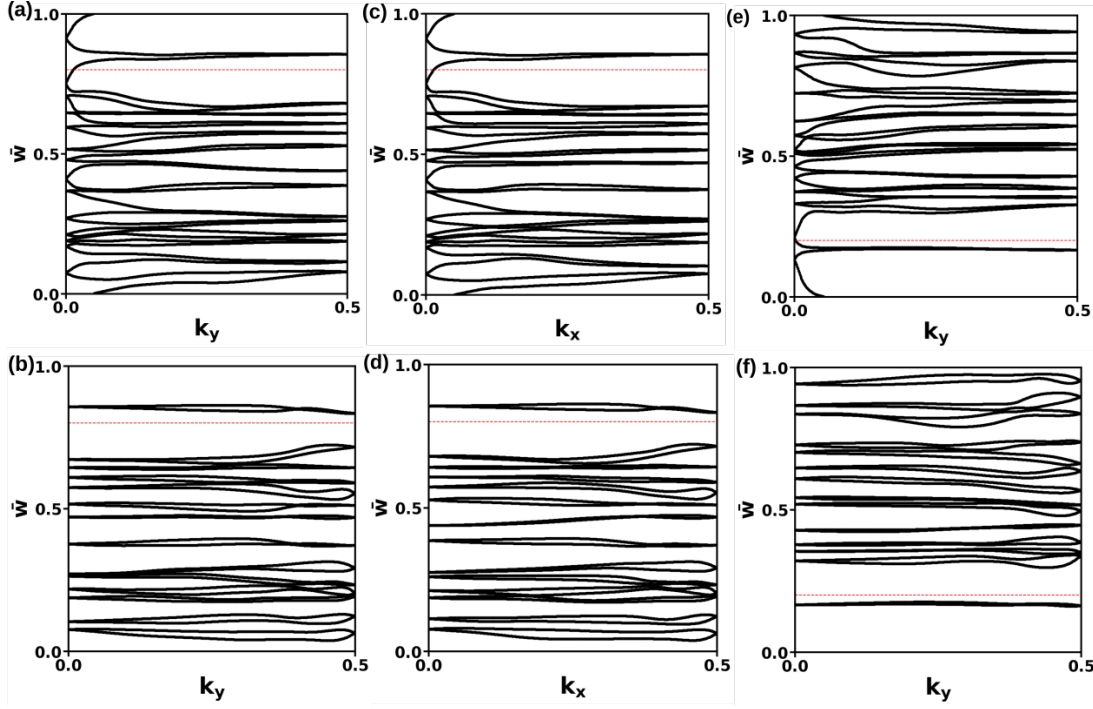


Figure 3A.2: a) The evolution of HWCCs on the $k_x = 0$ plane and (b) $k_x = \pi/a$ plane. The red line is chosen randomly and it is seen that on $k_x = 0$, it cuts the HWCC line once, making $\Delta = 1$, while on $k_x = \pi/a$, it cuts the HWCC evolution line zero times. Similarly, we see that (c) for $k_y = 0$ and (e) $k_z = 0$, $\Delta = 1$, and it is 0 for (d) $k_y = \pi/b$ and (f) $k_z = \pi/c$.

understand the topology in tandem with thermoelectricity.

In this chapter, we study a few members of $(\text{Sb}_2\text{Te}_3)_m(\text{Sb}_2)_n$ series with respect to their topological properties. The materials considered are Sb_2Te_3 - as a reference, Sb_2Te and SbTe . We have analysed the topological invariants, the surface spectrum and the Fermi contour of the surfaces of the systems to gain an in depth understanding of their topological state.

3A.2 Computational Methods

All the Density Functional Theory (DFT) calculations were performed using the Vienna Ab-initio Simulation Package (VASP)^[11,12], with plane wave basis set based on Projector Augmented Wave (PAW) pseudo potentials. The Generalized Gradient Approximation to the exchange-correlation potential was used in all the calculations,

as given by Perdew-Burke-Ernzerhof^[13]. The plane wave basis set was truncated by using an energy cutoff of 500 eV for all the systems. A Γ -centred k-grid was used for all the systems. For Sb_2Te_3 , we used a k-grid of dimension $8 \times 8 \times 8$, while for Sb_2Te and SbTe a k-grid of $12 \times 12 \times 4$ was used. Both the plane wave cut-off and the k-point grids were chosen by carefully analyzing the ground state energy convergence with respect to each of the parameters. A Gaussian smearing with a spread of 0.01 eV was used to take into account the partial filling of energy levels near the Fermi-level. We also used Spin-Orbit Coupling in all the band structure, topological invariant and surface state calculations. The topological invariant was calculated using the WannierTools software package^[14], by tracking the evolution of Hybrid Wannier Charge centres^[15]. The surface spectrum and the Fermi contour of designated surfaces are obtained from the imaginary part of the surface Green's function, which is also calculated from WannierTools. The tight binding Hamiltonian required for WannierTools was obtained from the Maximally Localised Wannier Functions, using Wannier90^[16] software.

3A.3 Results

The signature of a topologically non-trivial material is that electronic bands show band inversion at various time reversal invariant momenta (TRIM). All the structures show band inversion in their Brillouin Zone (BZ), as seen in Figs. 3A.1(b), 3A.4(c) and 3A.6(b). Sb_2Te_3 is a well known topological insulator. Our results exactly reproduce this already known nature of Sb_2Te_3 . The band structure of Sb_2Te_3 has a single band inversion, present at the centre of the Brillouin Zone, Γ . In the case of this homologous series, the conduction band is mainly of Sb-p character and the valence band nature is predominantly Te-p. At the Γ point this trend becomes the opposite, with everywhere else it retaining the expected nature. The other materials are not studied prior in regards to their topology. The band structure of Sb_2Te

shows a continuous gap and is inverted at Γ and A points. The band character on the conduction band and the valence band edges at these two points, are indistinguishable. Similarly SbTe also shows band inversion at M , Γ and A points, with a finite gap throughout the Brillouin Zone. Another interesting nature of the band structure of Sb_2Te and SbTe is the multiple conduction and valence band valleys present in the system. The electric transport properties are mostly determined by the top of the valence band and the bottom of the conduction band. This region in the band structure is termed as valley or carrier pocket, because of the specific morphology of the Fermi surface. The Seebeck coefficient, S and the electrical conductivity, σ are inversely connected to each other. Thus, just adjusting the Fermi-level can achieve only a limited success in bettering the thermoelectric figure of merit. Tuning the valley, however offers much more advantage. The valley degeneracy, N_v , is of particular importance in this regard. The thermoelectric materials with more valleys fair better than the case of a single valley, because they offer more number of states for the carriers to occupy and for transport^[17]. This large valley degeneracy in Sb_2Te and SbTe could be related to the extend of band inversion seen in both of them. The conduction band character is seen to “seep” much deep into the valence band and this corresponds to a large degree of band inversion. The topological nature of the series was further analysed by the calculation of the Z_2 invariants for each of the system. The evolution of the hybrid wannier charge centres (HWCCs) on cylinder of dimensions $S^1 \times 2\pi$, as the flux threading the cylinder changes from 0 to π , gives a description of the winding number for a given 2D plane of the 3D Brillouin zone. For all the systems, we calculated the Z_2 invariant for the six time reversal invariant planes, $k_x = 0$, $k_x = \pi/a$, $k_y = 0$, $k_y = \pi/b$, $k_z = 0$, $k_z = \pi/c$. For these fictitious 2D insulators, the Z_2 invariant is denoted as Δ . It takes value 1, if the number of times HWCC winds around the cylinder is odd, and 0, if it winds an even number of times. For any given parameter, say k_x , if the Δ changes as k_x goes from 0 to π/a , then the strong index of the system, ν_0 is 1. If none of the three, k_x , k_y or k_z

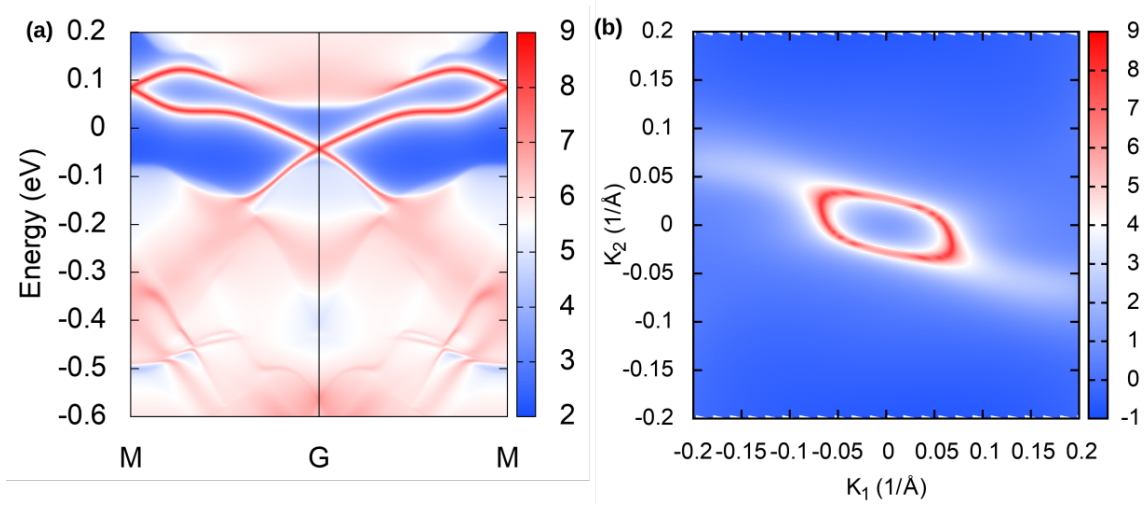


Figure 3A.3: a) The surface spectrum (simulated ARPES) of Sb_2Te_3 001 plane. The Γ -point has a distinct Dirac node. Note the linear dispersion seen on either side. (b) The corresponding Fermi arc on the surface. The Fermi surface forms a closed loop around Γ , suggesting a π Berry phase.

shows any change in Δ , as it slowly changes from 0 to π , then, ν_0 is 0. The weak indices are given by the Δ values at $k_x = \pi/a$, $k_y = \pi/b$ and $k_z = \pi/c$ ^[15,18]. The Z_2 invariants for each of the four systems is calculated and discussed in detail below, with the values summarized in Table 3A.1

Material	Z_2
Sb_2Te_3	(1;000)
Sb_2Te	(1;000)
SbTe	(1;000)

Table 3A.1: The calculated Z_2 invariants for Sb_2Te_3 , Sb_2Te and SbTe . All three systems have the strong topological index as zero, suggesting that they are strong topological insulators.

Sb_2Te_3

Sb_2Te_3 forms a layered structure along the c -axis, as given in Fig 3A.1(a). It belongs to the space group R-3m, and has a primitive cell as given in Fig. 3A.1(c). The band structure of Sb_2Te_3 is reported in Fig. 3A.1. The projections of the p orbitals of Sb and Te are given by the colours purple and orange respectively. As reported previously^[3], we see a band inversion at the centre of the Brillouin zone, with the

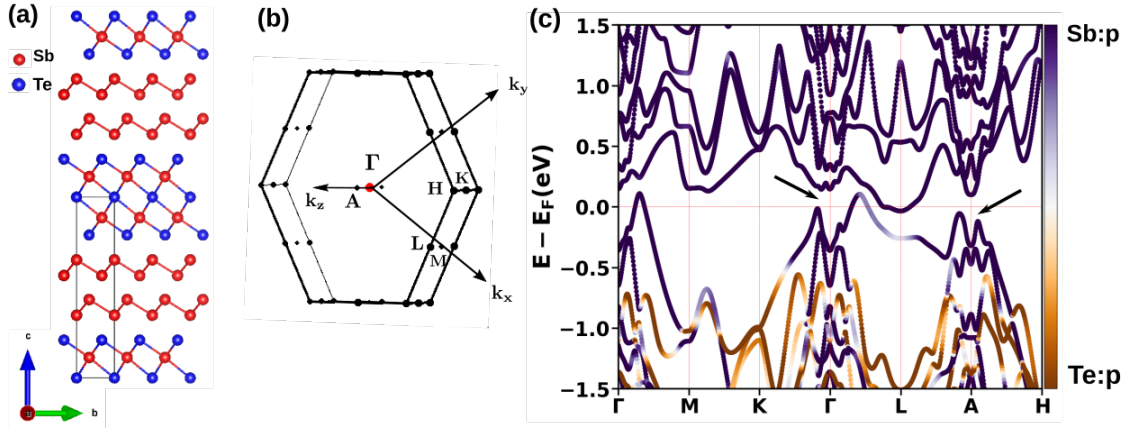


Figure 3A.4: a) Sb₂Te structure after optimization. It crystallizes in the P-3m1 spacegroup. A bilayer of Sb₂ exists between quintuple layers of Sb₂Te₃ (b) The Brillouin zone and the high symmetry points. (c) The band structure with SOC. The top valence band has a predominant conduction bands Sb-p orbital character. The highly parabolic conduction bands and the valence bands are extremely useful in the field of thermoelectrics.

orbital nature of Sb-p occurring on the valence band top and the Te-p orbital character appearing on the conduction band bottom. Furthermore, there exists a finite gap throughout the BZ, making it possible to classify the topology of the bands in this system.

The evolution of Wannier charge centres is shown in Fig. 3A.2. A line is drawn, which cuts the WCC curves as they evolve with the variation of an external parameter, which is plotted along the x-axis. On the $k_x = 0$ plane, given in Fig. 3A.2 (a), the line cuts the WCC curve at a single point. The same is observed on the $k_y = 0$ and

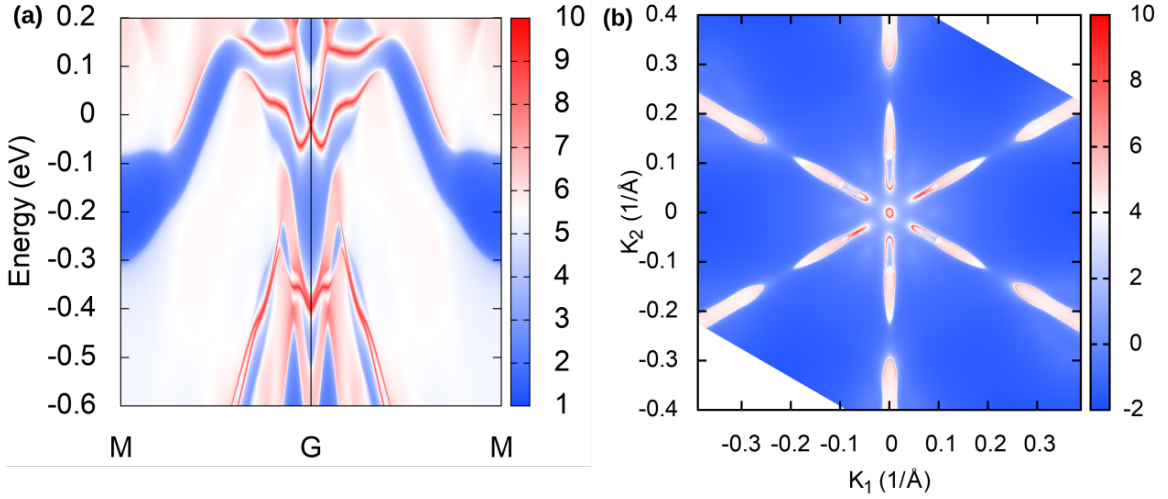


Figure 3A.5: (a) The 001 plane of Sb_2Te_3 showing the topological surface states. The Dirac cone is observed at the Γ point. (b) The Fermi surface of the 001 plane at the Fermi level. There are multiple electron pockets on the surface, formed by the surface states. These pockets are formed around Γ and the three in equivalent boundary points M , of the surface.

$k_z = 0$ plane, given in Fig. 3A.2 (c) and (e) respectively. The WCC evolution for $k_x = \pi/a$, $k_z = \pi/b$ and $k_z = \pi/c$ are shown in Fig. 3A.2 (b),(d) and (f), on which the line is shown to cut the WCC curve zero times, giving a Δ of 0 on these planes. It is clear that k_x , k_y and k_z changing from 0 to π/a , changes the Δ , making the strong index $\nu_0 = 1$. Thus, Sb_2Te_3 is a strong topological insulator.

This implies that any surface of Sb_2Te_3 can host an odd number of Dirac points. It has been shown previously that there exists a single Dirac cone on the surface of Sb_2Te_3 ^[3]. The surface spectrum was simulated by considering a semi-infinite slab system and constructing its surface Green's function. The simulated ARPES on the 001 plane of Sb_2Te_3 is given in Fig. 3A.3(a), which shows a single Dirac cone near the Fermi-level. This is a clear confirmation of the strong topological nature of Sb_2Te_3 . The surface Fermi surface as shown in Fig. 3A.3(b) is a circle around the Γ point. Thus the Fermi contour encircles the single Dirac point in the system. The Berry phase in this case is π , and this is typical in non-trivial topological systems.

Sb₂Te

In the case of Sb₂Te, we see a similar topological nature as Sb₂Te₃. The topological nature is reported for the first time in this system. The band structure given in Fig. 3A.4 is quite complicated, unlike the clean bands seen in Sb₂Te₃. In Sb₂Te, multiple Time Reversal Invariant Momenta (TRIM) points - Γ and A - show band inversion. At the TRIM point M, though VBM character is that of Te p orbital, the second VBM, shows an inverted nature. At the L point, the VBM does not have a predominant Tellurium p orbital or Antimony p orbital character. It has to be noted however, that the conduction band nature at all these special k-points retain the Sb p orbital character. The band edges are thus indistinguishable on either side of the Fermi level at Γ and A . This scenario can sometimes arise, when the conduction and valence bands cross and mix evenly. This kind of mixing has been observed in some other well-known topological insulators like Bi₂Te₃ and Bi₂Se₃^[19]. To understand the topological nature further, Z_2 calculation was done, especially because of the complex fat bands of the system. As compared to Sb₂Te₃, Sb₂Te has a large valley degeneracy. This valley degeneracy arises from orbital degeneracy, which corresponds to the case when the extrema of multiple valleys have similar energies, to the order of $k_B T$ ^[17]. The valley degeneracy corresponds to the number of distinct Fermi surface that exist at the Fermi level. Such a valley degeneracy is known to be extremely beneficial for thermoelectric applications. This valley degeneracy helps improve the Seebeck coefficient at a particular carrier concentration, without affecting the electrical conductivity^[17], by tuning the mass of the density of states.

The topological nature of Sb₂Te is confirmed from the evolution of HWCCs. The six TRIM planes have the Z_2 invariant, Δ as 1, 0, 1, 0, 1 and 0. This is calculated in the same way as above, where an arbitrary line is chosen and the number of times it cuts a particular WCC evolution line is counted. An even number of cuts leads to Δ of 0, while an odd number of cuts implies Δ is 1 for that plane. The value of Δ changes from 1 to 0 as k_x goes from 0 to π/a and similarly for k_y and k_z . This implies that

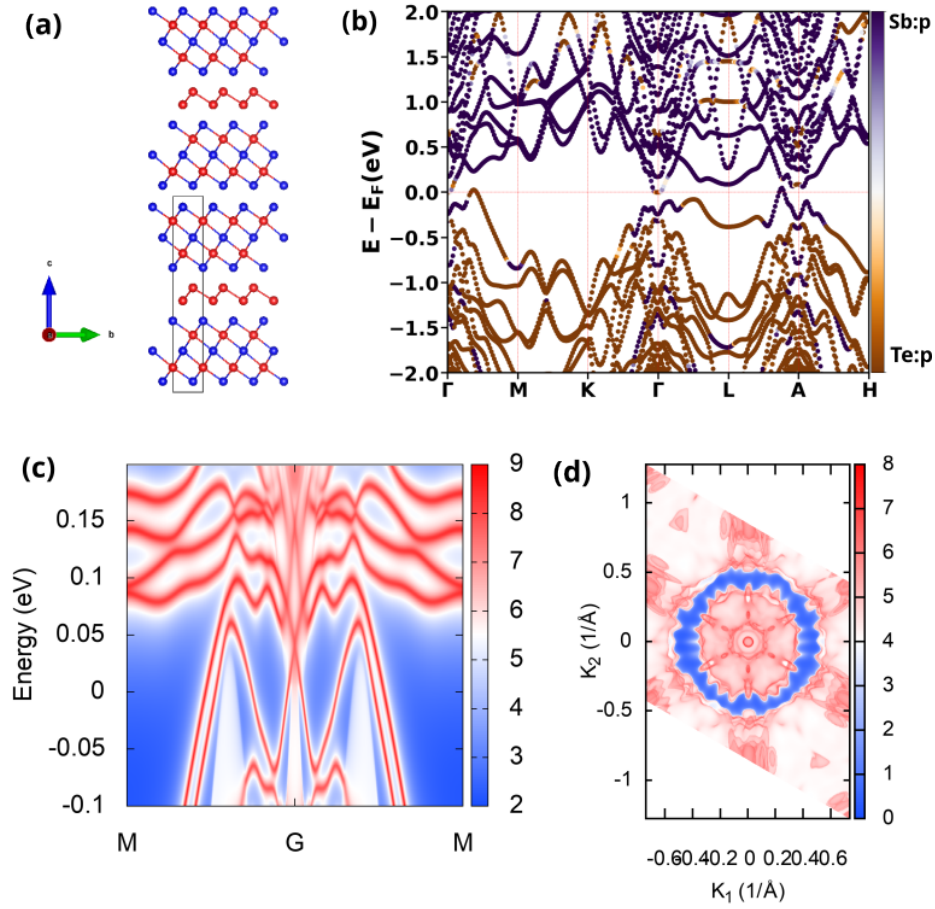


Figure 3A.6: (a) The SbTe structure, which crystallizes in P-3m1 space group. It is made up of alternating layers of Sb₂Te₃ quintuple layers and Sb₂ layers along the *c*-axis. (b) The calculated band structure (with SOC) along the high symmetry points in the BZ. Band inversions are visible at the M, Γ and A points. (c) The surface spectrum of the 010 plane of SbTe. There is a Dirac cone at the centre of the surface Brillouin zone d) The Fermi contour on the surface shows a non-trivial Berry phase

Sb₂Te is also a strong topological insulator with $\nu_0 = 1$.

The surface spectrum and the Fermi surface of the (001) plane is given in Fig 3A.5. The surface spectrum in Fig. 3A.5(a) has a Dirac cone at near the Fermi level. The dispersion at this point is linear and the can be described by the mass less Dirac equation. The linear dispersion signifies a spin-momentum locking in the system, with one spin channel along one direction and the other spin channel following the other direction. The Fermi surface shown in Fig. 3A.5(b) shows multiple Fermi circles on the 100 plane. The central lobe is around Γ , while there are pockets flanking the

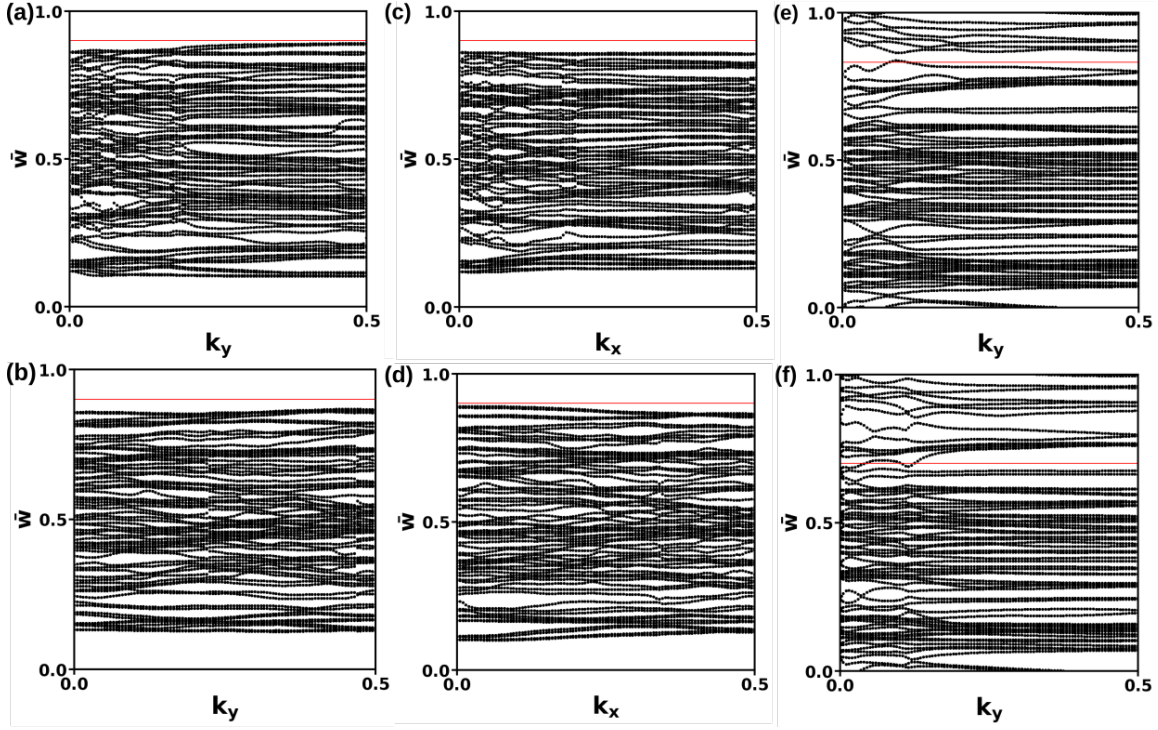


Figure 3A.7: The HWCC evolution on the 6 TRIM planes of SbTe. The Δ of $k_x = 0$, $k_x = \pi/a$, $k_y = 0$, $k_y = \pi/b$ and $k_z = 0$ is 0, as observed from the HWCC evolution shown in (a),(b),(c),(d) and (e) respectively. In (f), we see that the arbitrary line (in red), crosses the line an odd number of times, giving $\Delta = 1$

Γ point. Those pockets which do not circle around one of the four TRIM points on the 2D surface do not contribute to the topology. If the contour encircles an even number of Dirac points, then the Berry phase is trivial. However, an odd number of Dirac points within the Fermi contour, means a Berry phase of π , indicating non-trivial topology. This kind of Fermi surface has been observed in other similar materials like $\text{Bi}_{1-x}\text{Sb}_x$ ^[20]. The multiple Fermi pockets are direct indicators of the valley degeneracy in the system as well.

SbTe

To evaluate the band topology of SbTe, we first plotted the band structure. The obtained electronic bands are depicted in Fig. 3A.6. The band structure shows band inversion at Γ , M and A points. The presence of an odd number of inversions

clearly suggests non-trivial topology. The bands structure near the Fermi-level is quite complicated, similar to Sb_2Te and quite in contrast to Sb_2Te_3 . A number of valleys exist near the Fermi-level, having a similar energy to one another, within an energy range of $k_B T$ thereby increasing the valley degeneracy. This in fact, makes SbTe a very good thermoelectric material.

The Z_2 invariants for SbTe are calculated by analysing the change in Δ values, just as mentioned above. As observed in Fig. 3A.6, the Δ values for the TRIM planes, $k_x = 0$, $k_x = \pi/a$, $k_y = 0$, $k_y = \pi/b$, $k_z = 0$ are 0, while $k_z = \pi/c$ has a Δ value of 1. This implies that SbTe is also a strong topological insulator, which hosts an odd number of Dirac points on all its surfaces.

The robust surface states of SbTe are plotted in Fig. 3A.6. The Fig. shows the 010 plane of SbTe . At the Γ -point we see the Dirac point with linear dispersion. In fact, as the dispersion is linear, it is expected to bifurcate the two spin channels to two different directions, as was observed in Sb_2Te . The Fermi contour of the surface is reported in Fig. 3A.6, which reveal a non-trivial Berry phase.

3A.4 Conclusion

The topological nature of three members of the $(\text{Sb}_2\text{Te}_3)_m(\text{Sb}_2)_n$ homologous series was studied in detail in this chapter. These include Sb_2Te_3 , Sb_2Te , and SbTe . All the systems considered here show a non-trivial topology. We note that all three systems are strong topological insulators. Evidence for this is provided from multiple considerations. The odd number of band inversions, the calculated Z_2 invariants and the simulated ARPES spectra hosting an odd number of Dirac cones prove this to be the strong topological character of the system. Moreover, we notice that Sb_2Te and SbTe have band structures with multiple valley degeneracies and a complicated Fermi surface. The non-trivial topology combined with the rich band structure near the Fermi level can potentially make these materials good thermometric materials,

which can be fine-tuned in multiple ways, to push the limits of thermoelectrics.

Bibliography

- [1] D. Hsieh, D. Qian, L. Wray, Y. Xia, Y. S. Hor, R. J. Cava, and M. Z. Hasan, “A topological dirac insulator in a quantum spin hall phase,” *Nature*, vol. 452, pp. 970–974, Apr 2008.
- [2] Y. Xia, D. Qian, D. Hsieh, L. Wray, A. Pal, H. Lin, A. Bansil, D. Grauer, Y. S. Hor, R. J. Cava, and M. Z. Hasan, “Observation of a large-gap topological-insulator class with a single dirac cone on the surface,” *Nature Physics*, vol. 5, pp. 398–402, Jun 2009.
- [3] H. Zhang, C.-X. Liu, X.-L. Qi, X. Dai, Z. Fang, and S.-C. Zhang, “Topological insulators in Bi_2Se_3 , Bi_2Te_3 and Sb_2Te_3 with a single dirac cone on the surface,” *Nature Physics*, vol. 5, pp. 438–442, Jun 2009.
- [4] Y. L. Chen, J. G. Analytis, J.-H. Chu, Z. K. Liu, S.-K. Mo, X. L. Qi, H. J. Zhang, D. H. Lu, X. Dai, Z. Fang, S. C. Zhang, I. R. Fisher, Z. Hussain, and Z.-X. Shen, “Experimental realization of a three-dimensional topological insulator, Bi_2Te_3 ,” *Science*, vol. 325, no. 5937, pp. 178–181, 2009.
- [5] D. Hsieh, Y. Xia, D. Qian, L. Wray, J. H. Dil, F. Meier, J. Osterwalder, L. Patthey, J. G. Checkelsky, N. P. Ong, A. V. Fedorov, H. Lin, A. Bansil, D. Grauer, Y. S. Hor, R. J. Cava, and M. Z. Hasan, “A tunable topological insulator in the spin helical dirac transport regime,” *Nature*, vol. 460, pp. 1101–1105, Aug 2009.
- [6] D. Hsieh, Y. Xia, D. Qian, L. Wray, F. Meier, J. H. Dil, J. Osterwalder, L. Patthey, A. V. Fedorov, H. Lin, A. Bansil, D. Grauer, Y. S. Hor, R. J.

- Cava, and M. Z. Hasan, “Observation of time-reversal-protected single-dirac-cone topological-insulator states in bi_2te_3 and sb_2te_3 ,” *Phys. Rev. Lett.*, vol. 103, p. 146401, Sep 2009.
- [7] D. Baldomir and D. Faílde, “On behind the physics of the thermoelectricity of topological insulators,” *Scientific Reports*, vol. 9, p. 6324, Apr 2019.
- [8] R. Venkatasubramanian, E. Siivola, T. Colpitts, and B. O’Quinn, “Thin-film thermoelectric devices with high room-temperature figures of merit,” *Nature*, vol. 413, pp. 597–602, Oct 2001.
- [9] T. Kadono, K. Miyamoto, R. Nishimura, K. Kanomaru, S. Qiao, K. Shimada, H. Namatame, A. Kimura, and M. Taniguchi, “Direct evidence of spin-polarized band structure of $\text{Sb}(111)$ surface,” *Applied Physics Letters*, vol. 93, p. 252107, 12 2008.
- [10] J. C. Johannsen, G. Autès, A. Crepaldi, S. Moser, B. Casarin, F. Cilento, M. Zaccogna, H. Berger, A. Magrez, P. Bugnon, J. Avila, M. C. Asensio, F. Parmigiani, O. V. Yazyev, and M. Grioni, “Engineering the topological surface states in the $(\text{Sb}_2)_m - \text{sb}_2\text{te}_3$ ($m = 0 - -3$) superlattice series,” *Phys. Rev. B*, vol. 91, p. 201101, May 2015.
- [11] G. Kresse and J. Furthmüller, “Efficient iterative schemes for ab initio total-energy calculations using a plane-wave basis set,” *Phys. Rev. B*, vol. 54, pp. 11169–11186, Oct 1996.
- [12] G. Kresse and J. Hafner, “Ab initio molecular dynamics for liquid metals,” *Phys. Rev. B*, vol. 47, pp. 558–561, Jan 1993.
- [13] J. P. Perdew, K. Burke, and M. Ernzerhof, “Generalized gradient approximation made simple,” *Phys. Rev. Lett.*, vol. 77, pp. 3865–3868, Oct 1996.

-
- [14] Q. Wu, S. Zhang, H.-F. Song, M. Troyer, and A. A. Soluyanov, “Wanniertools: An open-source software package for novel topological materials,” *Computer Physics Communications*, vol. 224, pp. 405–416, 2018.
- [15] D. Gresch, G. Autès, O. V. Yazyev, M. Troyer, D. Vanderbilt, B. A. Bernevig, and A. A. Soluyanov, “Z2pack: Numerical implementation of hybrid wannier centers for identifying topological materials,” *Phys. Rev. B*, vol. 95, p. 075146, Feb 2017.
- [16] G. Pizzi, V. Vitale, R. Arita, S. Blügel, F. Freimuth, G. Géranton, M. Gibertini, D. Gresch, C. Johnson, T. Koretsune, J. Ibañez-Azpiroz, H. Lee, J.-M. Lihm, D. Marchand, A. Marrazzo, Y. Mokrousov, J. I. Mustafa, Y. Nohara, Y. Nomura, L. Paulatto, S. Poncé, T. Ponweiser, J. Qiao, F. Thöle, S. S. Tsirkin, M. Wierzbowska, N. Marzari, D. Vanderbilt, I. Souza, A. A. Mostofi, and J. R. Yates, “Wannier90 as a community code: new features and applications,” *Journal of Physics: Condensed Matter*, vol. 32, p. 165902, jan 2020.
- [17] J. Xin, Y. Tang, Y. Liu, X. Zhao, H. Pan, and T. Zhu, “Valleytronics in thermoelectric materials,” *npj Quantum Materials*, vol. 3, p. 9, Feb 2018.
- [18] J. E. Moore and L. Balents, “Topological invariants of time-reversal-invariant band structures,” *Phys. Rev. B*, vol. 75, p. 121306, Mar 2007.
- [19] R. Guehne and V. c. v. Chlan, “Exploring the nontrivial band edge in the bulk of the topological insulators Bi_2Se_3 and Bi_2Te_3 ,” *Phys. Rev. Res.*, vol. 6, p. 013214, Feb 2024.
- [20] D. Hsieh, Y. Xia, L. Wray, D. Qian, A. Pal, J. H. Dil, J. Osterwalder, F. Meier, G. Bihlmayer, C. L. Kane, Y. S. Hor, R. J. Cava, and M. Z. Hasan, “Observation of unconventional quantum spin textures in topological insulators,” *Science*, vol. 323, no. 5916, pp. 919–922, 2009.

Evolution of the Topological properties of Sb_2Te_3 and Sb_2Te under Uniaxial strain and Hydrostatic Pressure

3B.1 Introduction

In the previous chapter, we have established the non-trivial topological characters of the $(\text{Sb}_2\text{Te}_3)_m(\text{Sb}_2)_n$ homologous series. In this chapter, we turn our attention to understanding their evolution with the application of uniaxial strain and hydrostatic pressure. Many studies reveal how strain can tune the thermoelectric properties in various systems. For instance, the thermoelectric figure of merit is enhanced in $\text{Sb}_2\text{Te}_3/\text{Te}$ heterostructure under lattice strain^[1]. In addition to lowering the lattice thermal conductivity, this study had shown that the stress resulting from the

^{**} The work reported in this chapter is to be submitted soon for publication : A.G. Francis, R.K. Biswas, S.K. Pati.

uniaxial strain may lead the structure to a state near a topological phase transition, thereby increasing its zT . Another study on the strain effects on Sb_2Te_3 monolayer^[2] suggests that the thermoelectric performance is enhanced by the appearance of valley degeneracy and the tuning of the effective mass of the carriers. In addition to uniaxial strain, the tuning of the Hamiltonian under biaxial strain or hydrostatic pressure can also lead to a topological phase transition. The existing studies on such topological transitions induced by strain are also studied quite elaborately. However, the strain-dependent tuning of the topological properties of Sb_2Te_3 are not well studied. And there exists no reports on strain-dependent phase transitions in Sb_2Te . A detailed study of the effects of lattice tuning on the topological properties can offer us a better grasp on how the thermoelectric properties might change with strain or pressure.

In this chapter we try to systematically understand how uniaxial strain and hydrostatic pressure can affect the electronic band topology of Sb_2Te_3 and Sb_2Te . We observe a structural phase transition in Sb_2Te_3 bulk system with a uniaxial strain in the c -axis. While Sb_2Te do not undergo a structural transition with strain, its band structure and Fermi level evolves greatly with strain. However, the Fermi surface changes do not affect the parity of the eigenvalues, thereby showing no topological phase transition in system. We also have tried to understand the effect of pressure on these systems. In Sb_2Te_3 , with the application of pressure, the non-trivial topological nature vanishes and it becomes a normal insulator. However, in Sb_2Te , which we have found to be a strong topological insulator at zero pressure, undergoes a topological phase transition as pressure is applied. In fact, we find that with increase in applied pressure, the Sb_2Te transforms from a strong TI to a weak TI.

3B.2 Computational Methods

The first-principles simulations were performed using the Vienna Ab Initio Simulation Package (VASP)^[3,4]. The exchange correlation functional was approximated using

the Perdew-Burke-Ernzerhof (PBE)^[5] functional. The plane wave basis was truncated at an energy of 500 eV. A Γ -centred k point grid was used in all the calculations, with a grid size of $8 \times 8 \times 8$ for Sb_2Te_3 , $12 \times 12 \times 4$ for Sb_2Te . Strain and pressure was applied on the optimized structure obtained from ambient conditions, which are reported in Chapter 2.4. A uniaxial strain along the c -axis was applied to Sb_2Te_3 and Sb_2Te , after which the atomic positions were relaxed until the total energy change between two ionic steps was less than 10^{-6} . The systems were also subjected to pressure, where the system was optimised with respect to the enthalpy of the system, $H = E + PV$.

The band structure and the orbital projections on the band structure was calculated for a range of pressures and uniaxial strains for Sb_2Te_3 and Sb_2Te . For all the studied strains and pressure values, we have analysed the Z_2 invariant and the surface spectrum of the structures. First, the maximally localized wannier functions (MLWF) were obtained for each system using wannier90^[6] and a tight binding Hamiltonian was constructed. Using this tight binding parameters, a semi-infinite slab was constructed in WannierTools^[7]. The Z_2 invariant is then directly obtained by evaluating the change in the Hybrid Wannier Charge Centres (HWCC)_s^[8,9]. The surface spectrum and the surface Fermi surface were also obtained using WannierTools, where the surface states are given by the imaginary part of the surface Green's function, which is obtained using the iterative Green's function approach^[10,11].

3B.3 Results and Discussions

3B.3.1 Uniaxial Strain

A uniaxial strain is applied along the c -axis of Sb_2Te_3 and Sb_2Te . After the geometry optimization, we observe that the space group of Sb_2Te_3 changes from R-3m to C/2m, with 0.5 % compressive or tensile strain. However, the band structure retains the band inversion present at Γ . The evolution of band structure with strain in Sb_2Te_3

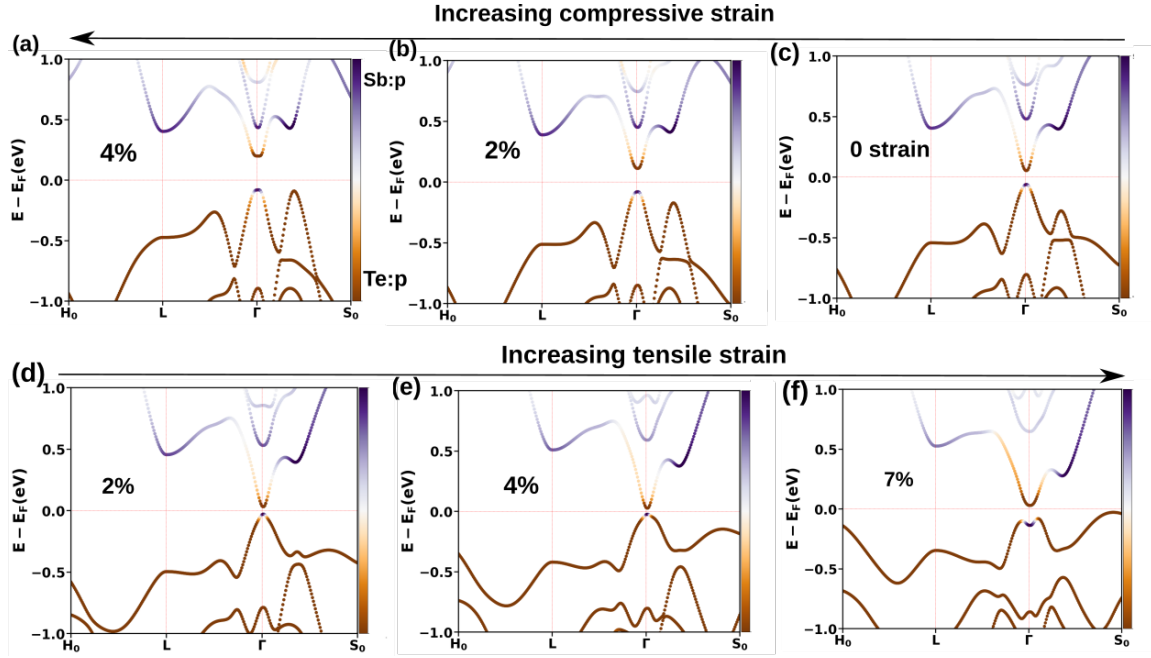


Figure 3B.1: The band structure of Sb_2Te_3 under uniaxial strain along the c -axis. The band structure at 0% strain is shown in (c). (a) corresponds to 4% compressive strain and (b) to 2% compressive strain. (d)-(f) shows the band evolution with tensile strain. It is clear that the band gap decreases with tensile strain and compressive strain leads to an increase in band gap at Γ

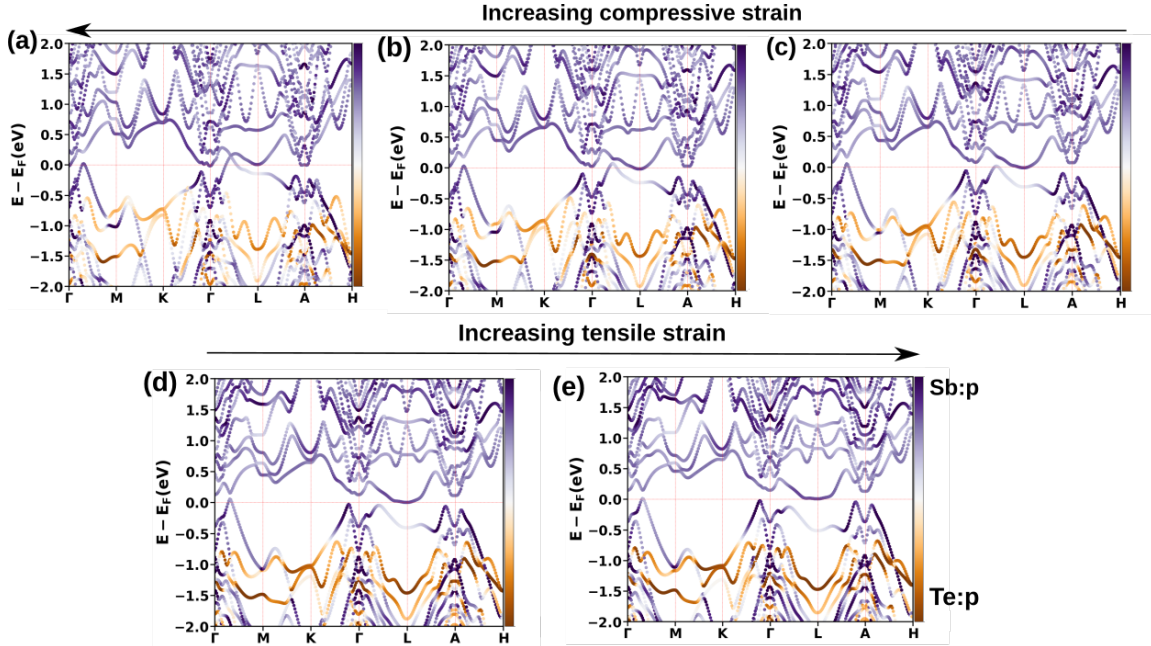


Figure 3B.2: (a) -(c) shows a decrease in the compressive strain in Sb_2Te_3 . (c) is the 0%-strain band structure. We see that the compressive strain do not lead to new band inversions or disappearance of old ones. (d) and (e) reports 2% and 4% tensile strain respectively. We see an additional band inversion appearing at the M -point suggesting a possible TQPT.

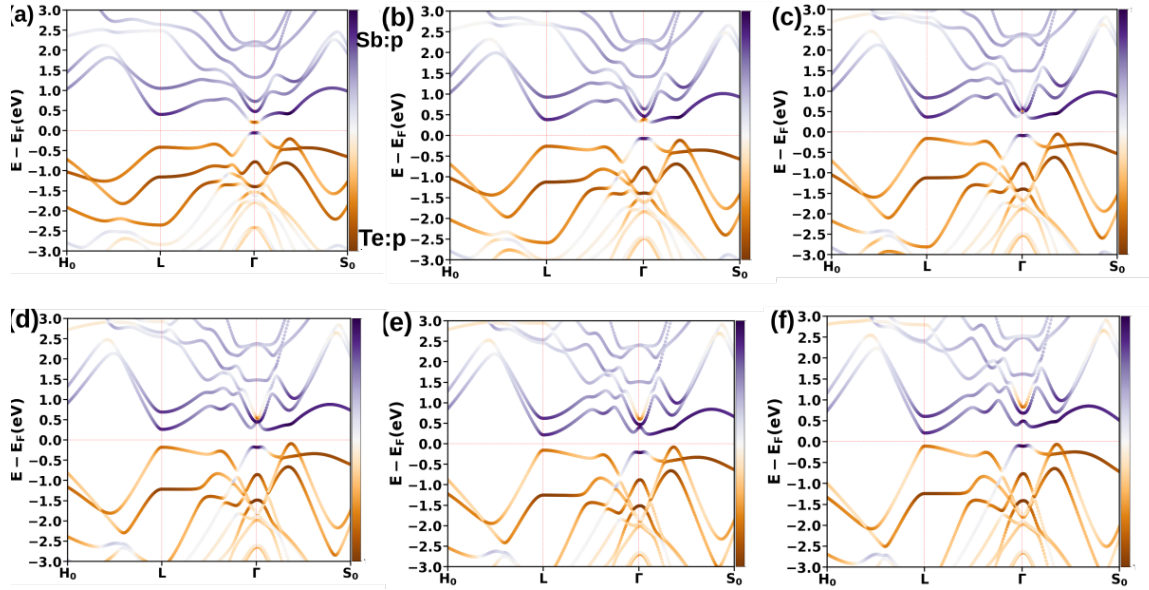


Figure 3B.3: The electronic band structure of Sb_2Te_3 under various pressures. (a)-(c) The band structure for 0.5 GPa, 2 GPa and 4 GPa pressure. The band structure remains similar, except the valley degeneracy increases as the pressure reaches 4 GPa. (d)-(f) shows the band structure at pressures 6 GPa, 8 GPa and 10 GPa. The band inversion at Γ , vanishes at pressures from 6 GPa and above. This leads to a trivial phase of Sb_2Te_3 at pressures above 6 GPa.

is given in Fig. 3B.1. We see that with compressive strain, see Fig. 3B.1(c) -(a), the band gap at Γ increases. This means that the possibility of a topological transition does not exist with compressive strain. However, with the increase in tensile strain, we see a decrease of the band gap at Γ , with an eventual parabolic band inversion arising at Γ . This kind of warping of the Fermi-surface is indicative of a larger SOC strength^[12]. Such a behaviour is seen in similar materials like Bi_2Te_3 ^[13,14]. This is also indicative of the coupling between the secondary bands and the band edges. However, the warping of the Fermi surface do not lead to a change in the calculated Z_2 invariant, thus suggesting no topological phase transition in Sb_2Te_3 , with uniaxial strain along the c -direction.

The change in band structure in Sb_2Te_3 under uniaxial strain along c is shown in Fig. 3B.2. The increase in compressive strain is shown on the top row, to the left, and we note that as the compressive strain increases, the number of band inversions remain the same as the band structure at 0 strain (Fig. 3B.2 (c)). There is a band crossing

behaviour between along $\Gamma - L$, at 4 % strain. Since this k-point is a non-TRIM point, it does not lead to a topological phase transition. With tensile strain, a band inversion occurs at the M -point, making the total number of band inversions even after 2 % tensile strain. However, our Z_2 invariant calculations do not show any change in the topological Z_2 invariant with the increase in strain. This means that there is no TQPT in Sb_2Te_3 as well, with uniaxial strain.

3B.3.2 Hydrostatic Pressure

Figure 3B.3 shows the band structure for 0.5 GPa, 2 GPa, 4 GPa, 6 GPa, 8 GPa and 10 GPa for Sb_2Te_3 . We see that as the pressure increases, the conduction band minima at Γ , lifts upward, with the higher conduction bands coming closer to this lowest conduction band. Beyond 6 GPa, however, the band inversion that existed at Γ , vanishes. To quantify the change, we explicitly calculated the Z_2 invariant of the system for the different pressures considered. We note that Sb_2Te_3 remains a strong TI, till 6 GPa, that is until the band inversion is present at Γ , beyond which the Z_2 changes to (0;000), indicating a trivial insulator. This means that with the application of pressure, the Sb_2Te_3 undergoes a topological quantum phase transition to a trivial insulator.

In the case of Sb_2Te , however, we observe quite a different band structure evolution with the application of pressure, which require further discussion. As the pressure increases, the band gap at the L -point decreases until 6 GPa. From 8 GPa, we see a reversal in the nature of the bands at L and at 10 GPa, we see a small band gap at L (see Fig. 3B.4). This band gap closing and opening, clearly is a signature of a topological transition. To understand if this indeed is the case, the Z_2 invariant was calculated and we see that there is a change in the invariant beyond 6 GPa. The invariant becomes (0;001) at 8 GPa. This corresponds to a weak topological insulator, with a topologically dark (001) surface. This means that all the planes other than (001) hosts an even number of Dirac cones, which can be removed pair-wise, making

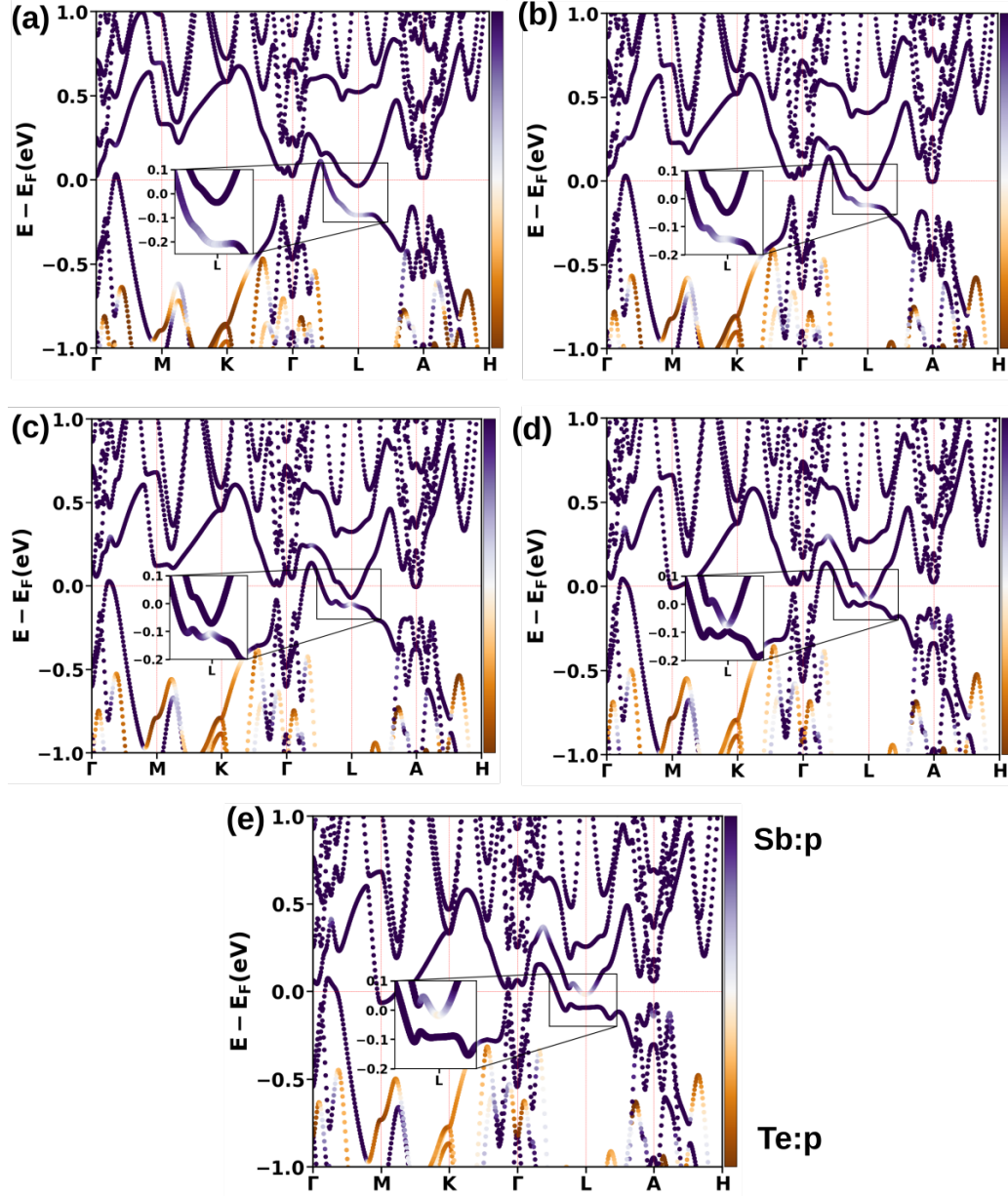


Figure 3B.4: (a) The band structure of Sb_2Te at 2 GPa. (b) -(e) represents the band structure for 4 GPa, 6 GPa, 8 GPa and 10 GPa. The valence band and conduction band at the L -point comes closer with the increase in pressure. For 8 GPa (d), we see a reversal of band characteristic at L .

it a weak TI.

3B.4 Conclusion and Discussions

We analysed the effect of uniaxial strain along the c -axis in Sb_2Te_3 , a well known strong topological insulator and a newly found strong topological insulator, Sb_2Te . We find that with the tensile and compressive strain, Sb_2Te_3 undergoes a structural transition to C2/m space group. Sb_2Te , though shows a change in the number of band inversions with the application of uniaxial strain, do not undergo a topological phase transition. This is because, the parity of the bands at the TRIM points do not change with the uniaxial strain. We also looked at the effect of hydrostatic pressure in both systems. A strong topological insulator to a trivial insulator topological phase transition is seen in Sb_2Te_3 between 6 GPa and 8 GPa, while in Sb_2Te , a topological quantum phase transition from strong topological insulator to a weak one is observed, with (001) surface as the dark surface. Our work provides a preliminary classification of the topological phases of Sb_2Te_3 and Sb_2Te under uniaxial strain and hydrostatic pressure. However, a further analysis of the structural transition in Sb_2Te_3 and a deeper analysis of the topological transitions in Sb_2Te are required to gain a better understanding. The phase transitions observed in Sb_2Te has to be verified experimentally and our work hints at the nature of transitions that can potentially occur in these two systems with lattice distortions.

Bibliography

- [1] Z. Wu, X. Chen, E. Mu, Y. Liu, Z. Che, C. Dun, F. Sun, X. Wang, Y. Zhang, and Z. Hu, "Lattice strain enhances thermoelectric properties in $\text{sb}_2\text{te}_3/\text{te}$ heterostructure," *Advanced Electronic Materials*, vol. 6, no. 1, p. 1900735, 2020.
- [2] Y. Ren, Y. Hu, Z. Hu, and L. Xue, "Influence of biaxial strain on the electronic

- and thermoelectric properties of sb2te3 monolayer,” *Materials Research Bulletin*, vol. 156, p. 111979, 2022.
- [3] G. Kresse and J. Furthmüller, “Efficient iterative schemes for ab initio total-energy calculations using a plane-wave basis set,” *Phys. Rev. B*, vol. 54, pp. 11169–11186, Oct 1996.
- [4] G. Kresse and J. Hafner, “Ab initio molecular dynamics for liquid metals,” *Phys. Rev. B*, vol. 47, pp. 558–561, Jan 1993.
- [5] J. P. Perdew, K. Burke, and M. Ernzerhof, “Generalized gradient approximation made simple,” *Phys. Rev. Lett.*, vol. 77, pp. 3865–3868, Oct 1996.
- [6] G. Pizzi, V. Vitale, R. Arita, S. Blügel, F. Freimuth, G. Géranton, M. Gibertini, D. Gresch, C. Johnson, T. Koretsune, J. Ibañez-Azpiroz, H. Lee, J.-M. Lihm, D. Marchand, A. Marrazzo, Y. Mokrousov, J. I. Mustafa, Y. Nohara, Y. Nomura, L. Paulatto, S. Poncé, T. Ponweiser, J. Qiao, F. Thöle, S. S. Tsirkin, M. Wierzbowska, N. Marzari, D. Vanderbilt, I. Souza, A. A. Mostofi, and J. R. Yates, “Wannier90 as a community code: new features and applications,” *Journal of Physics: Condensed Matter*, vol. 32, p. 165902, jan 2020.
- [7] Q. Wu, S. Zhang, H.-F. Song, M. Troyer, and A. A. Soluyanov, “Wanniertools: An open-source software package for novel topological materials,” *Computer Physics Communications*, vol. 224, pp. 405–416, 2018.
- [8] D. Gresch, G. Autès, O. V. Yazyev, M. Troyer, D. Vanderbilt, B. A. Bernevig, and A. A. Soluyanov, “Z2pack: Numerical implementation of hybrid Wannier centers for identifying topological materials,” *Phys. Rev. B*, vol. 95, p. 075146, Feb 2017.
- [9] A. A. Soluyanov and D. Vanderbilt, “Computing topological invariants without inversion symmetry,” *Phys. Rev. B*, vol. 83, p. 235401, Jun 2011.

-
- [10] F. Guinea, C. Tejedor, F. Flores, and E. Louis, “Effective two-dimensional hamiltonian at surfaces,” *Phys. Rev. B*, vol. 28, pp. 4397–4402, Oct 1983.
 - [11] M. P. L. Sancho, J. M. L. Sancho, and J. Rubio, “Quick iterative scheme for the calculation of transfer matrices: application to mo (100),” *Journal of Physics F: Metal Physics*, vol. 14, p. 1205, may 1984.
 - [12] M. P. L. Sancho, J. M. L. Sancho, and J. Rubio, “Quick iterative scheme for the calculation of transfer matrices: application to mo (100),” *Journal of Physics F: Metal Physics*, vol. 14, p. 1205, may 1984.
 - [13] J. P. Heremans, R. J. Cava, and N. Samarth, “Tetradymites as thermoelectrics and topological insulators,” *Nature Reviews Materials*, vol. 2, p. 17049, Sep 2017.
 - [14] I. T. Witting, T. C. Chasapis, F. Ricci, M. Peters, N. A. Heinz, G. Hautier, and G. J. Snyder, “The thermoelectric properties of bismuth telluride,” *Advanced Electronic Materials*, vol. 5, no. 6, p. 1800904, 2019.

Dynamic Magnetic Ground State in $\text{Yb}_2\text{Te}_5\text{O}_{13}$, a Dimer-based Compound

4.1 Introduction

Quantum Spin Liquids (QSLs) are extremely interesting and are at the forefront of research in condensed matter physics, because of their novel features. They defy a conventional kind of magnetic ordering, even as temperatures are lowered very close to 0 K. In addition they are also marked by fractional excitations and the emergence of a gauge field^[1–3]. The excitations in such a QSL phase are spinons, which are spin-1/2 particles with zero charge. These particles do not obey fermionic or bosonic statistics, but rather a fractional statistics. A QSL phase is much more than just the evasion of long range magnetic order. They, in fact, have a ground state which is long-range entangled. Observing such a state experimentally is quite

** The work reported in this chapter is to be submitted soon for publication : Rahul Kumar, Anita Gemmy Francis, Rhea Stewart, Peter J. Baker, Ralf Feyerherm, Devesh Chandra Binwal, Bella Lake, Swapan K Pati, A. Sundaresan

challenging. Though scientists worldwide are working on a large number of magnetic materials to find the signatures of a true quantum spin liquid, so far only “possible” candidates that hint at a QSL phase have been reported. The study of quantum spin liquids may thus answer a host of fundamental questions in physics, ranging from the nature of quantum entanglement^[4,5] and high-temperature superconductivity^[6], to the existence of fractionalized excitations^[7,8] and long range topological order^[9]. Apart from the rich physics, QSLs are very promising in regards to various material applications as well. For instance, the entangled ground state, which is robust against any local perturbation can be used in quantum information processing. Interestingly, a plethora of spin lattices, including the kagome^[11], hyperkagome^[12], triangular^[10], pyrochlore^[13], square lattices^[14] and dimer lattices with frustration^[15], were shown to realise quantum spin liquid states. Recently, frustrated rare-earth-based systems, particularly Yb³⁺ based, have been widely considered among the leading candidates for realizing novel quantum states. The presence of strong spin-orbit coupling (SOC) and crystalline electric field (CEF) causes such systems to have a spin with $J_{eff} = 1/2$. A combination of a low-dimensional frustrated magnetic lattice and J_{eff} or $S = 1/2$ ground state in high atomic number compounds proves to be an ideal platform for a quantum spin-liquid state.

In this chapter we look at a Yb³⁺ based oxide, Yb₂Te₅O₁₃, which shows experimental signatures of a QSL. We try to understand the phenomena from a combined First-principles and Monte-Carlo approach. Our investigations point to a spiral spin liquid state, with an incommensurate magnetic ordering at T= 0 K. This substantiates the experimentally observed lack of magnetic ordering seen in the system. A detailed explanation of the computational methods and results are given in the next section.

Table 4.1: The optimised lattice parameters.

$a(\text{\AA})$	$b(\text{\AA})$	$c(\text{\AA})$	α	β	γ
6.907	8.551	10.598	88.523	85.077	72.387

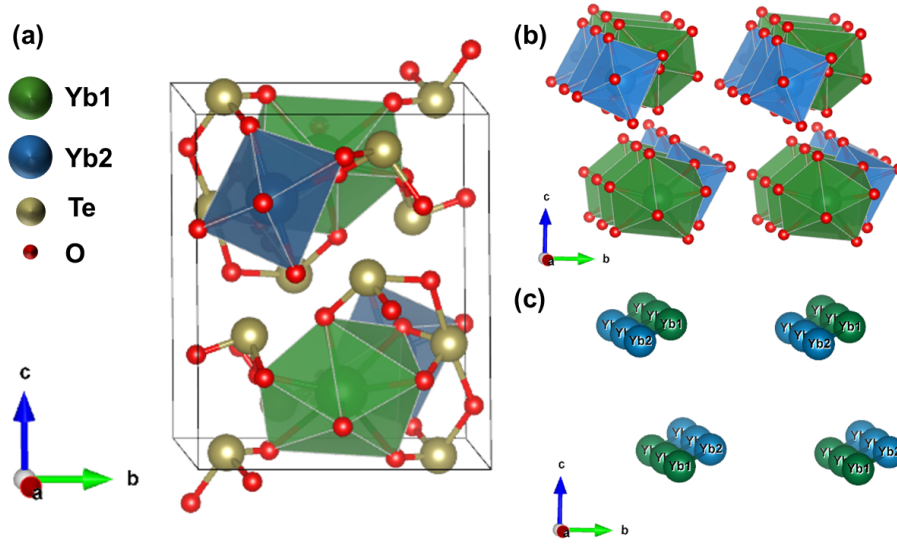


Figure 4.1: The crystal structure of $\text{Yb}_2\text{Te}_5\text{O}_{13}$. The green and blue polyhedra corresponds to the two Yb atoms having a different crystal environment. These atoms form dimers as shown in (b) and (c), along the c -direction. The dimers are stacked along the a -direction

4.2 Computational Methods

The first principles simulation was carried out on the periodic system using the Vienna Ab Initio Simulation Package (VASP)^[31–33], within the framework of the Projected Augmented Wave (PAW)^[34] method, utilizing the Perdew-Burke-Ernzerhof (PBE)^[35] approximation of the exchange-correlation functional. A plane wave basis set was used with an energy cutoff of 650 eV. The geometry of the experimentally observed structure is optimized until the forces on all the atoms are smaller than 0.03 eV/Å. To account for the self interaction error in the highly correlated f -electrons in the system, we have included a Hubbard correction of $U = 3$ eV^[36,37] for the optimization and the subsequent band structure and Density of States (DOS) calculations. The presence of heavy elements in the system gives rise to a large Spin-Orbit Coupling, which is included in all of our calculations. For the calculation of band structure and the Density of States (DOS), the Brillouin Zone integration was performed on a Γ -centered $7 \times 6 \times 5$ k-point grid. The number of kpoints to be used in the calculation was chosen by checking the ground state energy convergence with respect

to the k-point grid.

For the calculation of the magnetic exchange couplings were calculated from DFT and zero-field splitting parameters were obtained from a Complete Active Space SCF, as implemented in the ORCA package^[23]. The valence triple ζ basis set^[28] was employed for all atoms except Yb, for which a Segmented All Electron Relativistically Contracted (SARC) basis set, along with the SARC/J Coulomb fitting basis was implemented^[24,25]. The relativistic correction was applied by implementing the second-order Douglas-Kroll-Hess formalism. The nearest neighbor (J_1), next nearest neighbor (J_2), and the third nearest neighbor (J_3) magnetic exchange couplings were calculated by considering isolated nearest, next nearest, and third nearest Yb pairs and calculating the difference in energy of the high spin and broken symmetry states for each pair.

The ground state, ($T = 0$ K) state was probed using the iterative minimisation (IM) procedure^[52]. We consider a magnetic lattice of $N = 2 \times L \times L \times L$ spins, with periodic boundary conditions. The spins are treated as 3D vectors, with a magnitude of $|S| = 1$, with the real magnitude absorbed into the exchange couplings J_i . The spins are expressed in the spherical polar coordinates, and are free to orient in any direction. In the IM procedure, the spins are initially oriented in a random configuration. Each spin sees a local magnetic field because of its neighbours. We systematically choose each spin in the system and align it along its local magnetic field. The procedure was repeated until the energy change became less than 10^{-8} . This procedure was repeated for various linear system sizes L . For each L , we calculate the ordering vector by evaluating the equal time structure factor using the equation,

$$S_q = \langle s_q s_{-q} \rangle \quad (4.1)$$

where $s_q = \frac{1}{N} \sum_i S_i e^{-iq \cdot r_i}$. The ordering wave vector is then the q vector at which the equal time structure factor peaks.

The finite temperature properties of the magnetic system were explored using the

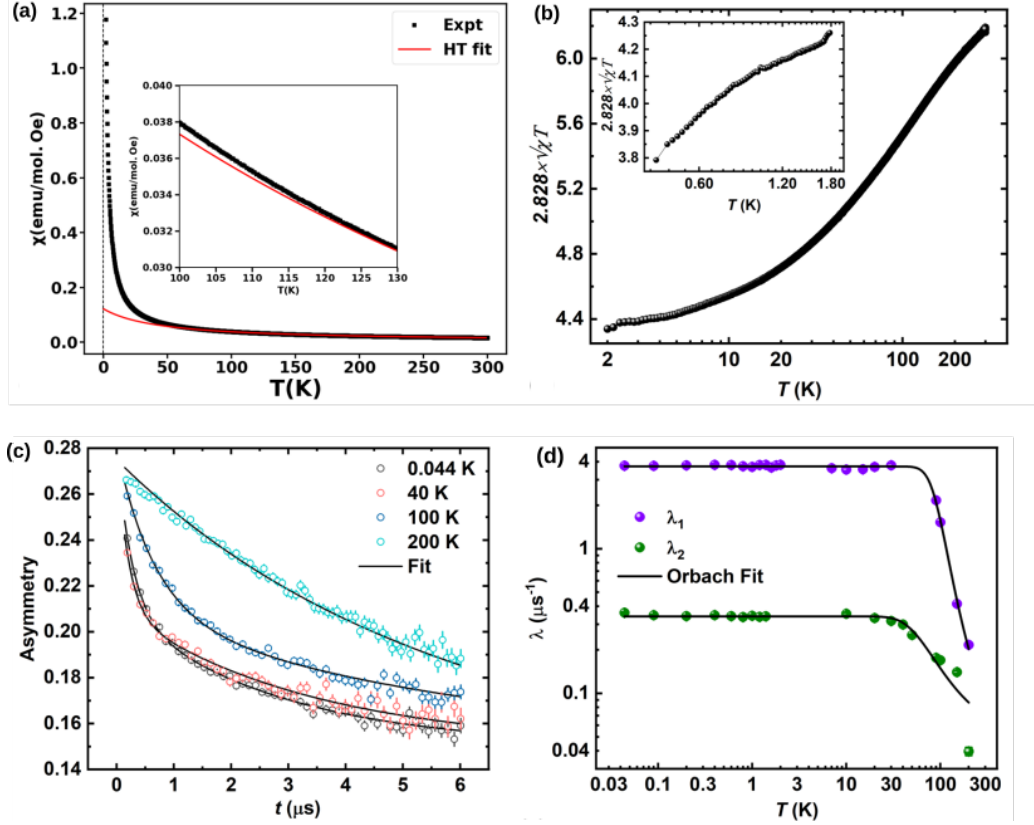


Figure 4.2: (a) The magnetic susceptibility with temperature. The Curie-Weiss linear fit, shown in red, corresponds to the behaviour of the system at high temperature paramagnetic region. The susceptibility deviates from the expected linear behaviour at around 125 K and at a lower temperature, around 45 K, the susceptibility turns upward sharply. (b) The variation of effective magnetic moment $\mu_{eff} = [(3k_B/N_A\mu_B^2)\chi T]^{1/2} \sim 2.828\sqrt{\chi T}$ with the temperature. The effective magnetic moment decreases as the temperature is lowered. (c) zero -field muon spin resonance measurements showing the a non-oscillatory behaviour in the depolarisation, suggesting the lack of a local static magnetic field. (d) The relaxation rate of the depolarization with temperature. As the temperature is lowered, the relaxation rates start increasing from around 200 K, until it plateaus below 10 K

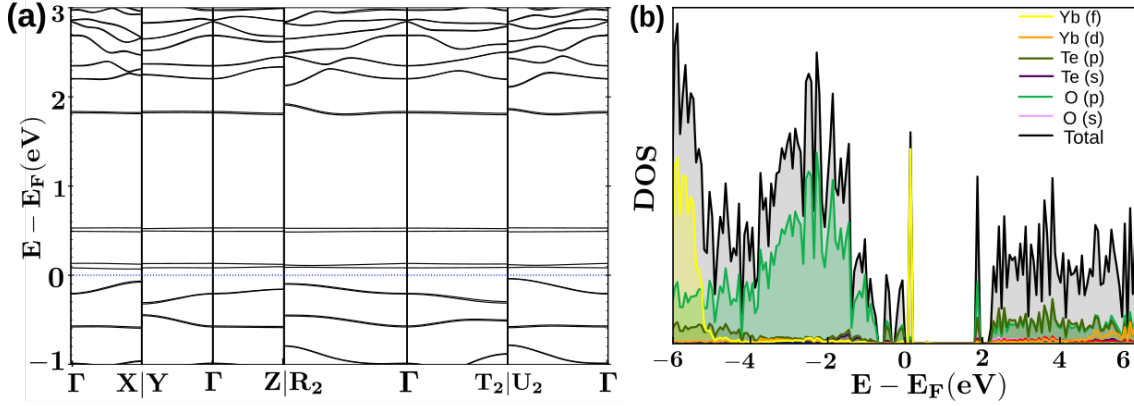


Figure 4.3: The band structure and the atom projected Density of States for $\text{Yb}_2\text{Te}_5\text{O}_{13}$. From b) it is clear that the bands in the gap are formed by the f orbitals of Yb with significant contribution of O p and Te p orbitals near the Fermi level.

Monte Carlo (MC) simulations, performed on a magnetic lattice of $N = 2 \times 10 \times 10 \times 10$ spins. In frustrated magnets, a Monte Carlo simulation using the Metropolis algorithm is inefficient because it leads to slow thermalization and displays long auto-correlation times. This slowing down becomes especially more prominent in the case of frustrated magnets, disordered systems, etc. Though many other algorithms like cluster update algorithms that are devised to tackle precisely such problems, their are not feasible in systems with Heisenberg spins^[31]. Hence, we resorted to a heat bath algorithm^[38] followed by over-relaxation^[53] in our simulations. The system was equilibrated for 5×10^6 MC steps, where each MC step consists of N heatbath steps, and a subsequent 10 over-relaxation steps. After thermalization, we performed 2×10^6 MC steps and the averaging was done taking the values at every 100 steps.

4.3 Results

The experiments on this system, including the magnetic susceptibility and specific heat with temperature show no magnetic transition in the system, for temperatures as low as 400 mK. The lack of such a transition is the first indication of a non-trivial magnetic state that the system has. To really get a grasp on the nature of

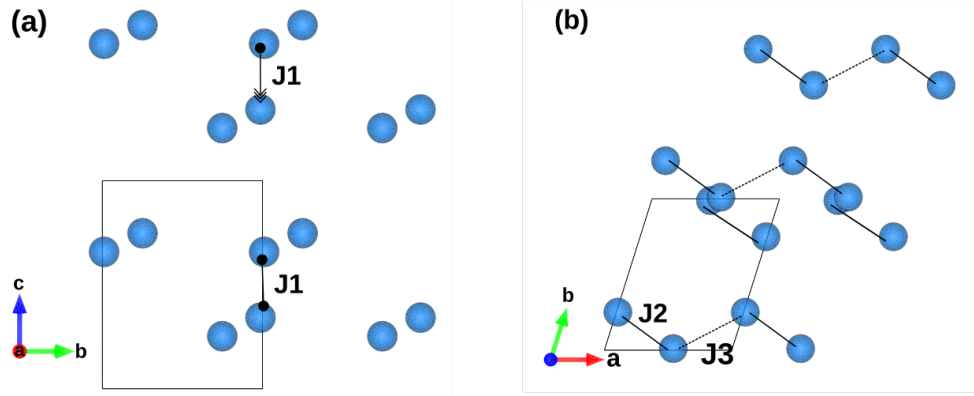


Figure 4.4: (a) The nearest neighbour pairs are aligned in the c -axis, with the exchange coupling represented by J_1 . (b) The second and third nearest neighbors lie in the $a - b$ plane and their exchange couplings are denoted as J_2 and J_3 respectively.

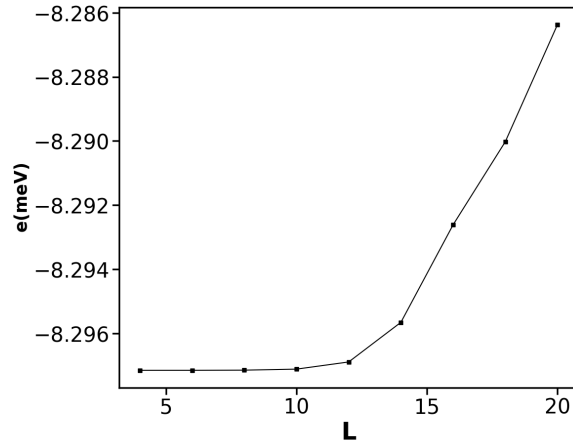


Figure 4.5: The energy per spin vs the linear system size L . The energy for the small L values remain almost the same after which it slowly increases.

magnetic field within the system the μ SR measurements were also performed. The polarization, do not show an oscillating behaviour. Instead it decays exponentially, hinting at the lack of a static magnetic field in the system. Moreover, there is no initial Asymmetry loss and a later recovery of the asymmetry to the $A_0/3$ -tail, thus ruling out a spin glass state. The relaxation rate in the system, moreover, becomes independent of temperature, below 30K, suggesting a dynamic magnetic ground state in the system. These experimental observations are summarized in Fig. 4.2. To understand the origin of this dynamic state, we resorted to a combined Density

J_1 (meV)	J_2 (meV)	J_3 (meV)	D (meV)	E (meV)
10.8	3.9	-7.3	-0.43	-0.009

Table 4.2: The nearest, next nearest, third nearest neighbor exchange couplings and the zero-field splitting parameters calculated from first principles calculations.

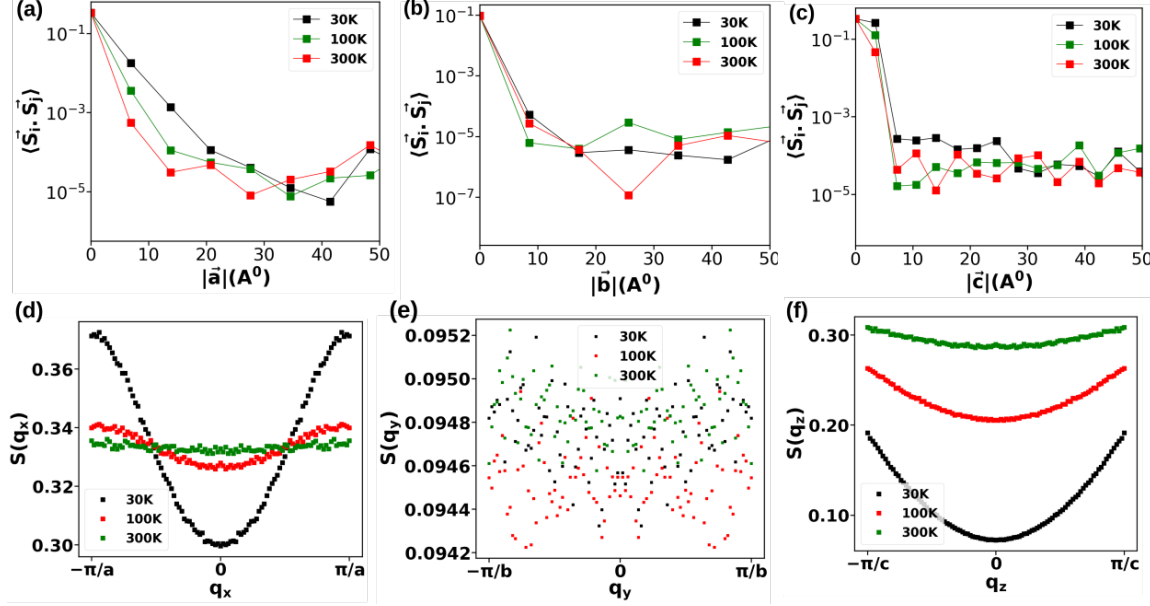


Figure 4.6: (a)-(c) The spin-spin correlation along the a , b and c axes respectively. Along each axis the spin correlations are plotted for three different temperatures- 30 K, 100 K and 300 K. (d)-(f) The equal time structure factor for q_x , q_y and q_z . The peak for $S(q_x)$ and $S(q_z)$ is at π/a and π/c respectively. $S(q-y)$ do not show any specific peak.

Functional Theory and Monte Carlo simulations approach. The lattice parameters obtained after geometry optimisation is given in Table 4.1. The lattice parameters agree well with the experimentally observed lattice constants, within the error bar of DFT. Using this optimised lattice, the band structure and the Density of States (DOS) is calculated, as reported in Fig. 4.3. The band structure reveals a large band gap of about 1.8 eV, with a small density of states in between this large gap, effectively decreasing the band gap to about 0.1 eV. Apart from this small contribution, the band gap matches well with the experimentally observed gap. A close look at the projected DOS as given in Fig 4.3(b) reveals that the f -orbitals of the magnetic Yb atoms, Te p -orbitals and the p -orbitals of O, are the major contributors to the bands near the Fermi level.

From the DFT calculations, we obtained the magnetic exchange interactions of the system. The first nearest neighbour exchange, J_1 , the second nearest neighbour interaction J_2 , the third nearest neighbour J_3 (visualized in Fig. 4.4) and the zero-field splitting parameters D and E are reported in Table 4.2. We observe that J_1 and J_2 are antiferromagnetic, while J_3 is ferromagnetic. An interesting fact to note is that the third nearest exchange is larger than the second nearest exchange. This suggests that the third nearest neighbours have a larger orbital overlap than the second nearest neighbours. The D and E parameters are very small and are negligible as compared to the exchange terms. Moreover, the implementation of heat-bath prohibits a Hamiltonian with anisotropy terms. Hence, we have modelled the system using an effective Heisenberg Hamiltonian, given by ,

$$H = J_1 \sum_{\langle ij \rangle} S_i \cdot S_j + J_2 \sum_{\langle\langle ij \rangle\rangle} S_i \cdot S_j + J_3 \sum_{\langle\langle\langle ij \rangle\rangle\rangle} S_i \cdot S_j \quad (4.2)$$

The ground state of the system was analyzed using the Iterative Minimization (IM) procedure. The energy per spin obtained for various system sizes L , is denoted in Fig. 5.4. The energy per spin remains similar upto fourth decimal point for $L = 4, 6, 8$ and 12. So, these systems are almost degenerate. However, examining the ordering vector obtained from the peak of the structure factor, as given in Table 4.3, we see that various system sizes lead to different ordering vector. The fact that the ordering vector depends on system size suggests that the exact ground state of the system cannot be reached by finite size simulations. This hints at the possibility of an incommensurate ground state magnetic order^[52]. The high temperature nature of the system was studied using Monte-Carlo simulations. The Monte Carlo simulation reproduces the Curie-Weiss temperature observed experimentally, which is $\theta_{CW} = -45$ K. The paramagnetic phase observed at room temperature remains unchanged down to 125 K, where we see a deviation from the Curie-Weiss law. We calculated the spin-spin correlation along the a -direction, b -direction and the c -direction by

Table 4.3: The ordering vector Q , in units of 2π , of the ground state, obtained from the peak of the equal time structure factor calculated using Iterative Minimisation (IM).

L	$Q(2\pi)$
4	$\frac{\pm 1}{2}, 0, \frac{\pm 1}{4}$
6	$\frac{\pm 1}{2}, 0, 0$
8	$\frac{\pm 1}{2}, \frac{\mp 1}{2}, \frac{\pm 3}{8}$
10	$\frac{\pm 1}{2}, \frac{\mp 3}{5}, \frac{\pm 3}{5}$
12	$\frac{\pm 1}{2}, \frac{\mp 1}{4}, \frac{\pm 5}{12}$
14	$\frac{\pm 1}{2}, \frac{\mp 5}{14}, \frac{\pm 1}{2}$
16	$\frac{\pm 1}{2}, \frac{\mp 5}{16}, \frac{\pm 1}{2}$
18	$\frac{\pm 1}{2}, \frac{\mp 5}{18}, \frac{\pm 4}{9}$
20	$\frac{\pm 1}{2}, \frac{\mp 7}{20}, \frac{\pm 7}{20}$

considering a linear system size of $L = 100$, along a , b and c axes respectively. The obtained spin-spin correlation is reported in Fig. 4.6. The spin-correlations along all three directions show an exponential decay, with the correlation length along the three axis being different. To gain a detailed understanding of the spin correlations, we analysed the static structure factor along the three directions, by calculating the Fourier transform of the spin correlations as given below,

$$S_{qi} = \frac{1}{N_i} \sum_{kj}^{N_i} \langle \vec{S}_k \cdot \vec{S}_j \rangle e^{i\vec{q}_i \cdot |\vec{r}_k - \vec{r}_j|_i} \quad (4.3)$$

Our observations are given in Fig. 4.6 (d) to (f). The structure factor along the a and the c axes peak at $q_x = \pi/a$ and $q_z = \pi/c$ respectively. This corresponds to an antiferromagnetic arrangement in the a and c axes. As the temperature is lowered

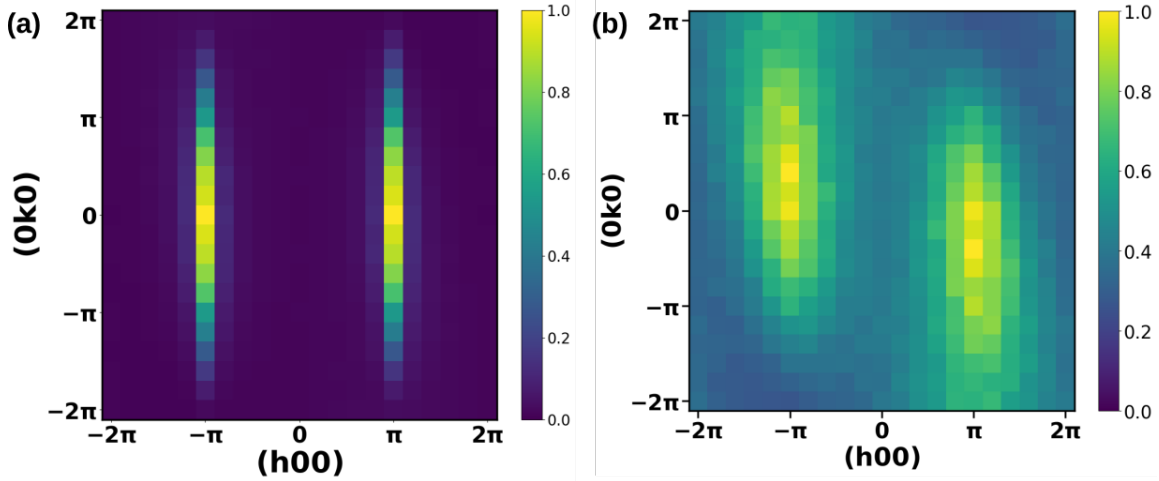


Figure 4.7: (a) The equal time structure factor at 10 K on the $(hk0)$ plane. This temperature is below the transition temperature observed in the simulations. (b) The structure factor at 50 K, which shows broad peaks near the boundary of the Brillouin zone. This corresponds to a spiral ordering in the system, which arises because of the thermal fluctuations acting on the classical spins

the intensity of the structure factor peak increases for both the axes. However, the b -direction do not show any particular peak, indicating a lack of ordering along b . The competition of the exchange interactions in the a - b plane leads to a lack of ordering in this system in the a - b plane. The spin structure factor $S(q_z)$ vs. q_z , shown in Fig. 4.6(f), peaks at $|q_z| = \frac{\pi}{c}$, confirming antiferromagnetic interactions along the c -axis. However, below 125 K, J_2 and J_3 , which act in the $a - b$ plane play a bigger role. These in fact, make the system much more interesting. We also looked at the equal time structure factor for the system with dimension $L \times L \times L$, with $L = 10$. The intensity analysis of the static spin structure factor at various temperatures in the high-temperature region gives us an idea about the dominant interactions and the origin of frustration in the system. It was calculated as follows:

$$S_q = \frac{1}{N} \sum_{ij}^N \langle \vec{S}_i \cdot \vec{S}_j \rangle e^{i\vec{q} \cdot (\vec{r}_i - \vec{r}_j)} \quad (4.4)$$

where N is the total number of spins in the three-dimensional simulation box. The static structure factor, in the $a - b$ plane, shows diffusive peaks in the first Brillouin

zone for $T = 50\text{K}$, as plotted in Fig. 4.7 (b). This phase is best described as a spiral non-trivial phase, where the spins fluctuate as spirals with some effective angles^[32–34], which exists down to a temperature close to where the susceptibility starts rising, around 45 K. Hence, our computational studies confirm that these competing magnetic interactions are the primary inducers of the interacting dimer based phase in $\text{Yb}_2\text{Te}_5\text{O}_{13}$ for temperature range from 125 K to the T value where the susceptibility starts rising as the T decreases. Interestingly, the low temperature phase is governed by the ferromagnetic exchange interaction, J_3 , in the $a - b$ plane which gains prominence at low temperature and solely governs the low temperature magnetic phase.

4.4 Conclusion

In conclusion, we studied the magnetic phase in a dimer-based material $\text{Yb}_2\text{Te}_5\text{O}_{13}$ from first principles analysis and Monte Carlo simulations. Our study reveals that absence of both magnetic long range order and local static magnetic field in the system, observed experimentally, is due to the competing exchange interactions in the $a - b$ plane of the system. The first nearest exchange, which is antiferromagnetic is significant at the high temperature paramagnetic region. As the temperature starts deviating from the Curie-Weiss law, we see that the second and third nearest neighbour exchange interactions, the former being antiferromagnetic and the latter ferromagnetic, lying in the $a - b$ plane becomes more prominent. Our classical Monte Carlo simulations reveal a spiral spin liquid region in the system and an incommensurate ground state, indicating definitive signals of a QSL phase in $\text{Yb}_2\text{Te}_5\text{O}_{13}$, if quantum fluctuations are included.

Bibliography

- [1] L. Balents, Spin liquids in frustrated magnets, *Nature (London)* **464**, 199 (2010).
- [2] R. Moessner and A. P. Ramirez, Geometrical frustration, *Phys. Today* **59**, 24 (2006).
- [3] B. Normand, Frontiers in frustrated magnetism, *Contemp. Phys.* **50**, 533 (2009).
- [4] S. V. Isakov, M. B. Hastings, and R. G. Melko, Topological entanglement entropy of a Bose–Hubbard spin liquid, *Nat. Phys.* **7**, 772 (2011).
- [5] X.-G. Wen, Quantum orders and symmetric spin liquids, *Phys. Rev. B* **65**, 165113 (2002).
- [6] B. Keimer, S. A. Kivelson, M. R. Norman, S. Uchida, and J. Zaanen, From quantum matter to high-temperature superconductivity in copper oxides, *Nature (London)* **518**, 179 (2015).
- [7] M. J. P. Gingras and P. A. McClarty, Quantum spin ice: a search for gapless quantum spin liquids in pyrochlore magnets, *Rep. Prog. Phys.* **77**, 056501 (2014).
- [8] R. Moessner and S. L. Sondhi, Irrational charge from topological order, *Phys. Rev. Lett.* **105**, 166401 (2010).

-
- [9] N. Y. Yao, C. R. Laumann, A. V. Gorshkov, H. Weimer, L. Jiang, J. I. Cirac, P. Zoller, and M. D. Lukin, Topologically protected quantum state transfer in a chiral spin liquid, *Nat. Commun.* **4**, 1585 (2013).
- [10] H. D. Zhou, E. S. Choi, G. Li, L. Balicas, C. R. Wiebe, Y. Qiu, J. R. D. Copley, and J. S. Gardner, Spin liquid state in the $S=1/2$ triangular lattice $\text{Ba}_3\text{CuSb}_2\text{O}_9$, *Phys. Rev. Lett.* **106**, 147204 (2011).
- [11] M. Fu, T. Imai, T.-H. Han, and Y. S. Lee, Evidence for a gapped spin-liquid ground state in a kagome Heisenberg antiferromagnet, *Science* **350**, 655 (2015).
- [12] P. Khuntia, F. Bert, P. Mendels, B. Koteswararao, A. V. Mahajan, M. Baenitz, F. C. Chou, C. Baines, A. Amato, and Y. Furukawa, Spin liquid state in the 3D frustrated antiferromagnet $\text{PbCuTe}_2\text{O}_6$: NMR and muon spin relaxation studies, *Phys. Rev. Lett.* **116**, 107203 (2016).
- [13] K. A. Ross, L. Savary, B. D. Gaulin, and L. Balents, Quantum excitations in quantum spin ice, *Phys. Rev. X* **1**, 021002 (2011).
- [14] O. Mustonen, S. Vasala, E. Sadrollahi, K. P. Schmidt, C. Baines, H. C. Walker, I. Terasaki, F. J. Litterst, E. Baggio-Saitovitch, and M. Karppinen, Spin-liquid-like state in a spin-1/2 square-lattice antiferromagnet perovskite induced by $d^{10}-d^0$ cation mixing, *Nat. comm.* **9**, 1 (2018).
- [15] I. Terasaki, T. Igarashi, T. Nagai, K. Tanabe, H. Taniguchi, T. Matsushita, N. Wada, A. Takata, T. Kida, M. Hagiwara, K. Kobayashi, H. Sagayama, R. Kumai, H. Nakao, and Y. Murakami, Absence of magnetic long range order in $\text{Ba}_3\text{ZnRu}_2\text{O}_9$: a spin-liquid candidate in the $S=3/2$ dimer lattice, *J. Phys. Soc. Jpn.* **86**, 033702 (2017).
- [16] G. Kresse and J. Furthmüller, Efficient Iterative Schemes for Ab Initio Total-Energy Calculations Using a Plane-Wave Basis Set, *Phys. Rev. B* **54**, 11169 (1996).

-
- [17] G. Kresse and J. Furthmüller, Efficiency of Ab-Initio Total Energy Calculations for Metals and Semiconductors Using a Plane-Wave Basis Set, *Comput. Mater. Sci.* **6**, 15 (1996).
- [18] G. Kresse and J. Hafner, Ab Initio Molecular Dynamics for Liquid Metals, *Phys. Rev. B* **47**, 558 (1993).
- [19] G. Kresse and D. Joubert, From Ultrasoft Pseudopotentials to the Projector Augmented-Wave Method, *Phys. Rev. B* **59**, 1758 (1999).
- [20] J. P. Perdew, K. Burke, and M. Ernzerhof, Generalized Gradient Approximation Made Simple, *Phys. Rev. Lett.* **77**, 3865 (1996).
- [21] Y. Chornodolskyy, V. Karnaushenko, J. Selech, V. Vistovsky, T. Demkiv, K. Przystupa, S. Syrotyuk and A. Voloshinovskii, Computer Modelling of Energy Structure of Yb^{3+} and Lu^{3+} Doped LaF_3 Crystals, *Materials*, **15**, 7937 (2022).
- [22] Y. Lu, J. Wang, J. Li, J. Wu, S. Kanno, T. Tada and H. Hosono, Realization of Mott-insulating electrides in dimorphic Yb_5Sb_3 , *Phys. Rev. B.* **98**, 125128 (2018).
- [23] F. Neese, F. Wennmohs, U. Becker, and C. Riplinger, The ORCA quantum chemistry program package, *J. Chem. Phys.* **152**, 224108 (2020).
- [24] D. Aravena, F. Neese, and D. A. Pantazis, Improved Segmented All-Electron Relativistically Contracted Basis Sets for the Lanthanides, *J. Chem. Theory Comput.* **12**, 3, 1148–1156 (2016).
- [25] D.A. Pantazis, F. Neese, All-Electron Scalar Relativistic Basis Sets for the Lanthanides, *J. Chem. Theory Comput.* **5**, 9, 2229–2238 (2009).
- [26] Anna Fancelli, Johannes Reuther and Bella Lake, Classical spin models of the windmill lattice and their relevance for $\text{PbCuTe}_2\text{O}_6$, *Phys.Rev.B* **108**, 184415 (2023).

-
- [27] Sophia R. Sklan and Christopher L. Henley, Nonplanar ground states of frustrated antiferromagnets on an octahedral lattice, *Phys. Rev. B* **88**, 024407 (2013).
- [28] F. Weigend and R. Ahlrichs, Balanced basis sets of split valence, triple zeta valence and quadruple zeta valence quality for H to Rn: Design and assessment of accuracy, *Phys. Chem. Chem. Phys.*, **7**, 3297-3305 (2005).
- [29] Y. Miyatake, M. Yamamoto, J. J. Kim, M. Toyonaga and O. Nagai, On the implementation of the 'heat bath' algorithms for Monte Carlo simulations of classical Heisenberg spin systems, *J. Phys. C: Solid State Physics*, **19**, 2539 (1986).
- [30] Michael Creutz, Overrelaxation and Monte Carlo simulation, *Phys. Rev. D*, **36**, 515 (1987).
- [31] Yang-Zhi Chou, Zhentao Wang, and Sankar Das Sarma, Monte Carlo solver and renormalization of Migdal-Eliashberg spin chain, *Phys. Rev. B*, **109**, 054514 (2024).
- [32] D. Bergman, J. Alicea, E. Gull, S. Trebst, and L. Balents, Order-by-disorder and spiral spin-liquid in frustrated diamond-lattice antiferromagnets, *Nature Physics*, **3**, 487–491 (2007).
- [33] S. Gao, O. Zaharko, V. Tsurkan, Y. Su, J. S. White, G. S. Tucker, B. Roessli, F. Bourdarot, R. Sibille, D. Chernyshov, T. Fennell, A. Loidl, and C. Rüegg, Spiral spin-liquid and the emergence of a vortex-like state in MnSc_2S_4 *Nature Physics*, **13**, 157–161 (2017).
- [34] J. N. Graham, N. Qureshi, C. Ritter, P. Manuel, A. R. Wildes and L. Clark, Experimental Evidence for the Spiral Spin Liquid in LiYbO_2 , *Phys. Rev. Lett.* **130**, 166703 (2023).

NaYbW₂O₈ : A Possible Quantum Spin Liquid in a Hyperhoneycomb Lattice

5.1 Introduction

Quantum magnetism is as old as quantum mechanics and spin is an integral part of electron along with charge. In the field of quantum magnetism, frustration is referred to the conflicting exchange interactions, where all interactions cannot be satisfied simultaneously. Such behavior leads to a host of new states of matter with exotic properties. One of the most notable outcomes of such frustration is the quantum spin liquid (QSL) state, in which quantum fluctuations keep the spins disordered down to 0 K^[1]. The resulting QSL states are of different types, ranging from chiral spin liquids^[2,3] to Z_2 topological spin liquids^[4–6], which feature fractional excitations. One would expect a spin flip to give rise to an integer change, leading to integer excitations.

^{**} The work reported in this chapter is submitted for publication : Rahul Kumar, Anita Gemmy Francis, Rhea Stewart, Peter J. Baker, Swapan K Pati, A. Sundaresan

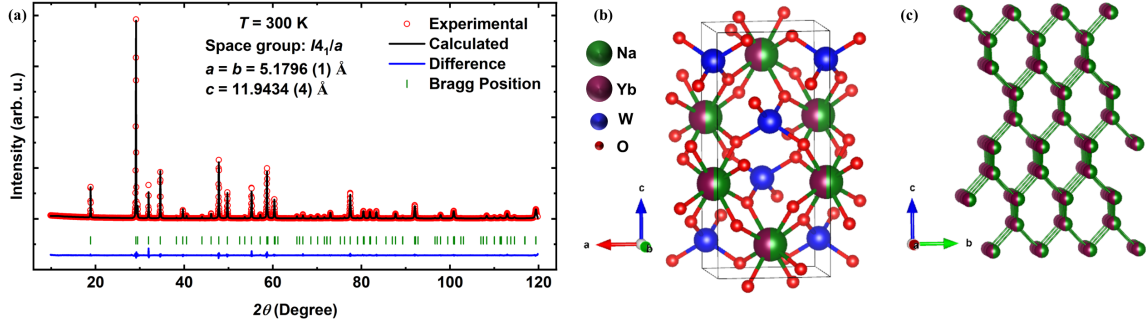


Figure 5.1: (a) The observed and refined powder x-ray diffraction pattern of NaYbW_2O_8 . The green lines mark the Bragg positions. The difference between experimental and calculated intensities is given in blue. (b) The lattice structure of NaYbW_2O_8 , as viewed along the b -axis. (c) The magnetic lattice, with 50% disorder between the Yb and Na atoms. This lattice forms a hyperhoneycomb structure.

A QSL shows a deviation from this expected behaviour, making their experimental detection difficult.

There have been extensive experimental and theoretical research on QSLs in two and quasi-two dimensional (2D and quasi-2D) systems^[1–9]. However, understanding these states in their three-dimensional (3D) counterparts is still largely an uncharted territory. It is well known that in the 3D systems, the long-range ordered magnetic states are quite natural, making the disordering effect of quantum fluctuations seems less significant. This area remains unexplored due to the limitations of theoretical and numerical approaches in 3D, as well as the scarcity of suitable materials^[10].

The frustration, which leads to the extensive ground state degeneracy in classical magnets in a magnetic lattice need not always be a result of geometry. Frustration and degeneracy can come about from competing exchange interactions as well. Additionally, in some rare-earth ions based on quantum magnets, the large spin-orbit coupling introduces anisotropic magnetic interactions that can create quantum-disordered ground states even without the typical geometric frustration. A notable example is the honeycomb lattice, a bipartite structure where both ferromagnetic and antiferromagnetic Heisenberg couplings result in ordered ground states. Yet, a unique set of anisotropic interactions proposed by Kitaev^[11], in which neighboring spins are

linked by Ising interactions along axes determined by the bond's spatial orientation, has been found to exist in a quantum spin liquid phase. If one can experimentally realize such a system in 3D, it may be a potential 3D quantum spin liquid^[12]. However, due to the difficulty in realizing 3D variants of the honeycomb lattice, material explorations have been limited to 2D layered honeycomb structure^[13–22], except a few 3D iridates^[23,24]. In this chapter, we report a Yb-based hyperhoneycomb lattice compound, NaYbW₂O₈, which crystallizes into a scheelite structure. It has inherently 50% site disorder among Na⁺ and Yb³⁺ ions. Intriguingly, it has been proposed that inherent disorder in certain frustrated magnets can result in a random exchange between spins^[25–30], and hence can lead to various exotic quantum phases. Despite the absence of magnetic ordering down to 0.4 K, the heat capacity measurements unveil an internal magnetic field of the order of 0.6 K. Further investigation using muon spin relaxation (μ SR) measurements indicate a dynamic magnetic state below 20 K. Hence, a combination of 3D spin-lattice, $J_{eff} = 1/2$ ground state, chemical disorder, and dynamical magnetic state can lead to a randomness-driven spin-liquid-like ground state. We use Density Functional Theory and Monte Carlo simulations to understand the microscopic origin of frustration in this system. Our structural analysis confirms two possible magnetic lattices possible in the system, one which harbors geometric frustration and the other which shows competing exchange interactions. Both the structures show broad diffused equal time structure factor, indicating a spin liquid phase, thus complementing the experiments.

5.2 Computational Methods

The magnetic properties of NaYbW₂O₈ were explored in detail employing combined Density Functional Theory (DFT) and Monte Carlo Simulations. The density functional theory calculations were carried out using the Vienna Ab-Initio Simulation Package (VASP)^[31–33]. A pseudopotential based on the Projector-Augmented-Wave

(PAW)^[34] method is used with the exchange-correlation functional approximated using the Perdew-Burke-Ernzerhof (PBE) functional^[35]. A Γ -centered $4 \times 4 \times 2$ k-point grid was used for all the calculations. An on-site Hubbard U of 3 eV was assigned to the Yb $4f$ orbitals to take into account their strong correlations^[36,37].

The presence of intrinsic substitutional disorder gives rise to six possible unit cells with different Na and Yb atomic coordinates. These structures lead to two different magnetic Yb lattices. We considered one unit cell from each kind of lattice, whose geometries were optimized until the energy between two consecutive ionic steps became less than 10^{-5} eV. The optimized structures were used to calculate the exchange interactions. To calculate the exchange couplings, various collinear magnetic configurations are considered, and their energies are mapped to the $J_1 - J_2$ Heisenberg model,

$$H = J_1 \sum_{\langle ij \rangle} \vec{S}_i \cdot \vec{S}_j + J_2 \sum_{\langle\langle ij \rangle\rangle} \vec{S}_i \cdot \vec{S}_j \quad (5.1)$$

where, $\langle .. \rangle$ corresponds to the nearest neighbour pairs, $\langle\langle .. \rangle\rangle$ corresponds to the next nearest neighbour pairs and J_1 and J_2 are the nearest and next nearest neighbor interactions respectively. The spins S_i are considered to be three-dimensional vectors in the spherical polar coordinates with $|S_i| = 1/2$. For this energy mapping analysis, we considered a $1 \times 1 \times 2$ supercell for the first lattice and a $2 \times 1 \times 1$ supercell for the second lattice. The supercells have four magnetic Yb atoms each and we considered three different spin configurations for the mapping analysis - one ferromagnetic (FM), and two antiferromagnetic (AFM_1 and AFM_2). AFM_1 has an up-up-down-down configuration and AFM_2 , an up-down-up-down configuration. Then the ground state DFT energies for the first lattice can be written as

$$\begin{aligned} E_{FM} &= E_0 + J_1 + 3 J_2 \\ E_{AFM_1} &= E_0 - J_1 + 3 J_2 \\ E_{AFM_2} &= E_0 + J_2 \end{aligned} \quad (5.2)$$

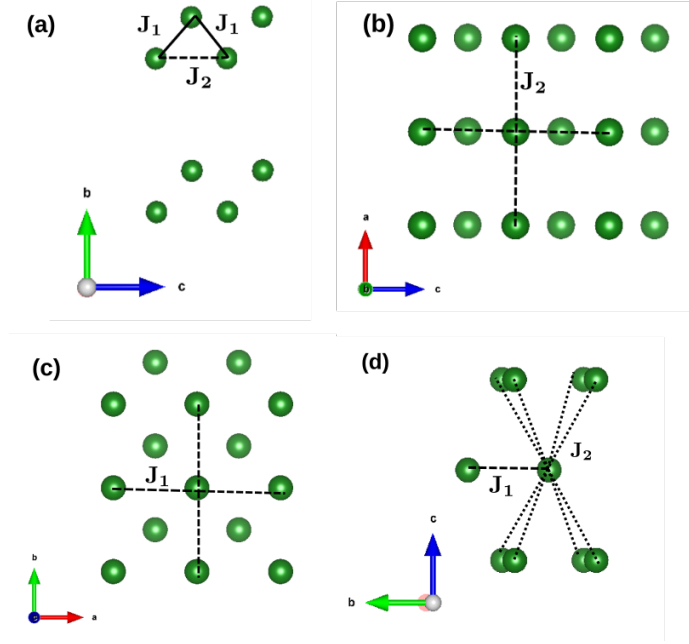


Figure 5.2: (a) and (b) shows a schematic representation of the nearest and next nearest neighbors in lattice A. (c) and (d) The nearest and next nearest pairs in lattice B. It is clear that lattice A is geometrically frustrated and that such geometric frustration is absent in lattice B. Lattice A has two nearest neighbors and four next nearest neighbors as compared to lattice B, which has four nearest neighbors and eight next nearest neighbors.

and for the second lattice, these three configurations yield the following set of equations,

$$\begin{aligned}
 E_{FM} &= E_0 + 3 J_1 + 4 J_2 \\
 E_{AFM_1} &= E_0 + 3 J_1 - 4 J_2 \\
 E_{AFM_2} &= E_0 + J_1
 \end{aligned} \tag{5.3}$$

where, E_0 is the DFT energy without the spin consideration.

The J_1 and J_2 values were obtained by solving the above system of equations and were used to simulate the magnetic properties at the zero temperature as well as the finite temperature for lattices A and B. The ground state properties were obtained by an Iterative Minimization (IM) procedure^[52,54]. The procedure is repeated for various linear system sizes L , each having $N = 2 \times L \times L \times L$ spins. The ordering vector Q , for a given L is obtained from the peak of the equal time structure factor, which is

the Fourier Transform of the spin-spin correlation function and can be calculated as:

$$S_Q = \frac{1}{N} \sum_{ij} \langle \vec{S}_i \cdot \vec{S}_j \rangle e^{iQ \cdot r_{ij}} = \langle s_Q \cdot s_{-Q} \rangle \quad (5.4)$$

where $\langle s_Q \rangle = \frac{1}{N} \sum_i \vec{S}_i e^{iQ \cdot r_i}$. To understand the finite temperature behavior of the system, we resorted to Monte Carlo simulations, implementing the heat-bath algorithm^[38] coupled with an over-relaxation algorithm^[53]. The simulations were carried out for a system size of $L = 16$ and $L = 10$. Each Monte Carlo (MC) step comprises of $2 \times L \times L \times L$ heat-bath steps followed by ten over-relaxation steps. After a thermalization of 10^6 MC steps, the thermodynamic properties were calculated by performing 5×10^6 MC steps.

5.3 Results

The presence of inherent disorder in the lattice leads to various lattice structures as the Na and Yb can be present at the same lattice site, thereby giving rise to many lattice realisations. To accurately simulate the experimental observations, which are summarised in Fig. 5.3, we first optimised all the possible lattice configurations. There are two Yb atoms and two Na atoms in the unit cell, which gives rise to $4C_2$ possible lattice configurations. Out of these six possible structures, four correspond to a particular magnetic lattice (lattice A) and the other two to another magnetic lattice (lattice B), see figure 5.2 depicting the nearest and the next-nearest pairs in the two lattices. The former has a nearest neighbor distance of 3.96 \AA , while the latter has a nearest neighbor distance of 5.17 \AA and has a lower free energy as compared to the former. We have calculated the nearest neighbour and the next nearest neighbour exchange parameters, J_1 and J_2 respectively, for both the structures by mapping the DFT energies to Heisenberg Hamiltonian. The obtained values for J_1 and J_2 are tabulated in table 5.1. In addition, we also calculated the zero-field splitting

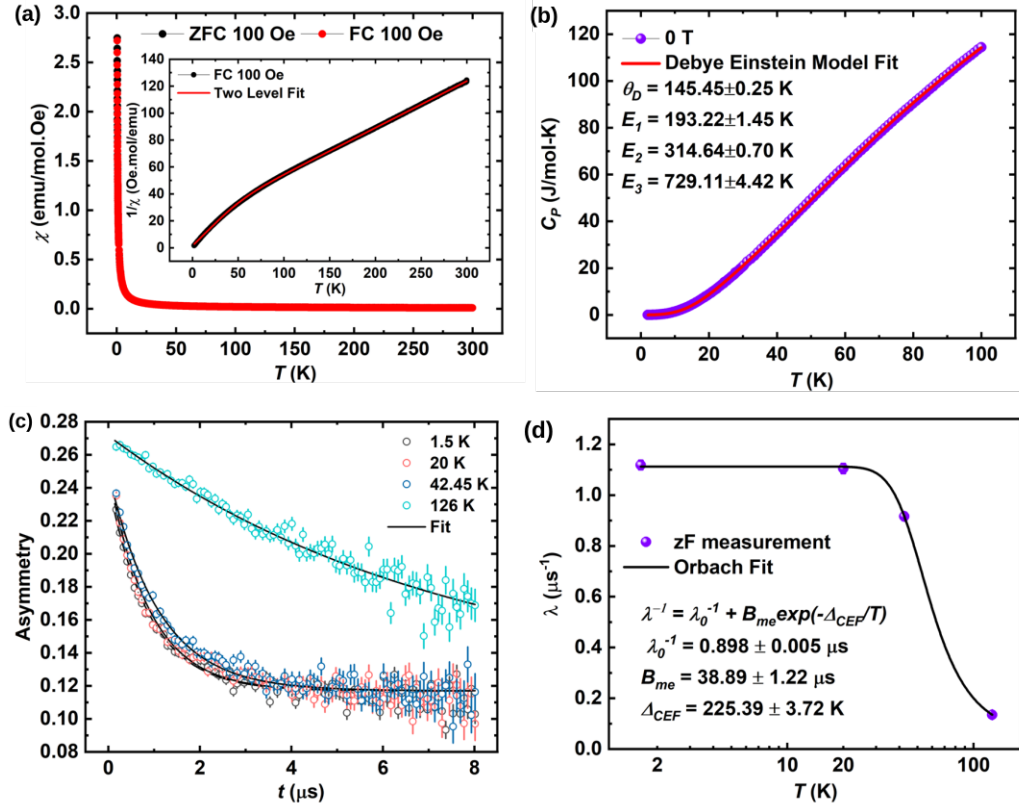


Figure 5.3: (a) The magnetic susceptibility vs temperature down to a temperature of 400 mK, under Zero Field cooled and Field cooled protocols. Two level Curie-Weiss model fit to the inverse susceptibility data is given in the inset. (b) Measured heat capacity in a temperature range 2 K to 100 K, in the absence of magnetic field. (c) The μ SR measurements showing the depolarisation with temperature. The depolarisation shows an exponential decay. (d) The variation of the corresponding fitting parameter, λ with temperature.

parameters, which are of the order of 10^{-4} and 10^{-6} respectively.

The nearest neighbour exchange is ferromagnetic, while the next nearest exchange is antiferromagnetic and almost half the nearest neighbour exchange in both the lattices. However, we see that in lattice B, the exchange interactions are one order less than the case of lattice A. This is because of the fact that the magnetic ions in lattice B are much more further apart than in the case of lattice A. We note that the values of D and E are much smaller in magnitude and we neglect those while probing the properties further. In fact, the system was modelled using the $J_1 - J_2$

Table 5.1: The nearest, next nearest exchange couplings from first principles calculations for lattice A and lattice B

Lattice	J_1 (meV)	J_2 (meV)
A	-2.8	1.2
B	-0.08	0.04

Heisenberg Hamiltonian given by,

$$H = J_1 \sum_{\langle ij \rangle} \vec{S}_i \cdot \vec{S}_j + J_2 \sum_{\langle\langle ij \rangle\rangle} \vec{S}_i \cdot \vec{S}_j \quad (5.5)$$

where, $\langle .. \rangle$ corresponds to the nearest neighbour pairs and $\langle\langle .. \rangle\rangle$ corresponds to the next nearest neighbour pairs. The spins S_i are considered to be three dimensional vectors in the spherical polar coordinates with $|S_i| = 1/2$.

Table 5.2: The ordering vector Q of the ground state for lattice A, in units of 2π , obtained from the peak of the equal time structure factor obtained from Iterative Minimisation (IM).

L	Q(2π)
6	$\frac{\pm 1}{2}, \frac{\pm 1}{6}, \frac{\pm 1}{3}$
8	$\frac{\pm 1}{2}, \frac{\pm 3}{8}, \frac{\pm 3}{8}$
10	$\frac{\pm 1}{2}, \frac{\pm 3}{10}, \frac{\pm 3}{10}$
12	$\frac{\pm 1}{2}, \frac{\pm 1}{12}, \frac{\pm 1}{3}$
14	$\frac{\pm 1}{2}, 0, \frac{\pm 5}{14}$
16	$\frac{\pm 1}{2}, \frac{\pm 3}{16}, \frac{\pm 5}{16}$
18	$\frac{\pm 1}{2}, \frac{\pm 1}{3}, \frac{\pm 1}{3}$
20	$\frac{\pm 1}{2}, \frac{\pm 1}{5}, \frac{\pm 7}{20}$

As a first step, we probed the ground state configuration of the model at zero temperature using the iterative minimization(IM) procedure. To identify the nature

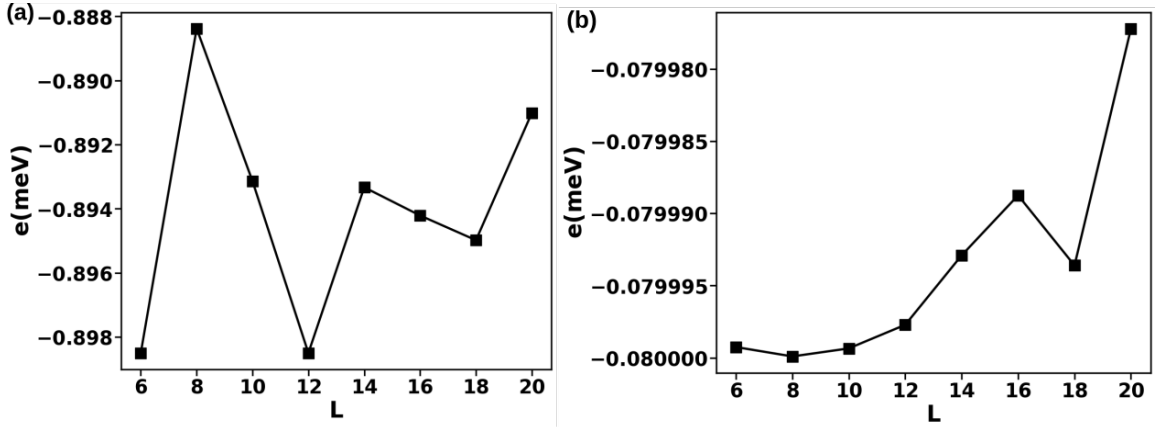


Figure 5.4: The energy per spin, e , for various linear system sizes L (a) for lattice A and (b) lattice B. The energy per spin remains almost the same for varying L .

of ground state using IM, we performed the calculations on various system sizes, L . The number of spins in the simulations is given by $N = 2 \times L \times L \times L$. The energy per spin for various system sizes L is plotted in Fig. 5.4. For each value of L , the equal time structure factor is calculated according to Eq. 5.4 and the ordering vector, which corresponds to the maxima in the structure factor are reported in Table 5.2. To understand the quantum system at finite temperatures, we resort to Monte Carlo simulations, as described in the computational methods section. The results at zero and finite temperatures for both the lattices are described in detail below,

Lattice A

It is clear from Fig. 5.4(a) that the energy per spin is equal upto third order at least for $L = 10$, $L = 14$ and $L = 16$ and the ordering vector, obtained from the peak of equal time structure factor varies with the system size L , suggesting that the exact magnetic ground state cannot be reached by finite size simulations. This corresponds to the case when the ordering vector approaches an irrational number^[52], hinting at an incommensurate ground state order in lattice A.

The finite temperature Monte Carlo simulations for this lattice show a magnetic tran-

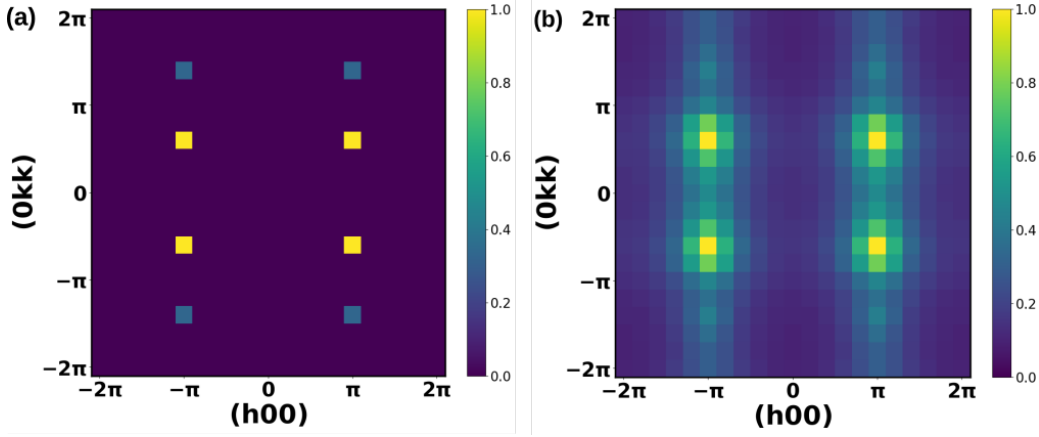


Figure 5.5: a) The equal time structure factor of lattice A from Iterative Minimisation for $L=10$. The peaks in this case occur at $(\frac{\pm 1}{2}, \frac{\pm 3}{10}, \frac{\pm 3}{10})$. b) The equal time structure factor at 5 K ($T > T_c$). The peaks are diffused about the peaks in (a).

sition temperature of 3 K, and the magnetic susceptibility vanishes as the T tends to zero. Experimentally, such a magnetic transition is not seen and the magnetic susceptibility also does not vanish down to the lowest measurable T , see the experimental results summarised in Fig. 5.3. Nevertheless, the rich physics associated with quantum spin liquids can be probed by understanding the effect of thermal (classical) fluctuations on these spins, in the temperature region above the ordering temperature. The spin structure factor, calculated using this model below T_c might not reproduce the experimentally observed signatures. However, at a temperature above T_c , the thermal fluctuations can mimic the role of quantum fluctuations observed at very low temperatures^[52]. The calculated equal time structure factor at 5 K, which is above T_c , as reported in figure 5.5(b) shows broad, diffused peaks, indicating a spin liquid phase at this temperature. In fact, these are the IM structure factor peaks (see figure 5.5(a)) broadened. Such a behavior is seen as because of the ferromagnetic and antiferromagnetic exchange interactions leading to a frustration in lattice A.

Lattice B

This lattice has the exchange interactions one order of magnitude lesser than lattice A. The first nearest neighbour interaction is ferromagnetic, with the second nearest

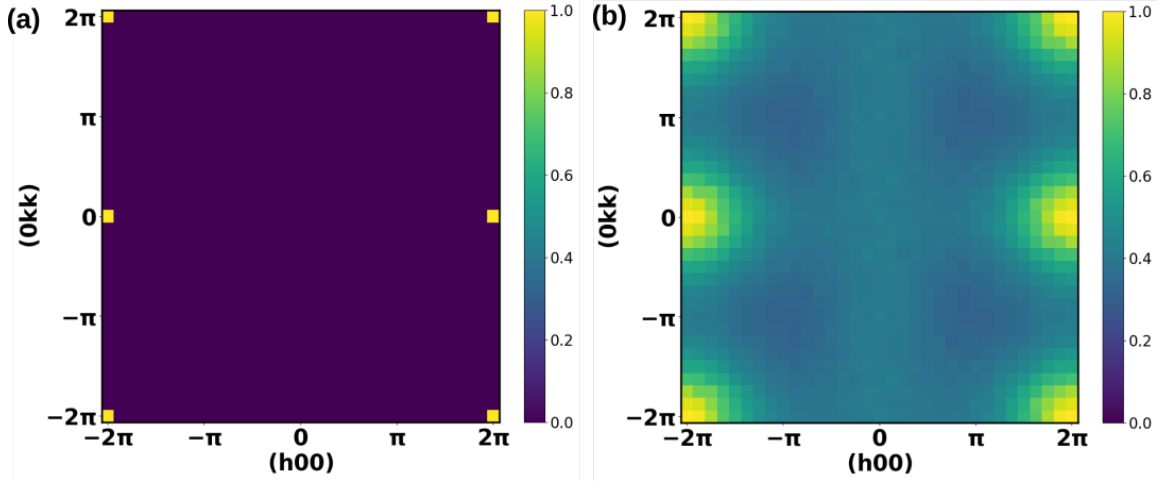


Figure 5.6: a) The equal time structure factor of lattice A from Iterative Minimisation for $L=12$
 b) The equal time structure factor at 1 K ($T > T_c$). The peaks are broad and diffused about the peaks in (a)

neighbour coupling antiferromagnetic with $J_2/J_1 = 1/2$. According to the iterative minimisation procedure, carried out for various linear system sizes L , the equal time structure factor peaks at $Q = 0$. The energy per spin with varying system size L is plotted in figure 5.6 (a). The nature of the lattice at finite temperature is understood with the help of Monte Carlo simulations employing heat bath algorithm coupled with over-relaxation. The very small exchange couplings lead to a much lower transition temperature ($T_c = 0.5K$) in this lattice. The equal time structure factor for this lattice at $T = 1K$ is reported in figure 5.6 (b). At this temperature above T_c , we see very broad diffused peaks about $Q=0$ ordering vector. This is indicative of “molten” state^[52,55–57], reminiscent of the spin liquid ground state observed in reality in the experiment.

Interestingly, the lattice A has the frustrated exchange interactions. Thus, the main point is that while the lattice A and lattice B both show spin liquid behavior above the transition temperature and below the Curie-Weiss temperature, the reasons are different. While for lattice A, the spin liquid behavior arises due to the lattice geometry, as the geometry allows frustrated exchange interactions, the spin-liquid behavior in lattice B is due to the exchange interactions, which are of opposite sign

and different in magnitude. It is highly possible that in the experimental system, both of these lattices are present in different proportions, as the spin liquid behavior is found between the respective transition temperature and Curie Weiss temperature, for both the low energy lattice structures.

5.4 Conclusion

We have carried out a comprehensive study of NaYbW_2O_8 having an inherent anti-site disorder (50%) using various physical properties characterization techniques and theoretical calculations. Yb^{3+} ions sit on a hyper honeycomb ($^{\mathcal{H}}\langle -1 \rangle$) lattice with sizeable antiferromagnetic interactions, and there is no magnetic phase transition down to 400 mK. Further, the dynamic nature of the local fields in the systems has been confirmed by zero-field μSR measurements. The theoretical studies revealed that this state originates from a combination of geometric frustration and competition between exchange interactions. The equal time structure factor in the two possible magnetic sublattices point to a spin liquid phase, owing through their broad peak. Hence, NaYbW_2O_8 stands out as a candidate that provides a platform to explore the disorder-driven correlated states in the quantum magnets.

Bibliography

- [1] L. Balents, Spin liquids in frustrated magnets, *Nature* **464**, 199 (2010).
- [2] L. Messio, B. Bernu, and C. Lhuillier, Kagome Antiferromagnet: A Chiral Topological Spin Liquid, *Phys. Rev. Lett.* **108**, 207204 (2012).
- [3] S. Capponi, V. R. Chandra, A. Auerbach, and M. Weinstein, p6 chiral resonating valence bonds in the kagome antiferromagnet, *Phys. Rev. B* **87**, 161118 (2013).
- [4] G. Misguich, D. Serban, and V. Pasquier, Quantum Dimer Model on the Kagome Lattice: Solvable Dimer-Liquid and Ising Gauge Theory, *Phys. Rev. Lett.* **89**, 137202 (2002).
- [5] S. Yan, D. A. Huse, and S. R. White, Spin-Liquid Ground State of the $S = 1/2$ Kagome Heisenberg Antiferromagnet, *Science* **332**, 1173 (2011).
- [6] S. Depenbrock, I. P. McCulloch, and U. Schollwöck, Nature of the Spin-Liquid Ground State of the $S = 1/2$ Heisenberg Model on the Kagome Lattice, *Phys. Rev. Lett.* **109**, 067201 (2012).
- [7] P. Mendels, F. Bert, M. A. de Vries, A. Olariu, A. Harrison, F. Duc, J. C. Trombe, J. S. Lord, A. Amato, and C. Baines, Quantum Magnetism in the

- Paratacamite Family: Towards an Ideal Kagomé Lattice, *Phys. Rev. Lett.* **98**, 077204 (2007).
- [8] T.-H. Han, J. S. Helton, S. Chu, D. G. Nocera, J. A. Rodriguez-Rivera, C. Broholm, and Y. S. Lee, Fractionalized excitations in the spin-liquid state of a kagome-lattice antiferromagnet, *Nature* **492**, 406 (2012).
- [9] L. Clark, J. C. Orain, F. Bert, M. A. De Vries, F. H. Aidoudi, R. E. Morris, P. Lightfoot, J. S. Lord, M. T. F. Telling, P. Bonville *et al.*, Gapless Spin Liquid Ground State in the $S=1/2$ Vanadium Oxyfluoride Kagome Antiferromagnet $[\text{NH}_4]_2[\text{C}_7\text{H}_{14}\text{N}][\text{V}_7\text{O}_6\text{F}_{18}]$, *Phys. Rev. Lett.* **110**, 207208 (2013).
- [10] Y. Okamoto, M. Nohara, H. Aruga-Katori, and H. Takagi, Spin-Liquid State in the $S = 1/2$ Hyperkagome Antiferromagnet $\text{Na}_4\text{Ir}_3\text{O}_8$, *Phys. Rev. Lett.* **99**, 137207 (2007).
- [11] A. Kitaev, Anyons in an exactly solved model and beyond, *Ann. Phys.* **321**, 2 (2006).
- [12] I. Kimchi, J. G. Analytis, and A. Vishwanath, Three-dimensional quantum spin liquids in models of harmonic-honeycomb iridates and phase diagram in an infinite- D approximation, *Phys. Rev. B* **90**, 205126 (2014).
- [13] S. Trebst and C. Hickey, Kitaev Materials, *Phys. Rep.* **950**, 1 (2022).
- [14] G. Xiao, Z. Xia, W. Zhang, X. Yue, S. Huang, X. Zhang, F. Yang, Y. Song, M. Wei, H. Deng *et al.*, *Cryst. Growth Des.* **19**, 2658 (2019).
- [15] W. Yao and Y. Li, *Phys. Rev. B* **101**, 085120 (2020).
- [16] R. Zhong, T. Gao, N. P. Ong, and R. J. Cava, *Sci. Adv.* **6**, eaay6953 (2020).
- [17] M. Songvilay, J. Robert, S. Petit, J. A. Rodriguez-Rivera, W. D. Ratcliff, F. Damay, V. Bal´edent, M. Jim´enez-Ruiz, P. Lejay, E. Pachoud, A. Hadj-Azzem, V. Simonet, and C. Stock, *Phys. Rev. B* **102**, 224429 (2020).

- [18] C. Kim, J. Jeong, G. Lin, P. Park, T. Masuda, S. Asai, S. Itoh, H.-S. Kim, H. Zhou, J. Ma *et al.*, J. Phys. Condens. Matter **34**, 045802 (2021).
- [19] X. Wang, R. Sharma, P. Becker, L. Bohatý, and T. Lorenz, Phys. Rev. Mater. **7**, 024402 (2023).
- [20] T. Halloran, F. Desrochers, E. Z. Zhang, T. Chen, L. E. Chern, Z. Xu, B. Winn, M. Graves-Brook, M. Stone, A. I. Kolesnikov *et al.*, Proc. Natl. Acad. Sci. U.S.A. **120**, e2215509119 (2023).
- [21] M. J. Daum, A. Ramanathan, A. I. Kolesnikov, S. Calder, M. Mourigal, and H. S. La Pierre, Phys. Rev. B **103**, L121109 (2021).
- [22] H. Ishikawa, R. Kurihara, T. Yajima, D. Nishio-Hamane, Y. Shimizu, T. Sakakibara, A. Matsuo, and K. Kindo, Phys. Rev. Mater. **6**, 064405 (2022).
- [23] A. Biffin, R. D. Johnson, I. Kimchi, R. Morris, A. Bombardi, J. G. Analytis, A. Vishwanath, and R. Coldea, Phys. Rev. Lett. **113**, 197201 (2014).
- [24] T. Takayama, A. Kato, R. Dinnebier, J. Nuss, H. Kono, L. S. I. Veiga, G. Fabbri, D. Haskel, and H. Takagi, Phys. Rev. Lett. **114**, 077202 (2015).
- [25] S.-H. Baek, H. W. Yeo, S.-H. Do, K.-Y. Choi, L. Janssen, M. Vojta, and B. Büchner, Observation of a random singlet state in a diluted Kitaev honeycomb material, Phys. Rev. B **102**, 094407 (2020).
- [26] L. Liu, H. Shao, Y.-C. Lin, W. Guo, and A. W. Sandvik, Random-Singlet Phase in Disordered Two-Dimensional Quantum Magnets, Phys. Rev. X **8**, 041040 (2018).
- [27] K. Kitagawa, T. Takayama, Y. Matsumoto, A. Kato, R. Takano, Y. Kishimoto, S. Bette, R. Dinnebier, G. Jackeli, and H. Takagi, A spin-orbital-entangled quantum liquid on a honeycomb lattice, Nature **554**, 341 (2018).

-
- [28] S.-H. Do, C. H. Lee, T. Kihara, Y. S. Choi, S. Yoon, K. Kim, H. Cheong, W.-T. Chen, F. Chou, H. Nojiri, and K.-Y. Choi, Randomly Hopping Majorana Fermions in the Diluted Kitaev System α -Ru_{0.8}Ir_{0.2}Cl₃, *Phys. Rev. Lett.* **124**, 047204 (2020).
- [29] I. Kimchi, J. P. Sheckelton, T. M. McQueen, and P. A. Lee, Scaling and data collapse from local moments in frustrated disordered quantum spin systems, *Nature Communications* **9**, 4367 (2018).
- [30] J. Khatua, M. Gomilšek, J. C. Orain, A. M. Strydom, Z. Jagličić, C. V. Colin, S. Petit, A. Ozarowski, L. Mangin-Thro, K. Sethupathi, M. S. R. Rao, A. Zorko, and P. Khuntia, Signature of a randomness-driven spin-liquid state in a frustrated magnet, *Communications Physics* **5**, 99 (2022).
- [31] G. Kresse and J. Furthmüller, Efficient Iterative Schemes for Ab Initio Total-Energy Calculations Using a Plane-Wave Basis Set, *Phys. Rev. B* **54**, 11169 (1996).
- [32] G. Kresse and J. Furthmüller, Efficiency of Ab-Initio Total Energy Calculations for Metals and Semiconductors Using a Plane-Wave Basis Set, *Comput. Mater. Sci.* **6**, 15 (1996).
- [33] G. Kresse and J. Hafner, Ab Initio Molecular Dynamics for Liquid Metals, *Phys. Rev. B* **47**, 558 (1993).
- [34] G. Kresse and D. Joubert, From Ultrasoft Pseudopotentials to the Projector Augmented-Wave Method, *Phys. Rev. B* **59**, 1758 (1999).
- [35] J. P. Perdew, K. Burke, and M. Ernzerhof, Generalized Gradient Approximation Made Simple, *Phys. Rev. Lett.* **77**, 3865 (1996).
- [36] Y. Chornodolskyy, V. Karnaushenko, J. Selech, V. Vistovsky, T. Demkiv, K.

- Przystupa, S. Syrotyuk and A. Voloshinovskii, Computer Modelling of Energy Structure of Yb^{3+} and Lu^{3+} Doped LaF_3 Crystals, *Materials*, **15**, 7937 (2022).
- [37] Y. Lu, J. Wang, J. Li, J. Wu, S. Kanno, T. Tada and H. Hosono, Realization of Mott-insulating electrides in dimorphic Yb_5Sb_3 , *Phys. Rev. B*, **98**, 125128 (2018).
- [38] Y. Miyatake, M. Yamamoto, J. J. Kim, M. Toyonaga and O. Nagai, On the implementation of the 'heat bath' algorithms for Monte Carlo simulations of classical Heisenberg spin systems, *J. Phys. C: Solid State Physics*, **19**, 2539 (1986).
- [39] Michael Creutz, Overrelaxation and Monte Carlo simulation, *Phys. Rev. D*, **36**, 515 (1987).
- [40] S. S. Perera and F. A. Rabuffetti, *Cryst. Eng. Comm.* **18**, 5818 (2016).
- [41] K. A. Modic, T. E. Smidt, I. Kimchi, N. P. Breznay, A. Biffin, S. Choi, R. D. Johnson, R. Coldea, P. Watkins-Curry, G. T. McCandless, J. Y. Chan, F. Gandara, Z. Islam, A. Vishwanath, A. Shekhter, R. D. McDonald, and J. G. Analytis, Realization of a three-dimensional spin-anisotropic harmonic honeycomb iridate, *Nat. Commun.* **5**, 4203 (2014).
- [42] N. D. Kelly, L. Yuan, R. L. Pearson, E. Suard, I. P. Orench, and S. E. Dutton, *Phys. Rev. Materials* **6**, 044410 (2022).
- [43] M. M. Bordelon, J. D. Bocarsly, L. Posthuma, A. Banerjee, Q. Zhang, and S. D. Wilson, *Phys. Rev. B* **103**, 024430 (2021).
- [44] M. M. Bordelon, C. Liu, L. Posthuma, E. Kenney, M. J. Graf, N. P. Butch, A. Banerjee, S. Calder, L. Balents, and S. D. Wilson, *Phys. Rev. B* **103**, 014420 (2021).

-
- [45] C. A. Marjerrison, C. Mauws, A. Z. Sharma, C. R. Wiebe, S. Derakhshan, C. Boyer, B. D. Gaulin, and J. E. Greedan, *Inorg. Chem.* **55**, 12897 (2016).
- [46] S. Injac, A. K. L. Yuen, B. J. Kennedy, M. Avdeev, and F. Orlandi, *Phys. Chem. Chem. Phys.* **21**, 7261 (2019).
- [47] Y. Li, D. Adroja, R. I. Bewley, D. Voneshen, A. A. Tsirlin, P. Gegenwart, and Q. Zhang, Crystalline electric-field randomness in the triangular lattice spin-liquid YbMgGaO_4 , *Phys. Rev. Lett.* **118**, 107202 (2017).
- [48] L. Ding, P. Manuel, S. Bachus, F. Grüßler, P. Gegenwart, J. Singleton, R. D. Johnson, H. C. Walker, D. T. Adroja, A. D. Hillier *et al.*, Gapless spin-liquid state in the structurally disorder-free triangular antiferromagnet NaYbO_2 , *Phys. Rev. B* **100**, 144432 (2019).
- [49] J. G. Rau, L. S. Wu, A. F. May, L. Poudel, B. Winn, V. O. Garlea, V. O. Garlea, A. Huq, P. Whitfield, A. E. Taylor, M. D. Lumsden *et al.*, Anisotropic exchange within decoupled tetrahedra in the quantum breathing pyrochlore $\text{Ba}_3\text{Yb}_2\text{Zn}_5\text{O}_{11}$, *Phys. Rev. Lett.* **116**, 257204 (2016).
- [50] T. Besara, M. S. Lundberg, J. Sun, D. Ramirez, L. Dong, J. B. Whalen, R. Vasquez, F. Herrera, J. R. Allen, M. W. Davidson *et al.*, Single crystal synthesis and magnetism of the BaLn_2O_4 family (Ln = lanthanide), *Prog. Solid State Chem.* **42**, 23 (2014).
- [51] M. Mitric, B. Antic, M. Balanda, D. Rodic, and M. L. Napijalo, An x-ray diffraction and magnetic susceptibility study of $\text{Yb}_x\text{Y}_{2-x}\text{O}_3$, *J. Phys.: Condens. Matter* **9**, 4103 (1997).
- [52] Anna Fancelli, Johannes Reuther and Bella Lake, Classical spin models of the windmill lattice and their relevance for $\text{PbCuTe}_2\text{O}_6$, *Phys.Rev.B* **108**, 184415 (2023).

- [53] Michael Creutz, Overrelaxation and Monte Carlo simulation, *Phys. Rev. D*, **36**, 515 (1987).
- [54] Sophia R. Sklan and Christopher L. Henley, Nonplanar ground states of frustrated antiferromagnets on an octahedral lattice, *Phys. Rev. B* **88**, 024407 (2013).
- [55] Masashi Hosoi, Emily Z. Zhang, Adarsh S. Patri and Yong Baek Kim, Uncovering Footprints of Dipolar-Octupolar Quantum Spin Ice from Neutron Scattering Signatures, *Phys. Rev. Lett*, **129**, 097202 (2022).
- [56] A. M. Samarakoon, A. Banerjee, S. S. Zhang, Y. Kamiya, S. E. Nagler, D. A. Tennant, S. H. Lee and C. D. Batista, Comprehensive study of the dynamics of a classical Kitaev spin liquid, *Phys. REv. B*. **96**, 134408 (2017).
- [57] Oliver Franke, Dumitru Călugăru, Andreas Nunnenkamp, and Johannes Knolle, Thermal spin dynamics of Kitaev magnets: Scattering continua and magnetic field induced phases within a stochastic semiclassical approach, *Phys. Rev. B*. **106**, 174428 (2022)

Conclusion and Future Outlook

In summary, this thesis explores two different kinds of exotic phases of matter - topological insulators and quantum spin liquids. The former, is a symmetry protected topologically trivial state of matter, meaning they are not protected against “any” local perturbation, but only some perturbations which do not break the $U(1)$ and time reversal symmetry, On the other hand, the latter is a topologically non-trivial phase, with large ground state degeneracy and long-range entanglement. This thesis identifies non-trivial topological insulator phases in a few chalcogenide systems and predicts two possible quantum spin liquid candidates in Rare-Earth based oxide systems.

The first topological insulator system studied was TaSe_3 , the choice of which was motivated by the possible realisation of topological superconducting phase in this material, which could potentially host Majorana fermions. Through our studies, we found a weak topological insulating phase in TaSe_3 at ambient conditions, with the weak invariants (101), suggesting a topologically dark (101) surface in TaSe_3 . However, with the application of hydrostatic pressure, we are able to tune the topological property of the system. We find a range of pressure between 4.5 GPa and 7 GPa, where TaSe_3 becomes a strong topological insulator with an odd number of Dirac cones on it’s surfaces. A further increase in pressure pushes it into another weak topological insulator phase, marked by a (100) stacking direction. This interesting

features of topological phases of TaSe_3 with application of hydrostatic pressure can be put to use in spintronics and quantum computing applications.

The next topological candidates we considered were of interest from a thermoelectric point of view. Topological insulators and thermoelectricity are intricately intertwined. It has been observed that many materials which are good thermoelectrics are topological insulators and topological insulators are always good thermoelectrics. The $(\text{Sb}_2\text{Te}_3)_m(\text{Sb}_2)_n$ homologous series is well known for its good thermoelectric properties. Three materials from this series - Sb_2Te_3 , Sb_2Te and SbTe - are studied with respect to their topological nature. We find that all of them are topological insulators. Additionally, we observe multiple hole pockets in the band structure of SbTe and Sb_2Te as compared to Sb_2Te_3 , suggesting that SbTe and Sb_2Te could be much useful in the field of thermoelectrics. We further explored how Sb_2Te_3 and Sb_2Te respond to lattice distortions by studying the effect of uniaxial strain along the c -direction and hydrostatic pressure on these two systems. Though we do not see any topological phase transition with strain, we observe a change in the topology in both the systems, with the application of pressure. Sb_2Te_3 undergoes a transition to a normal insulator at high pressure, while Sb_2Te becomes a weak topological insulator at high pressures. A future direction is to study the effect of the surface states to the thermoelectric properties of this series and to really gauge the contribution of the surface states to the transport properties in this extremely unique set of systems. Moreover, the layered nature this series make them exceptional in realising low dimensional and twisted hetero structure systems. Recent studies look at how the electronic band structure can be modulated with Moire patterns and it could be an interesting area to pursue.

In this thesis, we propose two novel materials which could potentially host quantum spin liquid phases. Quantum spin liquids are extremely interesting phases of matter, which can host fractionalized excitations which follow non-abelian statistics. These exotic properties are a result of their long-range entangled ground state. The

applications of such QSL phases are enormous. They can be the future of quantum computing and quantum information processing, because of their ability for fault-tolerant computing. We observe signatures of QSL phase in a dimer based Lanthanide oxide, $\text{Yb}_2\text{Te}_5\text{O}_{13}$ and a disordered system, NaYbW_2O_8 . Our studies reveal broad diffused equal time structure factor in both these systems, confirming their spin liquid behaviour. Though we have tried to understand the magnetic nature through classical simulations, the thermal fluctuations on the classical spins are shown to mimic the quantum fluctuations that the quantum spins experience at 0 K. We looked at the behaviour of both the systems between the transition temperature and the Curie-Weiss temperature and we obtain a “molten” remnant of a QSL space in this region in both the systems. More experiments and theoretical studies of these systems are required to fine tune their properties and to integrate them into emerging technology. Another interesting direction to pursue would be to understand and discover phase transitions that can occur in such QSL systems, thereby mapping out a phase diagram of this exotic phases of matter.

It is true that the systems studied in the thesis are open shell d- and f- orbital systems, where the strong correlation of electrons can potentially lead to spurious results. This is common with the application of DFT to such strongly correlated systems. The main reason for this is the inadequacy of the approximate exchange-correlation functionals that are commonly in use today. These functionals, like LDA, GGA etc, leads to delocalization or self-interaction error and static correlation error. There exists many methods to correct these errors to some extent. We have used one such method- the addition of a Hubbard correction to the GGA-DFT, thereby improving the delocalization error. A more accurate way is to use hybrid functionals like HSE for extended systems, where a fraction of the exact Hartree-Fock exchange is added to the functional. Though this can predict band gaps closer to experiments, the parameters of mixing required to accurately describe a particular system has to be semi-empirically determined, making it's applications limited and certainly not

helpful in predicting new materials. Another way is to use many body perturbation theory based on Green's function formalism, to calculate the the response of a system to the addition or removal of electrons. In this theory, the central quantity is the exchange-correlation self energy, which accounts for all electron-electron interaction beyond the Hartree-Fock approach. The GW approximation, where is self-energy is approximated using single particle Green's function, G and screened Coulomb interaction W , is the best first-principles method to describe the band structures of normal semiconductors and insulators. However, since this is based on a quasi-particle picture and strong correlation effects include interactions beyond this picture, GW calculation cannot capture the entire effect of the strong correlations in open d- or f-orbital systems. However, it can be used to get an accurate band structure of the system, based on which correlation effects beyond band structure can be studied. The best method so far to treat highly correlated systems is to use GW + DMFT (Dynamical Mean Field Theory), where the parameters for DMFT are obtained from the highly accurate GW calculations. Developing and comparing various methods to circumvent DFT errors is extremely crucial and requires much more attention.

The future holds immense potential for the development and implementation of technologies which are truly mind-bending. The search and realisation of exotic phases of matter, would be a great gift to the humanity as a whole. Our work tries to shed light on some fundamental properties required for such futuristic applications and reveals some interesting phenomena. In the process of doing so, we realize that the materials world holds vast potential with single-phase and multi-phase materials, as well as pure, hybrid, heterostructure and superlattice structures of materials that incorporate a greater variety of transition and post-transition metals with 3d, 4d, 5d and 4f bands. The search for materials with multiple exotic phenomena should be at the forefront of future research and this will indeed help us solve and understand the more ubiquitous problems in material science. In addition to identifying and classifying exotic phases in condensed matter physics, importance should be given to

mapping out a more comprehensive phase diagram of such phases, such that their potential applications can be easily predicted. The effect of temperature, magnetic field and electric field on the nature of these phases are of extreme importance from an application point of view. In addition, the functional applications of these phases and the possibilities of device manufacturing should be analysed to gain an in-depth understanding of the real possibilities such exotic systems can offer.

Other Works

During my PhD I have looked at some other phenomena as well, as given below

- In Situ Cation Intercalation in the Interlayer of Tungsten Sulfide with Overlaying Layered Double Hydroxide in a 2D Heterostructure for Facile Electrochemical Redox Activity

Sahanaz Parvin, Vishwadeepa Hazra, Anita Gemmy Francis, Swapan K. Pati, Sayan Bhattacharyya, *Inorg. Chem.*, 60 (2021).

In this work, we show how the catalytic property of a NiCO-Layered double Hydroxide and 1T'-WS₂ heterostructure is modulated by Ni²⁺ and Co²⁺ ions which intercalate between the two layers in the heterostructure. The finite Density of States (DOS) of the Ni and Co d-orbitals near the Fermi-level gives evidence to this phenomena.

- Impacts of Exciton Binding Energy and Dielectric Confinement of Layered Lead Halide Perovskites on Carrier Relaxation and Exciton Phonon Interactions
Kritiman Marjit, Anita Gemmy Francis, Swapan K Pati, and Amitava Patra, *J. Phys. Chem. Lett.*, 14 (2023). In this work we study the carrier-relaxation dynamics of Layered Perovskites (LP)s and the dependence of this dynamics on the chain length of the spacer ion. We have considered

three LPs, $(\text{BA})_2\text{PbI}_4$, $(\text{HA})_2\text{PbI}_4$ and $(\text{OA})_2\text{PbI}_4$, with the length of the spacers increasing from Butylamine (BA) to Hexylamine (HA) to Octylamine (OA). We observe that the dielectric confinement is the lowest in $(\text{BA})_2\text{PbI}_4$ and the largest in $(\text{OA})_2\text{PbI}_4$, with $(\text{HA})_2\text{PbI}_4$ having a value in between. The exciton binding energy was calculated using the Wannier-Mott model, which shows that the binding energy decreases in the order $(\text{OA})_2\text{PbI}_4 > (\text{HA})_2\text{PbI}_4 > (\text{BA})_2\text{PbI}_4$. Both these facts combine to make the carrier relaxation in $(\text{OA})_2\text{PbI}_4$ much faster than the other two, with $(\text{BA})_2\text{PbI}_4$ having the slowest electron-hole recombination dynamics. An analysis of the phonon dispersion of the three systems suggest that the smaller up-conversion of acoustic modes to optical modes in $(\text{OA})_2\text{PbI}_4$, is in fact responsible for this observed ultrafast dynamics in $(\text{OA})_2\text{PbI}_4$.